Towards Reliable Prediction of Wave-in-Deck Loads and Response of Offshore Structures

by

Nagi Abdussamie, MSc (Mechanical Engineering)

National Centre for Maritime Engineering and Hydrodynamics
Australian Maritime College

Submitted in fulfilment of the requirements for the degree of Doctor of Philosophy
University of Tasmania

June 2016

Declarations

Authority of Access

The publishers of the papers comprising Chapters 2 – 5 hold the copyright for that content, and access to the material should be sought from the respective journals. The remaining non-published content of this thesis may be made available for loan and limited copying and communication in accordance with the Copyright Act 1968.

Declaration of Originality

This thesis contains no material which has been accepted for a degree or diploma by the University or any other institution, except by way of background information and duly acknowledged in the thesis, and to the best of my knowledge and belief no material previously published or written by another person except where due acknowledgement is made in the text of the thesis, nor does the thesis contain any material that infringes copyright.

Signed: Date: 17 June 2016

Nagi Abdussamie

Statement of Co-Authorship

Paper 1 (Chapter 2): ***Measurements of global and local effects of wave impact on a fixed platform deck, Journal of Engineering for the Maritime Environment.***

Roberto Ojeda, Giles Thomas, Yuriy Drobyshevski and Walid Amin contributed to experiment design and data interpretation.

Percentage of Contribution: Candidate 70%, R. Ojeda 8%, G. Thomas 8%, Y. Drobyshevski 7%, W. Amin 7%.

Paper 2 (Chapter 3): ***Experimental investigation of extreme wave impacts on a rigid TLP model in cyclonic conditions, Journal of Ships and Offshore Structures.***

Roberto Ojeda, Yuriy Drobyshevski, Giles Thomas and Walid Amin contributed to experiment design and data interpretation.

Percentage of Contribution: Candidate 70%, R. Ojeda 12%, Y. Drobyshevski 10%, G. Thomas 6%, W. Amin 2%.

Paper 3 (Chapter 4): ***Dynamic behaviour of a tension leg platform due to wave-in-deck impact events, Journal of Ocean Engineering.***

Roberto Ojeda, Giles Thomas, Yuriy Drobyshevski and Walid Amin contributed to experiment design and data interpretation.

Percentage of Contribution: Candidate 70%, R. Ojeda 12%, G. Thomas 8%, Y. Drobyshevski 8%, W. Amin 2%.

Paper 4 (Chapter 5): ***Wave-in-deck loads and response of a TLP model in unidirectional regular waves, Journal of Ships and Offshore Structures.***

Yuriy Drobyshevski, Roberto Ojeda, Giles Thomas and Walid Amin contributed to experiment design and data interpretation.

Percentage of Contribution: Candidate 70%, Y. Drobyshevski 12%, R. Ojeda 10%, G. Thomas 7%, W. Amin 1%.

We the undersigned agree with the above stated “proportion of work undertaken” for each of the above published (or submitted) peer-reviewed manuscripts contributing to this thesis

Signed:

Dr Roberto Ojeda
Primary Supervisor
National Centre for Maritime Engineering and Hydrodynamics
University of Tasmania
Date: 03/10/2016

Prof Giles Thomas
Co-Supervisor
Department of Mechanical Engineering
University College London
Date: 04/10/2016

Dr Yuriy Drobyshevski
Co-Supervisor
National Centre for Maritime Engineering and Hydrodynamics
University of Tasmania
Date: 03/10/2016

Dr Walid Amin
Co-Supervisor
National Centre for Maritime Engineering and Hydrodynamics
University of Tasmania
Date: 03/10/2016

Acknowledgements

Peace be upon you all. Thank Allah for giving me the time and the strength and enabling me to complete this work. I would like to express my thankful to my primary supervisor Dr Roberto Ojeda for his guidance, assistance and advice throughout my study. Without his encouragement, nothing would be achieved.

I would like to express my sincere thanks to Dr Yuriy Drobyshevski from INTECSEA for his advice and great guidance. I have learned many hydrodynamic aspects from him. His great suggestions put me on the right track and without such, I would be lost.

I also thank Professor Giles Thomas for his kind support and encouragement. I also thank Dr Walid Amin for his assistance at the beginning of my research.

My special thanks must also go to all AMC staff, in particular, Mr Luciano Mason who taught me many things about wave mechanics and the great discussions and interpretations on my results.

I must acknowledge the assistance from Mr Tim Lilienthal, Mr Kirk Meyer and Mr Liam Honeychurch at the AMC towing tank. I thank also all my colleagues who have advised and assisted me, in particular, Dr Jalal Shahraki.

I would like also to thank Associate Professor Jean-David Caprace and Professor Patrick Kaeding for their constructive comments which definitely improved the quality of this work.

Last but not least, to my wife and kids, to my family in Libya, to my mother's soul who passed away in 2013, thank you all for the support and feeling.

Abstract

Offshore structures need to survive whilst being exposed to extreme wave events, which can potentially threaten workers, environment and the structure itself. Despite the increase in regulating air gap requirements, numerous offshore installations around the world continue to suffer damage due to wave-in-deck loads, and yet the prediction methods for these loads are still not mature.

This thesis reports on the development of reliable experimental and numerical techniques for the analysis and prediction of wave-in-deck loads and the resulting response of different types of offshore structures. The investigated structures included a fixed platform deck, a fixed multicolumn platform (rigidly mounted Tension Leg Platform) and a compliant TLP.

Experimental investigations were conducted at the Australian Maritime College (AMC) towing tank at a model scale of 1:125 to examine extreme wave events associated with a 10,000-year tropical cyclonic condition offshore Western Australia. All the investigated models were subjected to long-crested irregular waves. The compliant TLP model was also subjected to several deterministic unidirectional regular waves aimed at validating two-phase flow numerical models.

The scope of the experimental part was to obtain the magnitudes and trends in the wave forces, discrete local pressures and the platform dynamics and to obtain high-quality data for the purpose of validation of numerical predictions. The effect of the deck clearance reduction on the magnitudes of forces and pressure acting on the fixed structures was also examined. Model accelerations were monitored for each wave impact event so that the inertial force effects due to the structural dynamic response could be identified.

Uncertainty analyses conducted in this work demonstrated that variability in the measurements of wave elevations, global loads and motion responses were minimised using highly-controlled model tests of 4 – 5 repeated runs for each test condition.

The experimental results for a fixed platform deck showed that a reduction of deck clearance (up to 2.5 m in full scale, ≈17% of the original deck clearance) significantly increased global loads due to wave impacts (by a factor of 2). However, reducing deck clearance did not result in increased impact pressure magnitudes for all locations. In contrast, for a fixed multicolumn platform, a reduction in deck clearance was found to have no clear effect on either global or local vertical wave-in-deck loads.

For a compliant floating TLP, wave-in-deck impact events were found to have a significant effect on the tendon tensions. The experiments showed that the maximum tension in the up-wave tendons usually occurred when the wave crest reached the deck leading edge. The down-wave tendons experienced lower tensions and frequently became slack when the wave crest excited the platform deck, and ringing responses were produced in both the up-wave and the down-wave tendons. The slam pressure was found to correlate with wave steepness; the steeper waves tended to cause higher pressures.

The numerical part of the investigation used the commercial Computational Fluid Dynamics (CFD) code STAR-CCM+ to simulate the characteristics of a unidirectional regular wave impact on the floating TLP model. The numerical results of surge motions, tendon tensions and deck slamming pressures were compared against the measurements acquired in model tests. The CFD simulations showed that the model's motions and tendon tensions predicted by CFD were in good agreement with the measurements, except for the initial transient periods caused by the start-up condition of the wavemaker. Using CFD results, it was revealed that the downward component of the vertical wave-in-deck force caused tendon slack situations in the down-wave tendons.

The consequences of wave-in-deck impact events were identified and a better understanding of the problem for different types of offshore structures was gained. CFD simulations in regular waves developed a starting point towards reliable prediction of such loads. The results of the present investigations provide statistically reliable force (global) and pressure (local) values which can be used for the validation of advanced CFD models of wave-in-deck impact problems in irregular waves. Hence, the wave-in-deck loads associated with extreme wave conditions can be assessed to evaluate the risk for local damage to structural members as well as platform structural integrity. Overall, the knowledge gained in this project contributes towards broadening the understanding of the wave-in-deck impact of offshore structures.

Table of Contents

List of Figures

List of Tables

Nomenclature

(-)	Negative or downward direction	[-]
(+)	Positive or upward direction	[-]
a	Dynamic air gap	[m]
a_0	Deck clearance or still-water air gap	[m]
a_n	Dynamic air gap due to platform set-down	[m]
a_x	Model's acceleration in x-direction	[m/s^2]
a_z	Model's acceleration in z-direction	[m/s^2]
B	Breadth of the topside deck	[m]
C	Phase celerity	[m/s]
C_{air}	Sound speed in air	[m/s]
C_g	Centre of gravity	[m]
CV	Coefficient of variation	[-]
D	Column diameter	[m]
dt	Time interval/step	[s]
F	Force	[N]
F^*	Normalised force	[-]
F_B	Buoyancy force	[N]
f_c	Cut-off frequency	[Hz]
f_n	Natural frequency	[Hz]
h	Height of pontoon	[m]
H	Measured wave height	[m]
h_d	Height of the topside deck	[m]
H_s	Significant wave height	[m]
I	Mass moment of inertia	[kg.m^2]
k	Wave number	[1/m]
L	Length of the topside deck	[m]
L_o	Total tendon length at zero offset	[m]
m	Mass	[kg]
N	Number of occurrences in ringing response	[-]
n	Number of tendons per leg	[-]
p	Pressure	[Pa]
P^*	Normalised impact pressure	[-]
P_i	Impact/slam pressure	[Pa]
Q1	First quartile (25th percentile)	[-]
Q3	Third quartile (75th percentile)	[-]
R	Wave realisation	[-]
s	Column spacing	[m]

S	Wave steepness	[-]
t	Time	[s]
T	Wave period	[s]
T^*	Normalised tendon tension by T_o	[-]
T'	Instantaneous tendon tension	[N]
t_f	End time	[s]
t_i	Time instance at the wave impact	[s]
T_{max}	Maximum tendon tension	[N]
T_{min}	Minimum tendon tension	[N]
T_o	Initial pretention at SWL	[N]
t_o	Initial time	[s]
T_p	Peak wave period	[s]
T_r	Tendon tension range due to ringing	[N]
t_{slack}	Time elapsed during tendon slackness	[s]
T_z	Zero up-crossing wave period	[s]
u	Horizontal particle velocity	[m/s]
$U(t)$	Horizontal velocity of the model	[m/s]
u_r	Relative horizontal velocity	[m/s]
W	Width of pontoon	[m]
x	Coordinate system in *x-axis* (longitudinal direction)	[-]
X	Surge motion amplitude	[m]
$x(t)$	Instantaneous horizontal position of the model	[m]
y	Coordinate system in *y-axis* (transverse direction)	[-]
z	Coordinate system in *z-axis* (vertical direction)	[-]
Z	Platform set-down	[m]
ΔT	Change in tendon tension	[N]
ϵ	Deck exceedance	[-]
η_c	Measured crest height	[m]
λ	Wave length	[m]
ρ	Mass density	[kg/m^3]
σ	Standard deviation	[varied]

Abbreviations

ABS	American Bureau of Shipping
AFT	The aft section of the deck underside
AMC	Australian Maritime College
API	American Petroleum Institute
BV	Bureau Veritas
CFD	Computational Fluid Dynamics
CTLP	Conventional TLP
CV	Coefficient of Variation
DFBI	Dynamic Fluid Body Interaction
DNV	Det Norske Veritas
DOF	Degree Of Freedom
Eq.	Equation
Exp.	Experimental results
FFT	Fast Fourier Transform
FWD	The forward section of the deck underside
GoM	Gulf of Mexico
HRIC	High Resolution Interface Capturing
iVOF	Improved VOF
JONSWAP	Joint North Sea Wave Project
LE	Leading Edge of the topside deck
MLDT	Magnetostrictive Linear Displacement Transducer
NWS	North West Shelf
PM	Pierson-Moskowitz
PT	Pressure Transducer
RHS	Rectangular Hollow Section
SIMPLE	Semi-Implicit Method for Pressure-Linked Equations
TE	Trailing Edge of the topside deck
TLP	Tension Leg Platform
VOF	Volume Of Fluid
WE	Wave Event
WP	Wave Probe

Chapter 1: Introduction

1.1. Background

Offshore installations in many global locations including Gulf of Mexico (GoM), Australian North West Shelf (NWS) and the North Sea are exposed to harsh metocean conditions which generate severe wave events. During the period 2004 – 2005, offshore installations located in the GoM were exposed to destructive forces of hurricanes *Ivan*, *Katrina* and *Rita* [1]. A total of 118 offshore platforms were completely destroyed, and 72 other platforms were severely damaged by these hurricances. An appreciation of the extent of damage generated by these extreme weather events can be gained from Figure 1-1 where a stacked diagram of destroyed/severely damaged offshore platforms and rigs by these hurricanes during 2004 – 2005 is shown. In many cases, insufficient air gap (*the vertical distance between the design wave crest and the lower deck underside of an offshore platform*) has been reported to be one of the major reasons for damage sustained by offshore structures. Buchan *et al.* [2] reported on the impact of tropical cyclone *Olivia* on Australia's NWS which caused significant and extensive damage to oil and gas facilities in the region. Metocean measurements taken during the storm indicate that the maximum wave heights were in the order of 15 to 20 m.

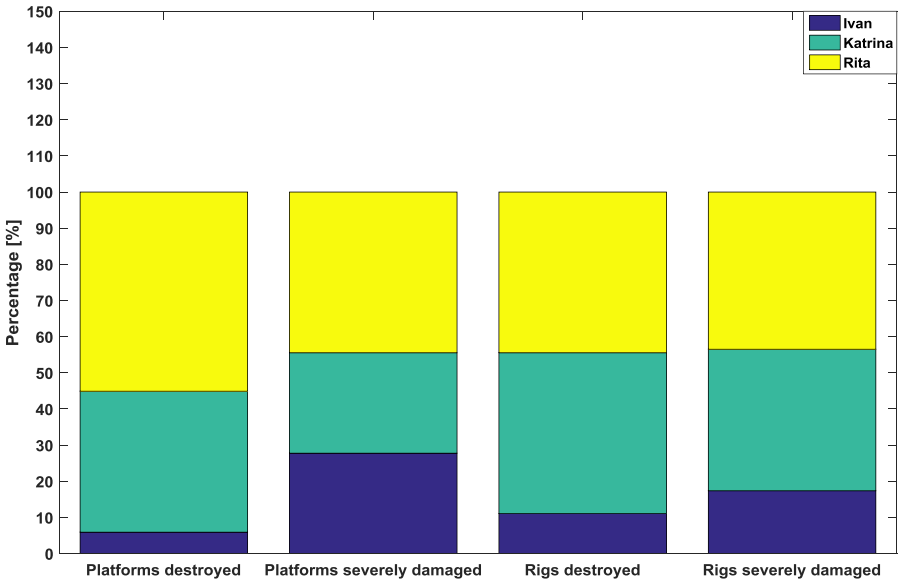

Figure 1-1: A stacked diagram showing the destroyed or severely damaged offshore platforms and rigs by Hurricanes during 2004 – 2005 in the Gulf of Mexico.

Such large (and steep) waves are greater in magnitude than the waves that these structures were designed for and would exceed the still-water air gap of many existing

offshore platforms in the region of NWS and other regions in the world [3, 4]. Most recently, in December 2015, living quarters of 50 workers of an offshore drilling rig in the North Sea were damaged when an enormous wave hit the accommodation block leaving one person dead and two more injured [5]. It has been found that these events occur more frequently than have been predicted using theoretical techniques [6]. In this thesis, such events are termed as *wave-in-deck* impacts where the wave crest is high enough to reach the deck underside of a platform's topside deck structure as defined in the recommended practice DNV-RP-C205 [7]. Wave overtopping and green water effects "*wave-on-deck*" are beyond the scope of this project.

Current regulations used in the design of an offshore platform for a specific site require a minimum air gap of 1.5 m between the expected magnitude of a 100-year wave crest (including tide and storm surge) and the underside of the lowest deck of the platform [8-10]. According to the current design practices for floating structures [11, 12], the survival conditions (1,000-year return period) are commonly used by designers for evaluating minimum required deck clearance (zero air gap). The recommended crest values for the North Sea and the Norwegian Sea have recently been increased. New platforms will be designed with an air gap sufficient to avoid impacts with a 10^{-4} annual probability crest, or equivalent to 10,000-year return period [13].

When attempting to ensure the survivability of offshore structures to large wave impacts, attention frequently focuses on extreme wave events, i.e., freak or rogue waves. These waves appear surprisingly as walls of water. Rogue waves are rare and strongly nonlinear waves that occur during extreme weather events that can cause serious damage to ships and offshore structures [14], examples of such are shown in Figure 1-2.

Figure 1-2: A photograph showing an extreme wave hitting the deck underside [online photo].

An accurate evaluation of the hydrodynamic loading and the corresponding dynamic characteristics experienced by offshore installations is therefore required to ensure that it will be able to survive these severe environmental conditions [11, 12]. This is crucial not only to ensure the survivability of the installation but also the safety of its crew.

1.2. State-of-the-art and Problem Definition

As highlighted above, provision of an adequate freeboard (air gap) of an offshore platform and prediction of the wave induced loads in the event of this freeboard being exceeded are important design tasks, for both fixed and floating offshore installations. One of the new developments at the Australian NWS is tension leg platforms (TLPs) which will be permanently moored in the field [15].

A TLP is a floating system connected to the sea floor by a series of pre-tensioned tethers. In other words, the TLP is classified as a compliant structure, moored to the seabed by vertical tethers/tendons that are tensioned by excess buoyancy over the weight of the structure. Figure 1-3 shows the structural components of a TLP, namely the hull, column top frame, topside deck, tendon system and foundation system [16]. Over the past decades, several TLP concepts have been explored, developed and used in the GoM and elsewhere in the world. The conventional type of TLPs (referred to as CTLP) consists of four columns connected by a ring pontoon at the base and a rectangular deck at the top.

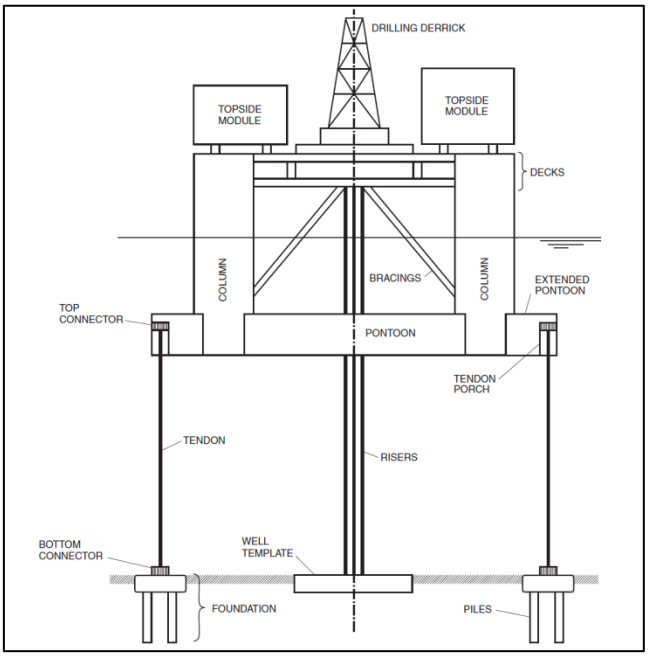

Figure 1-3: Profile view of a typical TLP [16] [not to scale].

Although historically TLPs have been used for hydrocarbon extraction below the seabed, they are now being used for the installation of lightweight floating offshore wind turbines [17]. An important operational requirement of TLPs is to have restricted heave motion to support vertical rigid risers (for oil and gas production) and wind turbines (for renewable energy). An undesirable consequence of this requirement is limited compliancy of the platform, which contributes to wave run-up on the structure. In effect, during high sea states water could run up along their columns hitting the topside structure [18].

Most critically, if an appropriate air gap for the TLP is not provided at its design stage, or is not maintained during its operation, direct wave impacts onto the deck of a TLP structure may occur resulting in severe wave-in-deck and slamming loads. These slam events can generate major global and local loads causing structural damage to the deck and floater structures, generating large forces in the mooring lines and risers and/or adversely affecting the floating structure's motions [19]. An accurate analysis of the effects of wave-in-deck impact on floating platforms such TLPs and Semi-submersibles is, therefore, a necessity [20]. However, such an analysis is an extremely complex endeavour due to the influence of multiple parameters such as the platform offset, set-down and tendon dynamics [7, 11, 12, 16].

Even though there has been significant research into the effects of abnormal waves on ships and offshore structures, many challenges remain [21]. The simplest way to investigate wave-in-deck impact problems is a simplified rigid model where the deck structure is idealised as a flat plate or as a box-shape [13, 22-32]. Current design practices [7, 8, 33] recommend several theoretical approaches such as the global/silhouette approach [8] and a detailed component approach, e.g. the momentum method [34, 35], to evaluate the wave-in-deck loads acting on fixed offshore platforms. However, such engineering approaches rely on potential flow theory. This theory simplifies the analysis by assuming an incompressible fluid with a free surface to derive global loads from the change of fluid momentum during the wave impact, using wave kinematics of a non-disturbed wave field. The effects of diffraction and entrapped air are therefore neglected, both effects that can strongly influence the platform behaviour and loads.

Scharnke *et al.* [36] reported that the load model recommended by the American Petroleum Institute (API) [7, 8] underestimates the measured horizontal wave-in-deck loads on a fixed deck of jacket platform in both regular and irregular wave tests. Even though the API loading model used wave kinematics obtained by Stokes fifth order wave theory, the underestimation of the loads was severe, particularly in irregular waves [36]. The momentum

method was also found to underestimate the magnitude of the wave-in-deck forces on a fixed horizontal deck subjected to unidirectional regular waves [22, 23].

A more complex investigation of the phenomenon should include the effect of columns on the magnitude and distributions of the deck loads. Scharnke and Hennig [13] investigated the effect of substructures on the magnitude of wave-in-deck loads by attaching a fixed box-type deck structure to a square column. The authors concluded that the column presence significantly increases the magnitude of global vertical forces and local pressures.

The current engineering knowledge required to accurately predict the magnitude and distribution of wave-in-deck loads and the resulting global response of floating structures such TLPs and semisubmersibles remains limited. This fact is reflected in the very limited number of papers reporting on model tests of typical multi-column floaters currently available in the open literature. Johannessen *et al.* [20] and Hennig *et al.* [19] investigated the dynamic air gap, wave loads and floating platform response under extreme wave conditions. Both investigations reported that a wave-in-deck event can lead to an additional extreme response mechanism and a step change in the extreme loading magnitude. It must be noted that complete and detailed results of these types of experiments are usually subjected to project confidentiality requirements and are therefore not available in the public domain.

Model tests are arguably the best approach for estimating wave-in-deck loads [36]. However, model testing is costly, time-consuming and involves several drawbacks such as scaling effects. It is therefore not surprising that computational fluid dynamics (CFD) based methods used for calculating wave-induced loads on offshore structures have received an increasing amount of attention in recent years. Commonly used commercial codes such as STAR-CCM+ and ANSYS FLUENT are available for modelling and solving wave-in-deck impact problems using the volume of fluid (VOF) method to capture free-surface hydrodynamic flows [37, 38].

There is a large body of work on CFD investigations of wave impact loads on fixed deck structures [28, 32, 39-42]. However, very little work on fixed multi-column and floating structures has been reported to date. Iwanowski *et al.* [43] and Lee *et al.* [44] investigated the air gap of a simplified, fixed semisubmersible with a full-scale static deck clearance of 18 m. CFD-based codes including ComFLOW [43] and CD-adapco STAR-CCM+ [44] were employed at full-scale dimensions to generate regular waves with the aid of the free surface VOF method. The computed wave run-up and wave impact pressures on the platform's columns were compared against model tests [43]. The authors observed a large variation in peak pressures for different wave events in both experimental and numerical tests which led

them to conclude that the peak magnitude of the impact pressure is an extremely localised phenomenon in both time and space.

There have been even fewer numerical investigations on floating TLPs [45-48]. Buchner and Bunnik [45] employed an improved VOF (iVOF) method implemented in ComFLOW for solving the dynamic response of the SNORRE-A TLP subjected to extreme regular waves. Rudman and Cleary [46], Rudman and Cleary [47] employed the Smoothed Particle Hydrodynamics (SPH) technique to simulate the fully non-linear dynamics of a large breaking wave hitting a TLP. These numerical studies [45-47] were not validated against model tests. Wu *et al.* [48] conducted a numerical study using STAR-CCM+ to investigate the air gap of a TLP under irregular extreme waves by applying the same input wave signal used in the model test. Each wave signal required 20 or more iterations in order to achieve a satisfactory match between measurements and numerical results. This implies that their proposed CFD technique is still too time expensive to be used for practical applications [28].

Recently, a robust overset grid technique was used by Wu *et al.* [48] and Chen *et al.* [49] to allow for numerical models with six degrees of freedom (6DOF). Unlike traditional mesh techniques such as dynamic mesh or sliding mesh, the mesh in the overset grid technique does not deform and thereby remeshing is not required. The method can therefore be employed with adequate numerical stability for modelling large amplitude motions such is the case of the surge motion in TLPs. Nevertheless, any new CFD simulation technique can only be trusted by the industry if its results have been thoroughly validated against experimental data first [41].

Based on the challenges remaining in the problem of wave-in-deck impact on offshore structures discussed above, the following research gaps have been identified:

- There is still considerable uncertainty about the magnitude and distribution of wave impact loads on structural deck elements near the free-surface.
- Effects of the columns of the floating platform on the wave-in-deck forces have not been systematically studied
- The measurement, estimation and simulation of local pressures due to wave-in-deck impact events on all types of offshore structures remains challenging.
- Accurate measurements and prediction of global loads and dynamic response of floating offshore structures due to wave-in-deck impact events is extremely limited.

- Combined numerical-experimental wave-in-deck investigations on floating offshore structures are not currently available in the open literature.

1.3. Research Objectives

This work aims at a better understanding of the problem of wave-in-deck impact on fixed and floating offshore platforms. The specific research objectives of this work are:

1. to establish an appropriate testing procedure to reliably measure the global and local effects in wave-in-deck experiments due to extreme wave impacts associated with a 10,000-year cyclonic sea state;
2. to investigate the effect of deck clearance reduction on the magnitude of global and local wave-in-deck loads on fixed offshore platforms;
3. to investigate pressure distribution at the deck underside of an offshore structure due to wave-in-deck impact events;
4. to examine the behaviour of a floating platform (compliant TLP) caused by a wave-in-deck impact event; and
5. to validate two-phase flow numerical models and assess their reliability in predicting global and local wave-in-deck loading and response of a compliant TLP.

1.4. Research Questions

The research questions answered by this work are:

1. How can the uncertainty about wave-in-deck loads be minimised? And what is the contribution of the structural dynamic response of the model test rig into the global forces measured in the model tests?
2. What are the changes in the magnitudes of global forces, and in the local wave-in-deck loads acting on fixed structures when the deck clearance is reduced?
3. How are wave-in-deck slam pressures distributed on the deck underside of an offshore structure?
4. What are the consequences of a wave-in-deck impact event on the dynamic behaviour of a compliant TLP, in terms of the platform motions, tendon tensions and slam pressures?
5. When using a proprietary CFD code based on the VOF method, what accuracy can be achieved for the prediction of the global loads and responses of a TLP model in a moderate water depth, when it is subjected to unidirectional regular waves?

1.5. Scope and Limitations of the Study

The scope of this study was limited to investigating problems of wave-in-deck impact in offshore structures. Experimental investigations were conducted in the Australian Maritime College (AMC) towing tank (100 m × 3.55 m × 1.5 m) at a model scale of 1:125 to examine extreme wave events associated with a 10,000-year tropical cyclonic condition at the Australian NWS and their impacts on different types of offshore structures. The selected prototype structure was SNORRE-A tension leg platform installed in 1992 at a water depth of 310 m in the Norwegian North Sea [50]. A scale of 1:125 was selected as a compromise among the AMC tank dimensions, wavemaker capability and the capacity of the instrumentations available during the time of this study. As the objective of the present investigation was to obtain an insight in typical wave-in-deck events (at small air gaps), the deck clearance (freeboard) of the prototype structure was not modelled to scale (reduced to 15 m at full scale, 120 mm at model scale). A deck clearance of 15 m at full scale for floating offshore structures is considered realistic, see e.g., [13, 28, 43, 44, 46, 47].

The investigated structures included a fixed platform deck, a fixed multicolumn platform (rigidly mounted TLP) and a compliant TLP, all subjected to long-crested irregular waves, as shown in Figure 1-4. The compliant TLP model was also subjected to several deterministic unidirectional regular waves aimed at validating two-phase flow numerical CFD models. The scope of each experimental investigation and the combined experimental-numerical investigation are given below:

1. Experimental results of the model tests conducted on the fixed platform deck structure (presented in Chapter 2) included wave elevations, global horizontal and vertical wave-in-deck forces and localised slamming pressures at the deck underside. The response of the model was also monitored using an accelerometer such that the contribution of structural dynamic response into the load cell response was efficiently identified. The effect of deck clearance reduction on the magnitude of global and local wave-in-deck loads was obtained.
2. Experimental results of the model tests conducted on the fixed multicolumn structure (presented in Chapter 3) included wave elevations, global wave impact forces and localised slamming pressures at the deck underside. Similarly, the contribution of inertial force effects due to the model's dynamic response into the load cell response was identified. The effect of deck

clearance reduction on the magnitude of global wave impact forces and local wave-in-deck loads was also examined.

3. Experimental results of the model tests conducted on the compliant TLP (presented in Chapter 4) included wave elevations, tendon tensile forces and localised slamming pressures at the deck underside. The platform tendons were modelled by light wires connected to custom extension coil springs manufactured to represent the appropriate scaled axial stiffness. The use of such an assembly implies that gravity and hydrodynamic loads acting on the tendon are neglected in model tests. Risers were not modelled in the experiments, yet, their tension was included as a lumped mass. The surge motion of the model was also measured such that new insights into the model dynamics during extreme wave deck impact were obtained. The effect of deck impact on the magnitude and dynamics of tendon tensions were obtained.

Fixed Deck Model	Fixed Multicolumn Model	Compliant TLP Model
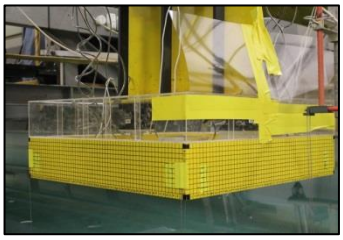	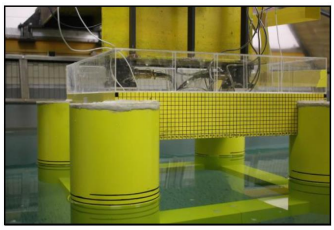	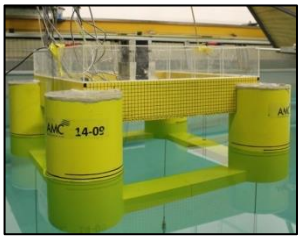
Measurements: ▪ Wave elevations. ▪ Global wave-in-deck forces. ▪ Localised slamming pressures. ▪ Deck accelerations.	**Measurements:** ▪ Wave elevations. ▪ Global wave impact forces. ▪ Localised slamming pressures. ▪ Deck accelerations.	**Measurements:** ▪ Wave elevations. ▪ Tendon tensions. ▪ Localised slamming pressures. ▪ Surge motion

Figure 1-4: Types of experiments conducted in this study.

4. The compliant TLP model subjected to unidirectional regular waves (presented in Chapter 5) provided both experimental and numerical results. The commercial CFD code STAR-CCM+ was used to investigate the characteristics of unidirectional regular wave impact on the model. The overset grid technique was used to model rigid body motions. The TLP tendons were modelled using massless spring lines. The numerical results of

surge motions, tendon tensions and deck slamming pressures were validated against the measurements acquired in model tests.

5. Additional CFD simulations of fixed deck structures and a multicolumn platform subjected to unidirectional regular waves were conducted and included in the thesis appendices.

1.6. Thesis Organisation

This thesis is comprised of four main chapters compiled from two journal articles that have been accepted for publication and two other articles currently under review. The relevant publishing details are given at the beginning of each chapter. A flowchart of the research conducted during this PhD study is presented in Figure 1-5. An outline of each chapter and its contribution to the research objectives is given below:

- Chapter 2 presents model test results of long-crested irregular wave tests conducted on a fixed platform deck. These results include global and local wave-in-deck loads. The effect of deck clearance reduction on the load magnitude is discussed. **Research objectives 1 – 3** are addressed in this chapter.
- Chapter 3 presents model test results of long-crested irregular wave tests conducted on a fixed multicolumn platform (rigid TLP). These results include global wave impact loads and localised wave-in-deck slam pressures. The effect of deck clearance reduction on the magnitude of global forces and localised wave-in-deck slam pressures is discussed. **Research objectives 1 – 3** are addressed in this chapter.
- Chapter 4 presents model test results of long-crested irregular wave tests conducted on a compliant TLP. These results include surge motions, tendon tensions and localised wave-in-deck slam pressures. The dynamic behaviour of the model due to a wave-in-deck impact event is discussed. **Research objectives 1 – 4** are addressed in this chapter.
- Chapter 5 presents comparisons of CFD and experimental results of unidirectional regular wave tests conducted on a compliant TLP. These results include surge motions, tendon tensions and localised wave-in-deck slam pressures. The effect of numerical parameters such as mesh density and air

compressibility on the magnitude of the computed impact pressure is discussed. **Research objectives 1 – 5** are addressed in this chapter.

- Chapter 6 presents the main research conclusions of this work and recommendations for future work.
- Appendix A presents additional experimental data for chapter 4.
- Appendix B is a peer-reviewed conference paper presented at the 24th International Offshore and Polar Engineering (ISOPE) Conference. The paper presented numerical and experimental results of unidirectional regular wave tests conducted on a fixed deck structure.
- Appendix C is a peer-reviewed conference paper presented at the 19th Australasian Fluid Mechanics Conference (AFMC). The paper presented numerical and experimental results of unidirectional regular wave tests conducted on a fixed deck structure.
- Appendix D a peer-reviewed conference paper submitted to the 12th International Offshore and Polar Engineering (ISOPE) Pacific/Asia Offshore Mechanics Symposium (PACOMS). The paper presented numerical and experimental results of unidirectional regular wave tests conducted on a fixed multi-column platform.

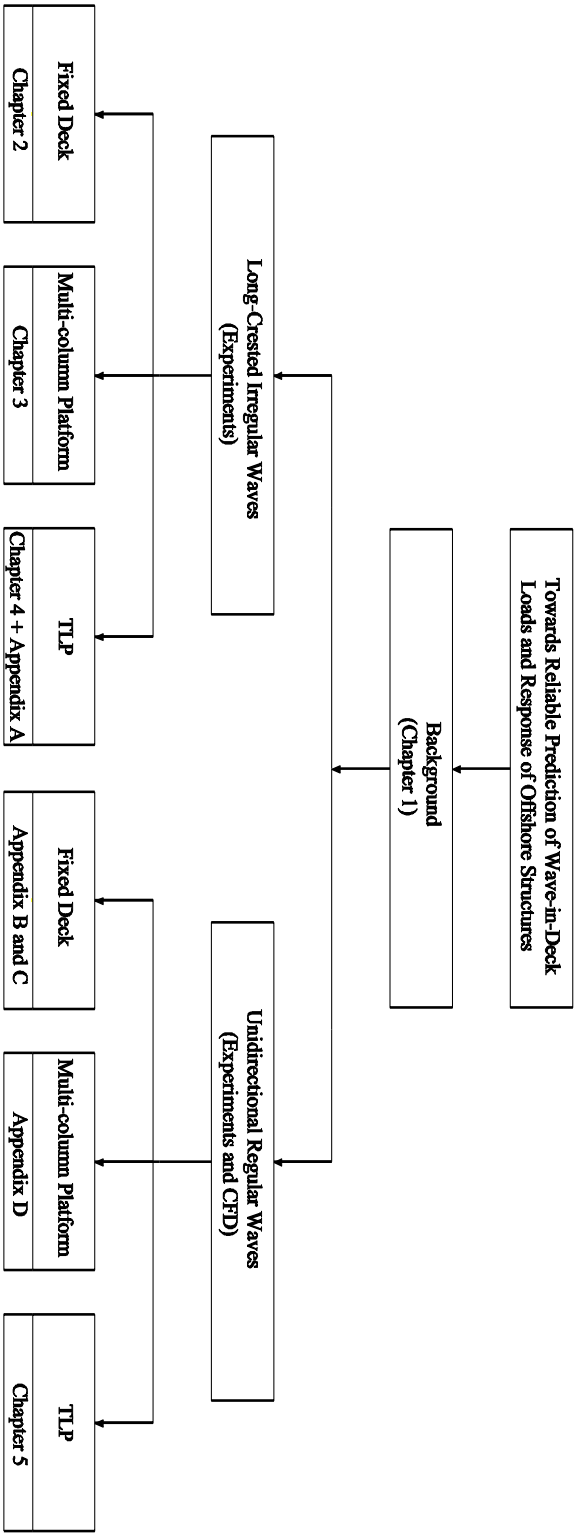

Figure 1-5: A flowchart showing thesis organisation.

Chapter 2: Measurements of global and local effects of wave impact on a fixed platform deck

This work presented in this chapter has been accepted for publication in *Proceedings of the Institution of Mechanical Engineers, Part M: Journal of Engineers for the Maritime Environment*. The paper has been edited for inclusion into this thesis to avoid repetition and to improve readability. The citation for this research article is:

Nagi Abdussamie, Roberto Ojeda, Giles Thomas and Walid Amin (2016). "Measurements of global and local effects of wave impact on a fixed platform deck", *Proceedings of the Institution of Mechanical Engineers, Part M: Journal of Engineers for the Maritime Environment.*

2.1. Scope

As specified in Chapter 1, the objective of this chapter is to analyse the characteristics of extreme long-crested irregular waves and their impacts on a three-dimensional fixed deck structure using a series of model experiments. The model tests were conducted in the towing tank of the AMC to measure both the global and local force effects of extreme wave events on the deck structure. The horizontal and vertical wave-in-deck forces due to a number of extreme waves were simultaneously measured with the localised slam pressures along and across the deck underside and the wave elevation in the vicinity of the model. The role of the dynamic response of the deck structure was identified by monitoring the acceleration components during wave impact tests. Measurement repeatability was analysed and the observed variations in forces and pressures are discussed. The effect of the deck clearance reduction on the peak forces and impact pressures was also examined.

2.2. Experimental investigation

A series of model tests was conducted at the AMC towing tank which is 100 m long, 3.55 m wide and 1.5 m deep. It is equipped at one end with a hydraulically driven flap-type wavemaker and has an artificial beach located at the opposite end of the tank to minimise wave reflections.

2.2.1. Test model and instrumentation details

The topside platform deck structure of a TLP was modelled using a flat horizontal box-shaped deck with external dimensions of length (L) = 608 mm, breadth (B) = 608 mm and depth (h) = 210 mm. The box dimensions were selected to represent, at a scale of 1:125, the 76 m × 76 m centre to centre spacing between columns of the SNORRE-A tension leg platform (TLP) installed in 1992 at a water depth of 310 m in the Norwegian North Sea [50].

The model deck was fabricated using a 10 mm thick aluminium plate for the bottom and 100 mm × 25 mm × 2.5 mm rectangular hollow sections (RHS) aluminium extrusions for the sides. The thickness of the model deck plate was selected using a finite element simulation to minimise the out of plane deformations so that the elastic effects could be neglected. Since the purpose of the testing was to measure wave slamming loads on the front and bottom faces of the deck structure without overtopping, a 100 mm high acrylic sheet was installed on top of the RHS to prevent water from splashing onto the internal deck space as shown in Figure 2-1. The deck was elevated above the water surface at a distance

representing the still-water air gap, i.e., deck clearance. The effect of set-down was examined by reducing the original deck clearance.

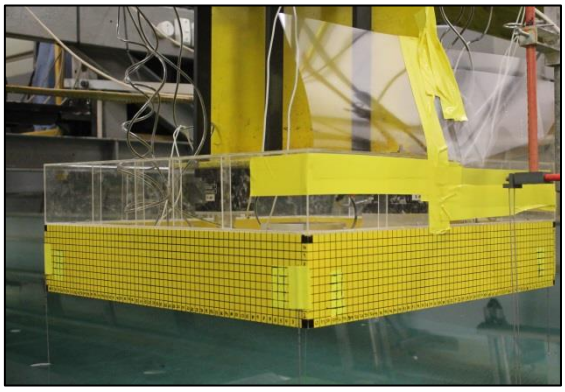

Figure 2-1: Photograph of the deck model positioned above the water surface.

Recent experimental studies [23, 36] have shown that a considerable dynamic response in force measurements is introduced when a fixed deck model is directly attached to a towing tank carriage. To minimise this undesired effect the stiffness and rigidity of the system was improved by attaching the model to a 4500 mm long steel H-beam (334 mm × 170 mm × 6/11 mm) mounted on the tank rails and placed 15 m away from the wavemaker as shown in Figure 2-2. The remaining 85 m of towing tank allowed for sufficiently long run times without interference from reflected waves travelling back up the tank [51]. The deck model was then supported by two load cells (LC1 and LC2) connected to a vertical 510 mm long I-beam (360 mm × 170 mm × 6/10 mm) suspended from the H-beam.

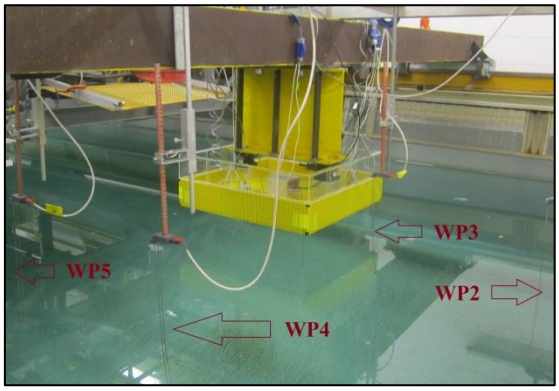

Figure 2-2: Experimental setup showing the deck structure attached to an I-beam under the H-beam across the towing tank, with WP2 – WP5 in the vicinity of the model (wave propagating from right to left).

2.2.2. Deck clearance

Wave-in-deck impact events occur when the dynamic air gap reduces to zero, as a result of either a reduction in the static air gap, i.e., deck clearance or when an extreme wave exceeds

the deck clearance. Three deck clearances were nominated based on the platform's loading conditions, as shown in Figure 2-3 at model scale with the *z*-coordinate vertical and positive upward. Scenario 1 is equivalent to the operating draft of SNORRE-A at normal condition. Scenarios 2 and 3 were designed to investigate the effect of static set-down (or increase in the platform's draft) on the magnitude of wave-in-deck forces. Such an increase in the platform's operating draft can be caused by tension increase in the tethers. The resulting deck clearances measured from still water level to the deck underside are 120 mm (15 m full scale), 110 mm (13.75 m full scale) and 100 mm (12.5 m full scale). The 10 mm reduction in deck clearance, which is equivalent to 1.25 m at full scale, could realistically occur during a platform's lifetime due to platform settlement, set-down or sea level rise [52-54]. It is assumed that the deck's underside will be in a flat position in relation to the water surface.

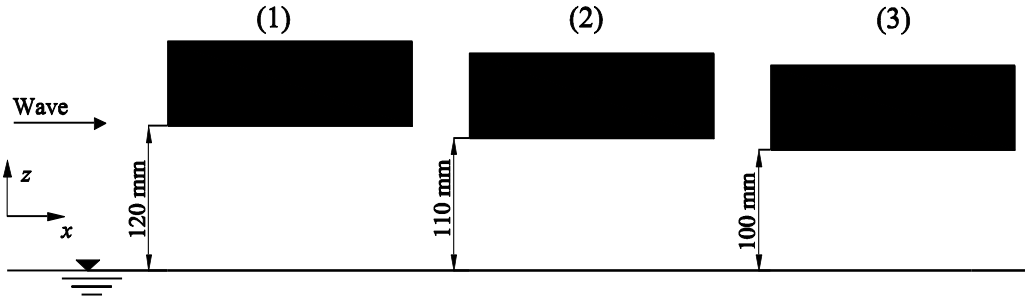

Figure 2-3: Profile views showing three deck clearances measured from the still-water line: (1) original deck clearance (scenario 1); (2) scenario 2; (3) scenario 3.

The deck clearance adjustment was performed by moving the deck up and down using four finely threaded rods and nuts, as illustrated in Figure 2-4, and connecting both beams (H-beam and I-beam) so that the deck alignment in the *xy* plane relative to the water surface could be controlled.

2.2.3. Measurement of wave elevation

Wave surface elevations were measured using five capacitance-type wave probes; denoted as WP in Figure 2-5. The location of each wave probe is presented in Table 2-1 defined from the origin point located at the model's geometric centroid. During all tank experiments, a constant water depth of 1.5 m was maintained. The wave height of incoming/incident waves, travelling in positive *x*-direction along the tank, was measured by WP1 and WP2. Before the impact tests were conducted, the change in crest height through the test section was investigated by using WP3 through WP5 without the deck structure in place. During the impact tests the wave height at the leading edge (LE) and trailing edge (TE) of the deck were

simultaneously measured by WP4 and WP5 so that the disturbed wave profile due to the presence of the deck could be recorded. Meanwhile, the undisturbed profile of the incoming wave at the centreline in front of the deck was measured by WP2.

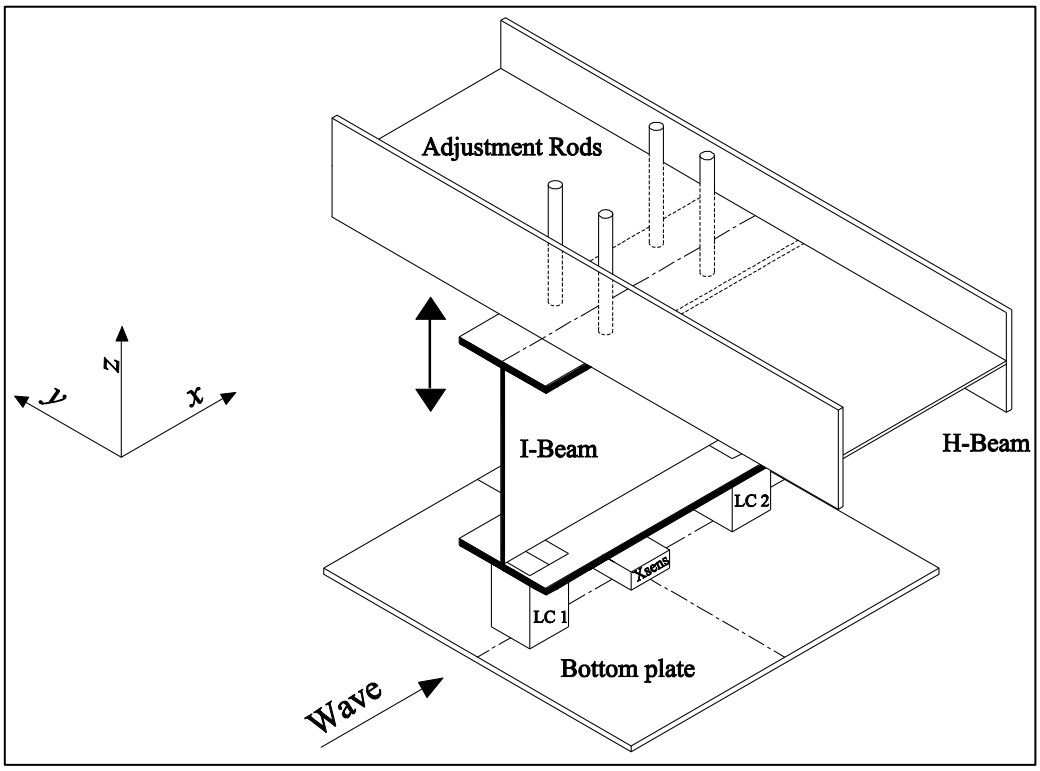

Figure 2-4: Isometric view of model attachment and method of adjustment of deck clearance.

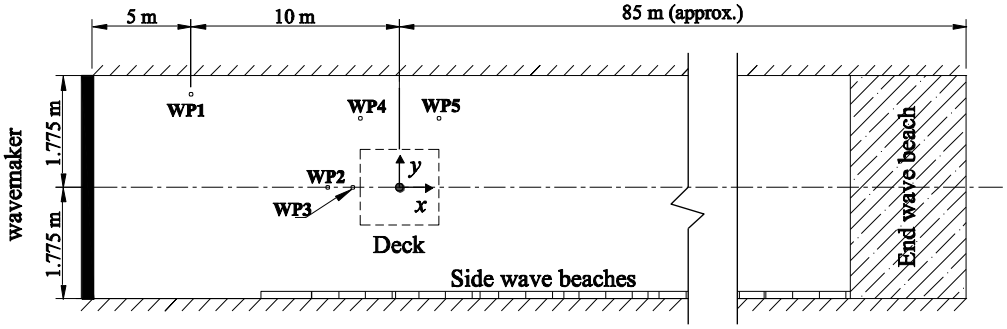

Figure 2-5: Schematic diagram (plan view) of the AMC towing tank showing the distribution of wave probes (WP) [not to scale].

Table 2-1: Location of wave probes with respect to the model's centroid.

Wave probe (WP)	Location (x, y) (m)
1	(-10.000, 0.500)
2	(-1.000, 0.000)
3	(-0.404, 0.000)
4	(-0.304, 1.200) at LE
5	(0.304, 1.200) at TE

2.2.4. Measurements of wave-in-deck loads

In this work, both global and local effects of wave-in-deck impact loading were investigated. Two load cells were used to measure the global forces generated due to the impact of the wave crest against the deck structure. The layout of the two AMTI MC3A-100 load cells, denoted by LC1 and LC2, is illustrated in Figure 2-6. Each load cell has a square base of 76 mm × 76 mm and was connected to the deck using a hinge for LC1 and a slider for LC2. This meant that the total vertical force, F_z, was measured by both load cells whilst the horizontal force, F_x, was measured by the forward load cell LC1 only. In order to monitor the deck acceleration components, an MTi-30 Xsens accelerometer was installed in the middle of the bottom plate.

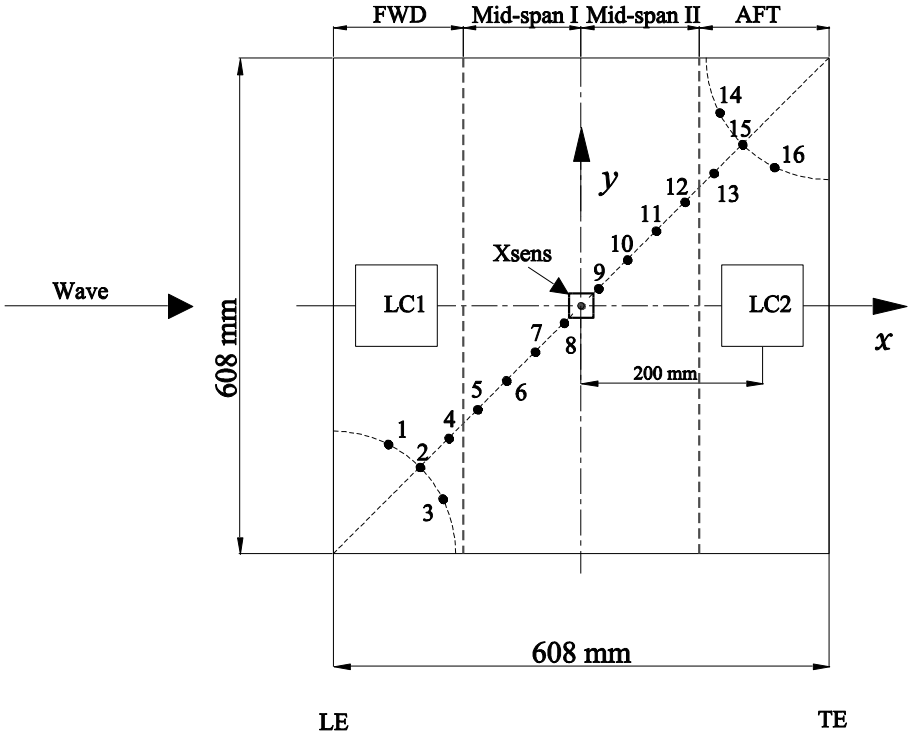

Figure 2-6: Distribution of pressure transducers and load cells (LC) on the deck underside [not to scale].

The localised slamming pressures were measured using sixteen piezoresistive pressure transducers (five Endevco 8510C-50, three Endevco 8510B-2 and eight Measurex MRV21-0.5). These pressure transducers have a high resonance frequency, making them suitable for the measurement of slamming pressures [22]. The tip of each transducer, which has a diameter of approximately 4 mm, was mounted flush with the underside of the deck. As can be seen in Figure 2-6 and Table 2-2, the pressure transducers (denoted as PT) were placed along the diagonal of the bottom plate. PT#1 was located close to the leading edge

(LE) whilst PT#16 was located near the trailing edge (TE). PT#3 and PT#14 were installed to measure slamming pressures near the deck edges; especially to capture the aeration process that may take place. The remaining pressure transducers, PT#1 through PT#15, were arranged diagonally so that pressure distribution in the *xy* plane could be obtained. This arrangement resulted in four regions fitted with four pressure transducers each (Table 2-3). A sampling frequency of 20 kHz was chosen for all channels (including wave probes) in order to capture the short-duration slamming pressures [7]. This high sampling frequency, with a total of twenty-four channels being recorded, limited the data acquisition time to approximately 40 s due to software memory constraints.

Table 2-2: Specifications and coordinates of pressure transducers (PT).

PT#	Model	Sensitivity (mV/kPa)	Range (kPa)	Location (*x*, *y*) relative to model's centroid (mm)
1	8510B-2	16.650	0 – 13.8	(-237, -170)
2	8510B-2	19.095	0 – 13.8	(-198, -198)
3	MRV21-0.5	1.038	0 – 50.0	(-170, -237)
4	MRV21-0.5	1.042	0 – 50.0	(-163, -163)
5	MRV21-0.5	1.036	0 – 50.0	(-127, -127)
6	8510C-50	0.662	0 – 344.0	(-92, -92)
7	MRV21-0.5	1.051	0 – 50.0	(-57, -57)
8	8510C-50	0.670	0 – 344.0	(-21, -21)
9	8510C-50	0.731	0 – 344.0	(21, 21)
10	MRV21-0.5	1.035	0 – 50.0	(57, 57)
11	8510C-50	0.701	0 – 344.0	(92, 92)
12	MRV21-0.5	1.110	0 – 50.0	(127, 127)
13	MRV21-0.5	1.021	0 – 50.0	(163, 163)
14	MRV21-0.5	1.091	0 – 50.0	(170, 237)
15	8510B-2	17.500	0 – 13.8	(198, 198)
16	8510C-50	0.665	0 – 344.0	(237, 170)

Table 2-3: The examined regions along the bottom plate.

Region	Pressure Transducers (PT)
FWD – LE	1, 2, 3, 4
Mid-span I	5, 6, 7, 8
Mid-span II	9, 10, 11, 12
AFT – TE	13, 14, 15, 16

The selection of load cells and pressure transducers was made based on a preliminary CFD study with the deck model being at the lowest deigned deck clearance (a_0 = 100 mm) and subjected to an extreme regular wave condition (H = 240 mm and T = 1.52 s). The CFD

results were then used to design the location of pressure transducers and to select the minimum capacity of the required load cells.

2.3. Experimental procedure

The experiments were conducted using a combination of the following procedures:

- *Wave calibration tests* – carried out to identify the extreme waves within long-crested irregular wave trains without the model being in the tank.
- *Free oscillation tests* – to find the natural frequencies of the complete test system when subjected to free oscillation tests in air and in water.
- *Wave impact tests* – to measure the impact wave forces and localised slamming pressures. In addition, the deck accelerations were monitored to identify the structural dynamic response and its effect on the force magnitudes by estimating the inertial force contribution in the load cell responses.

2.3.1. Wave calibration tests

The wave calibration tests were conducted by measuring the wave elevation profile, using five wave probes spread longitudinally down the tank, whilst running long-crested irregular waves without the deck model in-place. The tank length and absence of the deck model instrumentation allowed for long data acquisition times with the wave probes being sampled at 200 Hz. Three long-crested irregular wave trains, with duration of 120 s each, were generated. The wave trains were representative of cyclonic conditions for a 10,000-year return period at the NWS of Australia with a significant wave height, H_s, of 177 mm (22.125 m full scale) and a peak wave period, T_p, of 1.52 s (17.0 s full scale). The JONSWAP spectrum with a peak shape parameter $\gamma = 1.0$, which in this case is identical to the Pierson-Moskowitz (PM) spectrum, was used to synthesise short-time wave trains using the towing tank wavemaker. The PM spectrum is commonly adopted formulation of the fully-developed wind generated wave elevation spectrum for different offshore locations [55].

Since a small change in crest height can lead to a considerable variation in the associated wave impact forces and slam pressures, accurate measurement of the wave height was critical [39]. Consequently, the wave crests of each wave event were identified from the measured wave elevation time histories with and without the deck structure (at different deck clearances, a_0). WP4 (at the LE) time histories were used to identify wave characteristics of the wave events of interest. An example is presented in Figure 2-7 where two wave events (denoted by WE#) in a single wave train were identified by analysing the wave elevation time

histories of WP4. This wave train contains WE#1 observed at time = 0.0 to 2.0 s and WE#2 at time = 12.0 to 13.5 s. Such extreme waves, approximately 27.5 m to 31.0 m high at full scale, can indeed occur in severe sea states. For instance, similar steep waves were measured by three wave radars on the *Marco Polo* tension leg platform during hurricane *Rita* in the Gulf of Mexico [56].

The generated waves had good repeatability using multiple runs at different values of a_0, with only a very minimal disturbance on crest height of WE#1 seen in Figure 2-7 (a) due to the presence of the deck structure. Nevertheless, the crest elevation of WE#2 was heightened by approximately 6% for all deck clearances when the deck was present, as shown in Figure 2-7 (b). Therefore, the wave crest measured simultaneously with wave impact forces and slamming pressures was used when investigating the relationship between the impacting waves and the associated wave-in-deck loads.

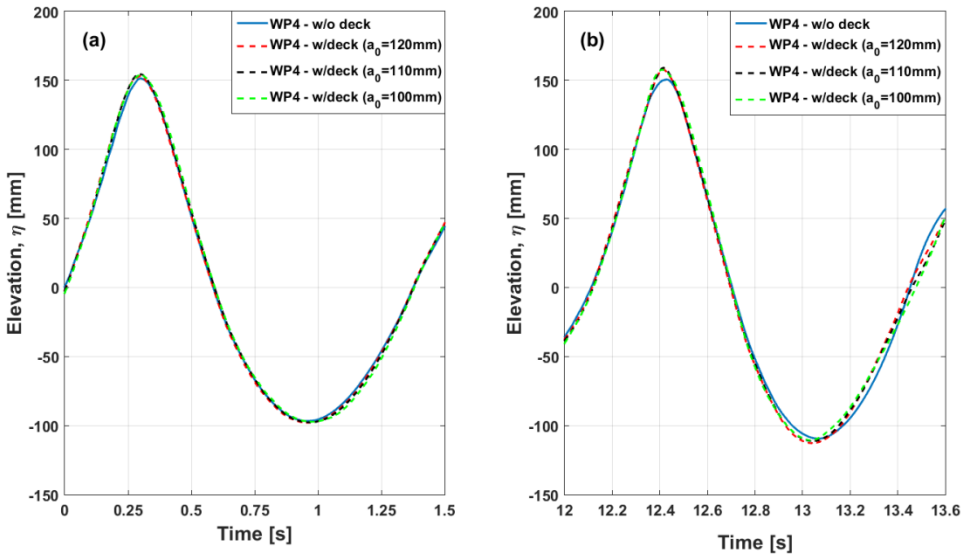

Figure 2-7: Time history of wave elevation at the deck leading edge measured by WP4 with and without the deck structure: (a) wave event WE#1; (b) wave event WE#2.

Figure 2-8 shows a fair match between the measured wave elevation of WE#1 at WP4, with the deck setup in the tank, and the theoretical one obtained based on Stokes second and fifth orders was achieved. However, the theoretical wave elevation failed to reproduce the non-linear behaviour at both wave crest and trough, underestimating the crest height and overestimating the trough amplitude. Besides, in terms of time-evolution both Stokes orders were found to be approximately identical but wider/broader than the measured WE#1.

The wave calibration procedure identified 12 wave events, which were then used in the wave impact tests. Each wave event is defined by wave height (H), wave crest height (η_c) and wave period (T_z) as summarised in Table 2-4. The zero up-crossing method was employed to estimate such parameters (Figure 2-9). In order to combine the effect of wave height and its period, the wave steepness, S, of each wave event was introduced using $S = H/\lambda$ in which λ is the wavelength estimated from the dispersion relationship.

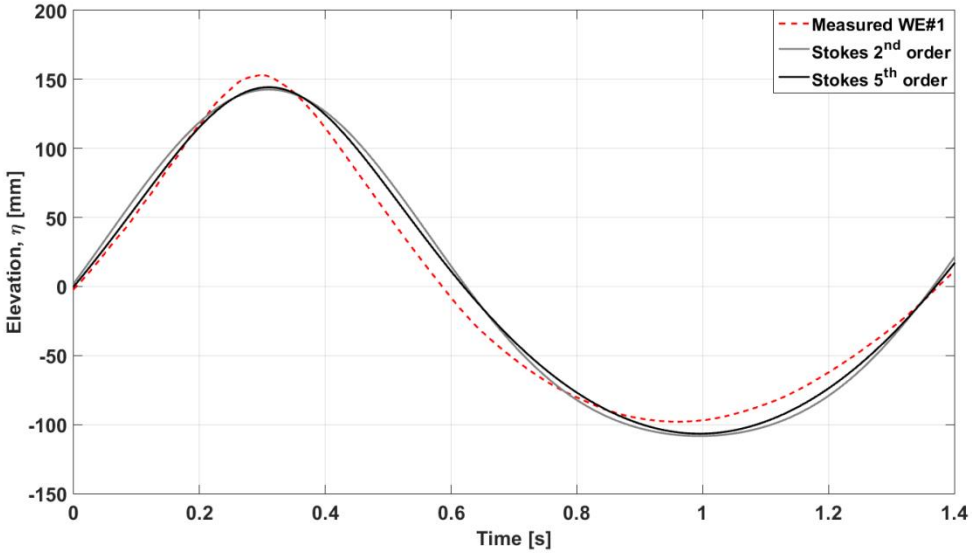

Figure 2-8: Time history of wave event WE#1 measured by WP4 and compared to Stokes wave theory.

The maximum wave steepness of the identified wave events was found to be approximately 0.10 (WE#5), i.e., non-breaking wave conditions. The parameter η_c/H was also introduced for each wave event. The phase celerity, $C = \lambda/T_z$, was estimated so that the resulting impact pressure could be related to the associated dynamic pressure ($0.5\rho C^2$).

In addition, since the magnitude of the peak horizontal force depends on the associated wave velocity, u, in the x-direction at the wave crest, the later was estimated using the Stokes second order wave kinematics [7] at $z = \eta_c$. Studying the information in Table 2-4, the crest height, η_c, of both WE#7 and WE#9 suggests that no impact can occur when the deck is elevated above such a height (a_0 = 120 mm or a_0 = 110 mm). However, it was observed that while WE#7 and WE#9 have a small crest height at the LE (WP4), both wave events hit the deck bottom at the rear section as the wave crest became larger as noted in the time history of WP5.

Table 2-4: Wave events (WE) and their parameters.

WE#	H (mm)	η_c (mm)	T_z (s)	λ (m)	C (m/s)	u (m/s)	S (-)	η_c/H (-)
1	251	153	1.37	2.92	2.13	0.803	0.086	0.61
2	271	158	1.33	2.76	2.08	0.920	0.098	0.58
3	213	129	1.51	3.53	2.34	0.560	0.060	0.61
4	190	138	1.74	4.58	2.63	0.420	0.041	0.73
5	242	163	1.23	2.36	1.92	0.950	0.103	0.67
6	198	130	1.24	2.40	1.94	0.710	0.083	0.66
7	184	112	1.2	2.25	1.88	0.660	0.082	0.61
8	249	166	1.49	3.44	2.31	0.720	0.072	0.67
9	157	90	1.95	5.55	2.85	0.290	0.028	0.57
10	168	118	1.2	2.25	1.88	0.610	0.075	0.70
11	190	112	1.11	1.92	1.73	0.780	0.100	0.59
12	154	104	1.78	4.76	2.67	0.320	0.032	0.68

These wave parameters can be obtained graphically, as shown in Figure 2-10, by mapping the wave event along subplots (a), (b) and (c) and using H_s = 177 mm and T_p = 1.52 s. The ratio of H/H_s for the observed wave events ranges from 0.87 (WE#12) to 1.53 (WE#2), whilst the wave crest to height ratio (η_c/H) was found to be between 0.57 (WE#9) and 0.73 (WE#4). The T_z/T_p ratio was estimated to be within 0.73 (WE#11) and 1.28 (WE#9).

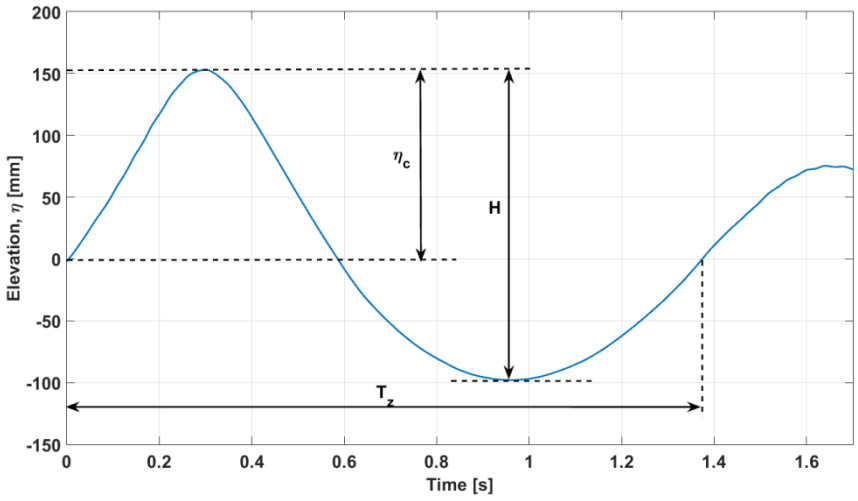

Figure 2-9: Estimated wave parameters of wave event WE#1 using the zero up-crossing method applied to WP4 time histories.

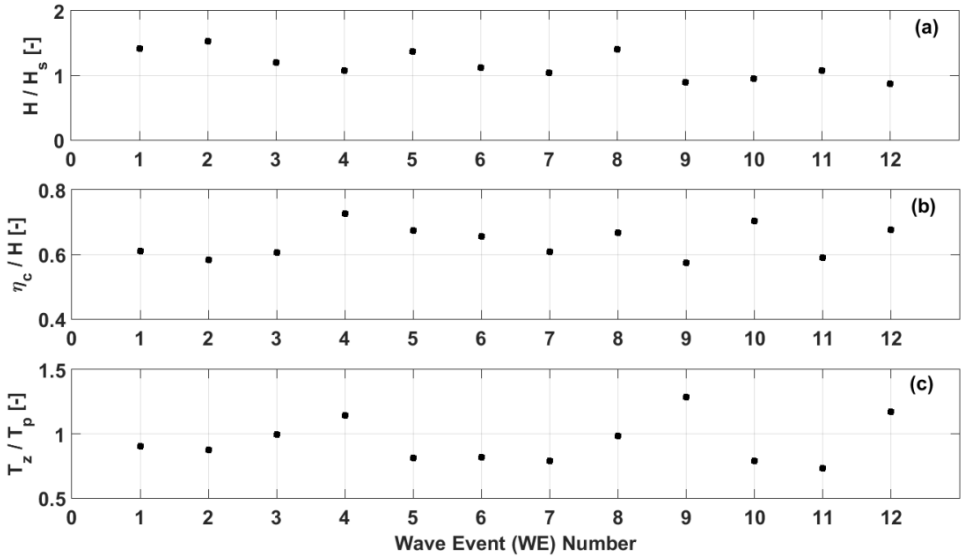

Figure 2-10: Wave parameters of measured extreme wave events (WE): (a) wave height ratio, H/Hs; (b) wave crest to height ratio, η_c/H; (c) wave period ratio, T_z/T_p.

2.3.2. Free oscillation tests

The full testing assembly (deck model, instruments and force supports) was subjected to a series of oscillatory decay tests. Dry and wet free oscillation tests were performed in order to identify the natural frequency of the system and the associated force contribution into the load cell signals due to the system's dynamics. The dry free oscillation tests were conducted with the deck positioned above the water surface, whereas the wet free oscillation tests were executed by lowering the model such that the deck underside was slightly touching the water surface. Free oscillation time traces were measured by means of the load cells and the MTi-30 Xsens accelerometer. The lowest natural frequencies (denoted as f_n) obtained in the dry and wet free oscillation tests are summarised in Table 2-5.

Table 2-5: The lowest natural frequencies, f_n, (Hz) obtained from free oscillation tests in air and in water.

Decay test	Medium (type)	f_n in x-direction (Hz)		f_n in z-direction (Hz)	
		Accelerometer	Load cell	Accelerometer	Load cell
1	Air (dry)	9.76	9.714	16.08	16.00
2	Water (wet)	10.20	10.18	14.66	14.50

A comparison between the results of the dry and wet free oscillation tests in the x-direction is made in the frequency domain using Fast Fourier Transform (FFT), as shown in Figure 2-11 (a).

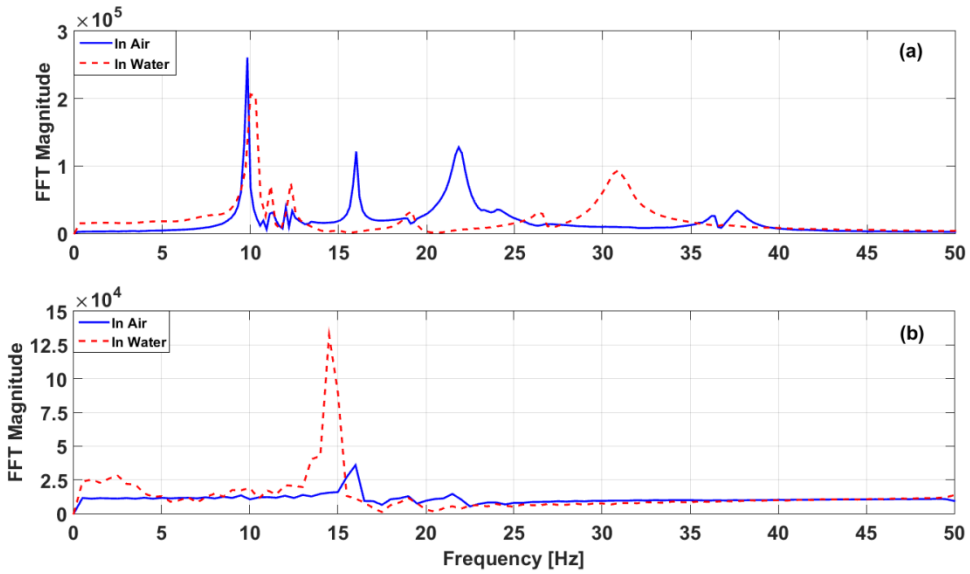

Figure 2-11: FFT results of free oscillation tests conducted in air and in water based on time traces of the load cells: (a) in the *x*-direction; (b) in the *z*-direction.

The second and the third modal frequencies obtained from the dry test (16.0 Hz and 21.8 Hz) are not present when the bottom plate of the deck is aligned on the water surface, due to the contribution of the relatively small added mass and viscous damping to the system. As shown in Figure 2-11 (b), the effect of water surrounding the bottom plate is more pronounced in the *z*-direction than in *x*-direction. The lowest natural frequency observed while the deck was tested in air (16.00 Hz) was found to reduce to 14.50 Hz.

The natural frequencies of the system (in both the *x* and *z* directions) did not coincide with the peak wave frequency of the incoming waves (0.51 – 0.90 Hz). Therefore, the inertial force due to the structural dynamic response can be assumed to be minimal and insignificant in the load cell responses.

2.3.3. Wave impact tests

A total of 29 conditions were tested as summarised in Table 2-6. In order to ensure the repeatability of the results each test condition was repeated 3 – 5 times resulting in a total of 138 runs such that approximately 2620 peaks were analysed and averaged to obtain reliable experimental data. The dynamic air gap ($a = a_0 - \eta_c$) was obtained for each condition. All test conditions, except 7, 16 and 26, show a negative air gap at the LE. Wave events WE#7 and WE#9 caused wave impact nearby the TE for conditions 7, 16 and 26.

Table 2-6: Test conditions.

Condition	WE#	H (mm)	η_c (mm)	T_z (s)	a_0 (mm)	a (mm)
1	1	251	153	1.37	120	-33
2	2	271	158	1.33	120	-38
3	3	213	129	1.51	120	-9
4	4	190	138	1.74	120	-18
5	5	242	163	1.23	120	-43
6	6	198	130	1.24	120	-10
7	7	184	112	1.20	120	8
8	8	249	166	1.49	120	-46
9	1	251	153	1.37	110	-43
10	2	271	158	1.33	110	-48
11	4	190	138	1.74	110	-28
12	5	242	163	1.23	110	-53
13	6	198	130	1.24	110	-20
14	7	184	112	1.20	110	-2
15	8	249	166	1.49	110	-56
16	9	157	90	1.95	110	20
17	10	168	118	1.20	110	-8
18	1	251	153	1.37	100	-53
19	2	271	158	1.33	100	-58
20	3	213	129	1.51	100	-29
21	4	190	138	1.74	100	-38
22	5	242	163	1.23	100	-63
23	6	198	130	1.24	100	-30
24	7	184	112	1.2	100	-12
25	8	249	166	1.49	100	-66
26	9	157	90	1.95	100	10
27	10	168	118	1.20	100	-18
28	11	190	112	1.11	100	-12
29	12	154	104	1.78	100	-4

2.4. Data analyses

Wave-in-deck forces in the x-direction (F_x) and z-direction (F_z) as well as localised pressures associated with the test conditions shown in Table 2-6 are presented and discussed in this section. Wave events WE#1 (H = 251 mm, η_c = 153 mm, T_z = 1.37 s) and WE#8 (H = 249 mm, η_c = 166 mm, T_z = 1.49 s), which were the most extreme wave events observed, were selected for detailed discussion in terms of uncertainty analyses.

2.4.1. Wave-in-deck forces

To assess the uncertainty in the experimental data, each test condition was repeated between 3 and 5 times. The peak values in the *x*- and *z*-direction measured in the multiple runs were then averaged to obtain a mean value. The force peaks in the *z*-direction were found for both the upward direction, $F_z(+)$, and the downward direction, $F_z(-)$. The peak values of the three force components, F_x, $F_z(+)$ and $F_z(-)$, measured for WE#1 are summarised in Table 2-7 for test conditions 1, 9 and 18 (see Table 2-6). For all the tabulated conditions, good repeatability can be seen for F_x and $F_z(+)$. However, significant variability was found in the values of $F_z(-)$ e.g., in condition 1 a relative difference of approximately 12% was obtained between Run 1 and Run 2. The associated peaks with WE#8 for test conditions 8, 15 and 25, the force peaks are obtained as given in Table 2-8. A good repeatability was also obtained amongst repeated runs in the three conditions. Hence, there is a sufficient confidence in the mean values. Nevertheless, a close investigation was done in regards to the dynamic response of the impacted deck structure and its effect on the magnitude of wave-in-deck forces.

Table 2-7: Wave event 1 (WE#1) force peaks [given in Newtons] measured using multiple runs for test conditions 1, 9 and 18.

Condition 1: H = 251 mm, η_c = 153 mm, T_z = 1.37 s, a_0 = 120 mm							
Component	Run 1	Run 2	Run 3	Run 4	Run 5	Mean	σ
F_x	12.7	11.9	12.4	11.7	12.0	12.1	0.40
$F_z(+)$	29.1	28.8	27.7	28.6	28.8	28.6	0.53
$F_z(-)$	-62.3	-70.5	-70.3	-70.4	-63.7	-67.4	4.08
Condition 9: H = 251 mm, η_c = 153 mm, T_z = 1.37 s, a_0 = 110 mm							
Component	Run 1	Run 2	Run 3	Run 4	Run 5	Mean	σ
F_x	15.7	15.8	14.7	15.5	15.9	15.5	0.48
$F_z(+)$	38.8	38.2	37.8	39.1	39.3	38.6	0.63
$F_z(-)$	-98.7	-80.2	-85.7	-97	-88.3	-90	7.78
Condition 18: H = 251 mm, η_c = 153 mm, T_z = 1.37 s, a_0 = 100 mm							
Component	Run 1	Run 2	Run 3	Run 4	Run 5	Mean	σ
F_x	24.6	24.7	24.2	24.6	25.1	24.6	0.32
$F_z(+)$	57.9	56.9	57.6	55.8	56.0	56.8	0.93
$F_z(-)$	-181	-104	-77.5	-103	-82.8	-109.7	41.60

2.4.2. Force time history

For condition 1, the horizontal and vertical wave-in-deck forces measured over each of the five runs for WE#1 and an air gap of 120 mm are shown in Figure 2-12 and Figure 2-13, respectively, with the time vectors manually synchronised.

Table 2-8: Wave event 8 (WE#8) force peaks [given in Newtons] measured using multiple runs for test conditions 8, 15 and 25.

Condition 8: H = 249 mm, η_c = 166 mm, T_z = 1.49 s, a_0 = 120 mm							
Component	Run 1	Run 2	Run 3	Run 4	Run 5	Mean	σ
F_x	63.1	63.2	55.4	53.2	51.2	57.2	5.61
F_z(+)	33.2	31.9	28.6	29.8	28.5	30.4	2.08
F_z(-)	-57.4	-58.9	-53.9	-57.7	-54.3	-56.4	2.21
Condition 15: H = 249 mm, η_c = 166 mm, T_z = 1.49 s, a_0 = 110 mm							
Component	Run 1	Run 2	Run 3	Run 4	Run 5	Mean	σ
F_x	55.2	66.2	57.9	69.3	60.7	61.9	5.82
F_z(+)	53.3	52.4	50.1	53.7	53.7	52.6	1.52
F_z(-)	-64.4	-70.1	-67	-69.8	-66.1	-67.5	2.44
Condition 25: H = 249 mm, η_c = 166 mm, T_z = 1.49 s, a_0 = 100 mm							
Component	Run 1	Run 2	Run 3	Run 4	Run 5	Mean	σ
F_x	80.9	67	77.1	78.4	71.9	75.1	5.22
F_z(+)	70.5	63.1	67.9	69.8	69.7	68.2	3.14
F_z(-)	-66.3	-64.2	-67.5	-62.6	-66.1	-65.3	2.15

Both time histories show an impulse-like impact, i.e., force magnitude sharply increased and then followed by a rapid decrease. It is clear that the dynamic response is more pronounced in the horizontal direction than in the vertical direction (Time = 16.25 – 17.50 s). This can be attributed to a combination of the direction of travel of the wave and the free horizontal motion at the slider attachment of LC2 of the deck model. However, this dynamic effect appears only after the main deck impact at approximately 16.1 s.

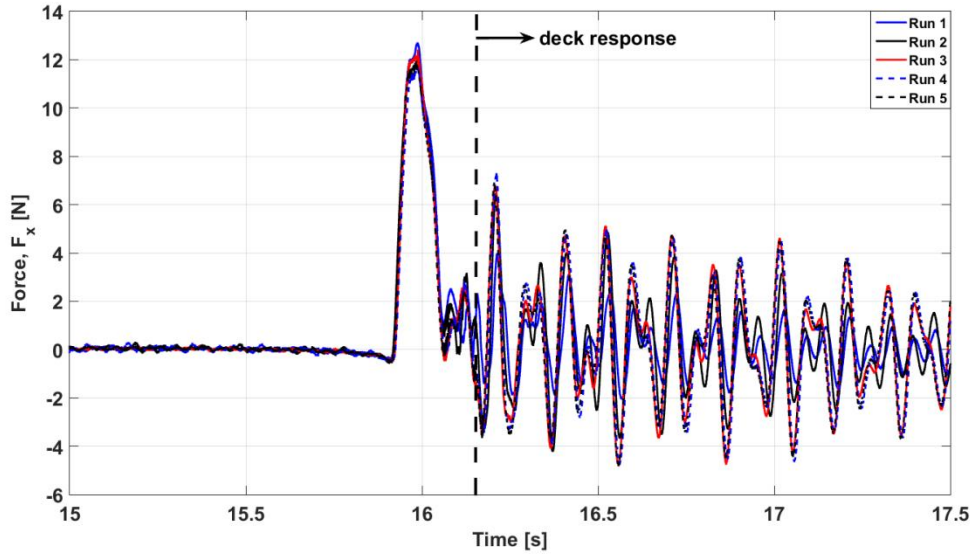

Figure 2-12: Time history of the horizontal force (F_x) for condition 1 [WE#1: H = 251 mm, T_z = 1.37 s at a_0 = 120 mm].

The ratio between the maxima of the horizontal and vertical upwards forces was found to be approximately 0.41. The vertical force signal, illustrated in Figure 2-13, has a large downward component; approximately double the upward component.

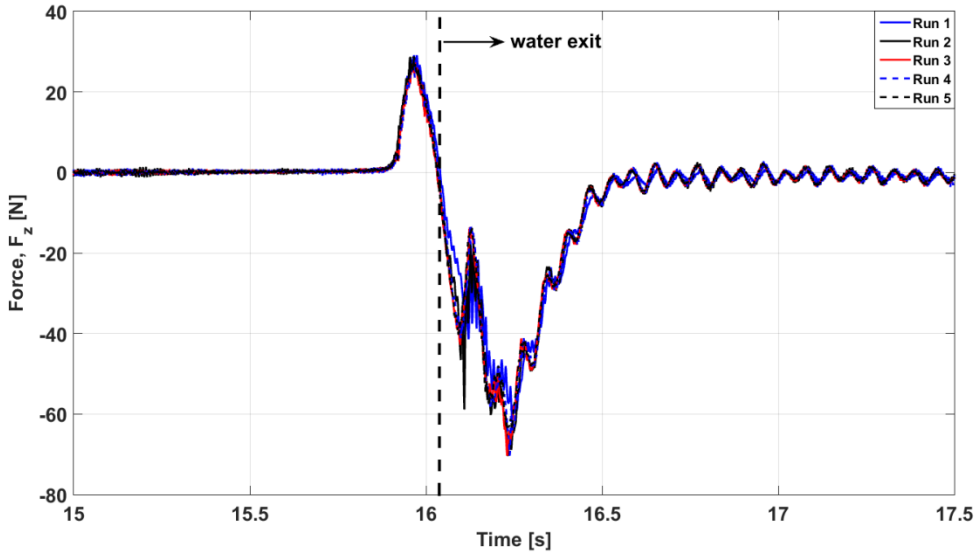

Figure 2-13: Time history of the vertical force (F_z) for condition 1 [WE#1: H = 251 mm, T_z = 1.37 s at a_0 = 120 mm].

Analysis of the video records of this event, as shown in Figure 2-14, suggests that the large magnitude of the downward force is related to the added mass surrounding the immersed deck structure, in both *x* and *z* directions. The figure clearly shows a substantial amount of water flowing downwards from the LE of the deck after the wave impact.

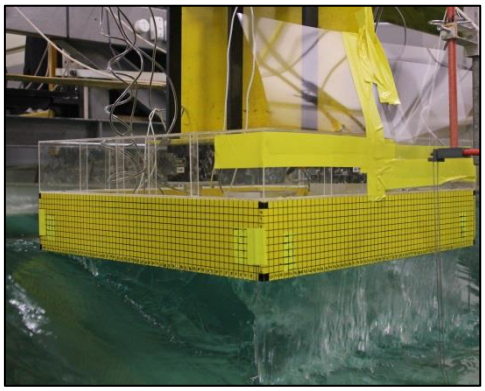

Figure 2-14: Photograph showing a substantial amount of water flowing downwards from the deck LE after the wave impact for condition 1 [WE#1: H = 251 mm, T_z = 1.37 s at a_0 = 120 mm].

Since the front face of the deck structure acted as a vertical wall against which the waves impact, the impacts may take a form akin to a breaking wave or jet-like impact. Subsequent to this impact a large amount of water contributed into the magnitude of the

downward F_z component (see Figure 2-14, water flowing down at the LE immediately after hitting the front face). In other words, the bottom plate of a box-type deck structure was impacted in a manner similar to a horizontal flat plate, except that the amount of water passing the plate (which causes the vertical wave-in-deck force F_z) was controlled by the magnitude of the horizontal force. This finding is in contrast with the theoretical models which assume that the deck structure is transparent to the impacting waves [35].

2.4.3. Identification of dynamic response

Impacting waves contain high-frequency energy components that cause the structure to respond at its modal frequencies [25, 36, 57, 58]. This impact-induced vibration can corrupt the real force measurements since the load cells records include the inertial force. Consequently, prior to determining the actual peaks of force data, the inertial force should be identified and removed from the measured signal. Whilst Winsor [58] describes various techniques suitable for removing the inertial force from measured force signals, the simplest method is using low-pass filtering. The characteristics (e.g., cut-off frequency) of the low-pass filter are often selected based on dry and wet free oscillation tests [27, 36, 59]. However, free oscillation tests do not accurately represent the actual wave-structure interaction and thus, the signal information may be misinterpreted or lost when filtering. An alternative is to use FFT to analyse the force signal in the frequency domain to remove high-frequency components that can be idealised as a single degree of freedom system. Nevertheless, an analysis of the spectral density of the impact generally contains frequencies attributed to multiple degrees of freedom. Therefore, as concluded by Winsor [58], neither of these techniques produce fully satisfactory results for the removal of the inertial force from the force signal.

Oberlies *et al.* [57] used a calibrated impulse hammer to compare the input force with the force response measured by the load cells on a model of a gravity-based structure. Oberlies *et al.* [57] found that the dynamics of the test rig during a hydrodynamic impact differed significantly from those obtained with the hammer test; this leads to questioning of the validity of using an impulse hammer to identify the inertial force.

In this work, in order to identify and remove the inertial forces (generally speaking, “remove the effect of the inertial forces”) from the measured force data, the following procedure was proposed:

- Firstly, dry and wet free oscillation tests were performed as discussed previously to obtain the natural frequency of the testing assembly (deck model, instruments and force supports).
- The next step was to investigate the magnitude of the inertial force during wave-in-deck impact events by recording the translational acceleration components in both the *x*- and *z*-direction using an accelerometer.
- The inertial force in the *x*- and *z*-direction could then be identified from the accelerometer signal in the time domain and its magnitude estimated using Newtown's second law as $m.a_x$ and $m.a_z$, respectively, where m is the structural mass of the deck model including support members (≈17.75 kg) and a_x and a_z are the horizontal and vertical peak accelerations measured during each wave impact event. The water added mass in both directions was neglected.
- Finally, the actual measured peaks of horizontal force F_x and vertical force F_z were obtained by subtracting the estimated inertial forces (F_{ix} and F_{iz}) due to the dynamic deck response from raw force values.

The original load cell signals and the estimated inertial forces, F_{ix} and F_{iz} in the *x*- and *z*-direction, are presented in Figure 2-15 (a) and (b), respectively, for condition 1 using Run 4. No dynamic response was noticed at the instant of wave impact (time ≈ 15.9 s); however the deck's dynamic response becomes visible at the water exit phase of WE#1 and thereafter (time = 16.1 s). This may be attributed to the applied force, i.e., water impact had an ideal instantaneous load step and therefore the system which was at rest will respond after a time delay.

This suggests that the deck structure started vibrating shortly after the wave slam event, which often elapses a very short duration. Therefore, the dynamic response had a minimal effect on the peak forces in F_x and the upward F_z. Beyond the water exit phase, the deck structure seems to continuously vibrate with a settling time exceeding 2.0 s. Such a long duration may not be tolerated for wave impact experiments, particularly when two successive large waves hit the model thereby the force time history of the second impact may be corrupted. In comparison with the load cell responses, the magnitude of inertial forces was reasonably estimated, as a result of product the structural mass in the magnitude of a_x and a_z, (Figure 2-15). This implies that the load cells detected the dynamic response of the deck structure introduced as an additional impact force. Since the dynamic response of the deck

structure had a minimal effect on the magnitude of wave-in-deck forces (although it had an effect on the force time history), peak values of force components were extracted from the raw data.

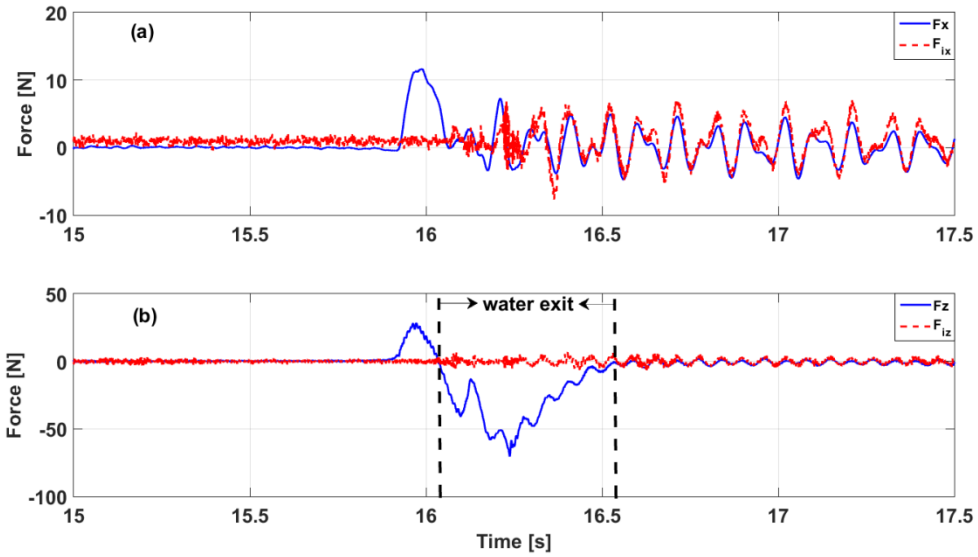

Figure 2-15: Time history of original (raw) forces and estimated inertial forces (F_{ix} and F_{iz}) associated with condition 1 [WE#1: H = 251 mm, T_z = 1.37 s at a_0 = 120 mm]: (a) x-direction; (b) z-direction.

2.4.4. Localised impact wave pressures

Figure 2-16 shows the time history of PT#1 in runs 1 and 2 for test condition 1 (WE#1, a_0 = 120 mm). Both runs had a similar trend in the uplift direction, i.e., positive cycle. Nevertheless, the first peak in Run 1 is significantly larger than the one measured in Run 2. In both runs, the duration of the positive pressures was found to be approximately 100 ms or 7% T_z (dots (1) and (2) are to denote the cycle end). In both runs, a double peak appeared before the actual slam event occurred, where this peak was more pronounced in Run 1 than Run 2. Such a peak might be caused by water separation at the deck leading edge (water momentum in the x- and z-direction), see Figure 2-14.

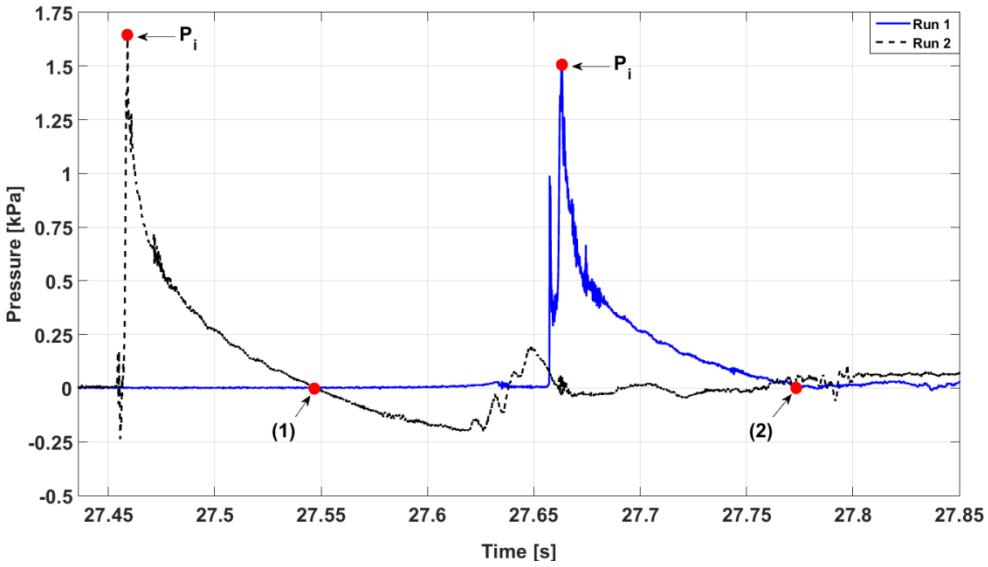

Figure 2-16: A typical time history of pressure signal measured by PT#1 in different runs for condition 1 [WE#1: H = 251 mm, T_z = 1.37 s at a_0 = 120 mm].

The ratio between the maximum positive pressures (impact pressure, Pi) in both runs was found to be 0.92 (almost an 8% difference). By using the area under each curve (impulse pressure), as suggested by Cooker [60], the ratio was reduced to 1.01 or only a 1% difference.

Uncertainty analysis of pressure measurements is introduced in this section by demonstrating the impact pressures associated with WE#1 measured in multiple runs for test conditions 1, 9 and 18. The pressure distribution along the bottom plate is presented using boxplots such that the variation among the different runs can be investigated. The maximum and minimum values, the first quartile (the 25th percentile) and third quartile (the 75th percentile), Q1 and Q3, as well as the median pressure values, measured in multiple runs, were combined into a single plot.

The associated impact pressures with conditions 1, 9 and 18 measured over repeated runs can be shown in Figure 2-17, Figure 2-18 and Figure 2-19, respectively. The vertical centreline between PT#8 and PT#9 denotes the geometric centroid (x = 0) of the bottom plate. The boxplot definition is given in the legend of each graph. The square symbol (▪) represents the mean value of peak pressures measured by a transducer in different runs.

In general, the front half of the bottom plate experienced larger pressures than the rear section. For condition 1 (Figure 2-17), the maximum peak pressure was captured by PT#1 with a mean value of approximately 2.38 kPa. Only PT#1, PT#11 and PT#15 detected outliers as depicted by cross marks (+). For condition 9 (Figure 2-18), the maximum peak pressure was also captured by PT#1 with a mean value of approximately 2.48 kPa, whilst for

condition 18 (Figure 2-19), the maximum peak pressure was captured by PT#8 (2.6 kPa) and PT#11 (2.7 kPa). In addition, the region near the TE (AFT-TE) seems to experience lower impact pressure, more pronounced at the location of PT#15.

Using boxplots indicated how the impact pressures vary amongst multiple runs having approximately an identical wave condition. The variation in impact pressures was examined by investigating the uncertainty attributed to the transducer itself, its location (which may be affected by side edges) as well as the deck clearance. Studying conditions 1, 9 and 18, the following findings were reached:

- The transducer uncertainty was tested as shown in Figure 2-16 by integrating the pressure with respect to time. As demonstrated above, the impulse pressure defined as integrated pressure did not largely vary among repeated runs.
- Side edges may affect the magnitude of impact pressures measured by the transducers PT#1, 2 and 15 and hence, outliers were detected.
- By reducing the deck clearance the interaction between a steep wave and the deck structure became stronger and more violent resulting in a wider range of impact pressures (max and min values in boxplots) e.g., PT#4, 5, 6, 8 and 10. To overcome this issue, a sufficient number of repeated runs, five or more runs per each test condition, were required during tanks experiments.

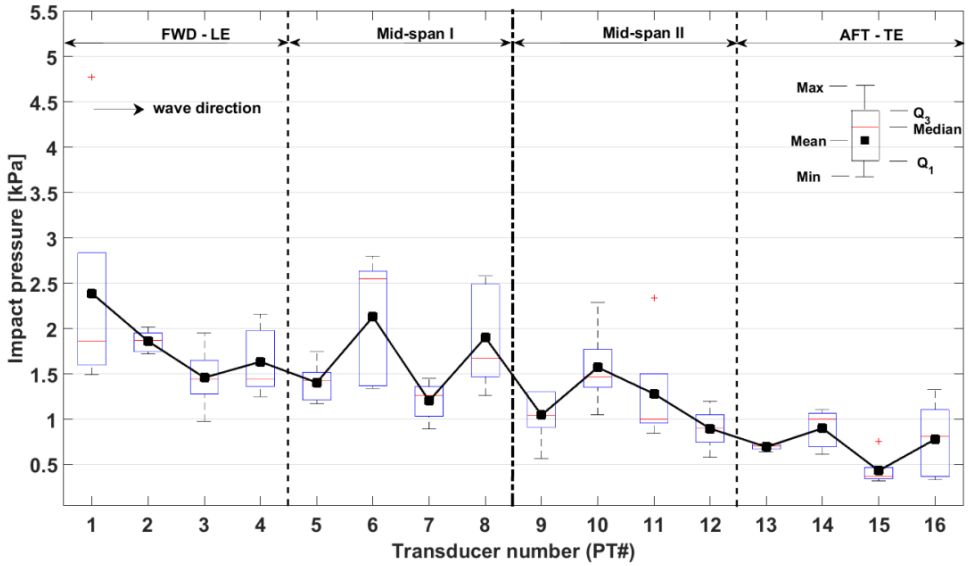

Figure 2-17: Boxplots showing impact pressures measured by sixteen PTs in multiple runs for condition 1 [WE#1: H = 251 mm, T_z = 1.37 s at a_0 = 120 mm].

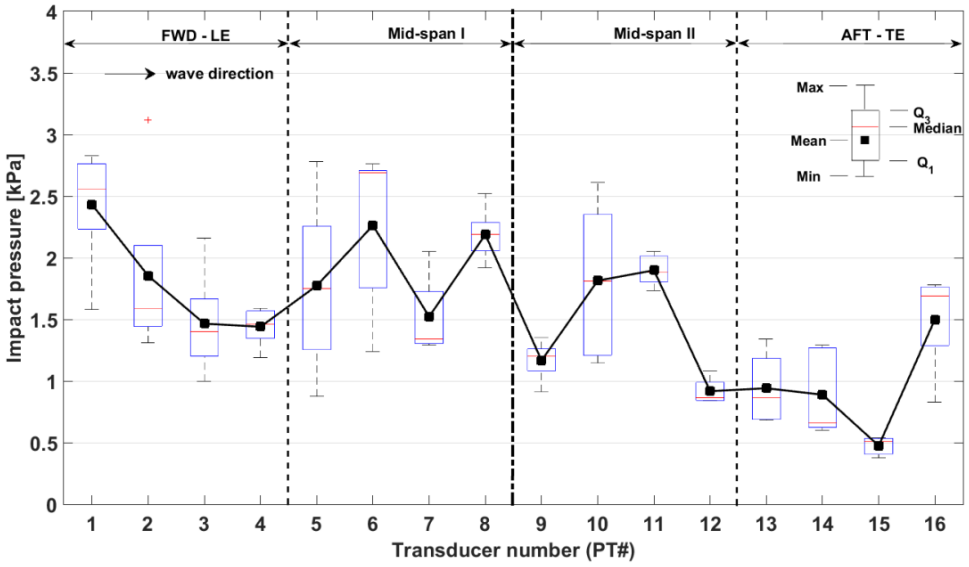

Figure 2-18: Boxplots showing impact pressures measured by sixteen PTs in multiple runs for condition 9 [WE#1: H = 251 mm, T_z = 1.37 s at a_0 = 110 mm].

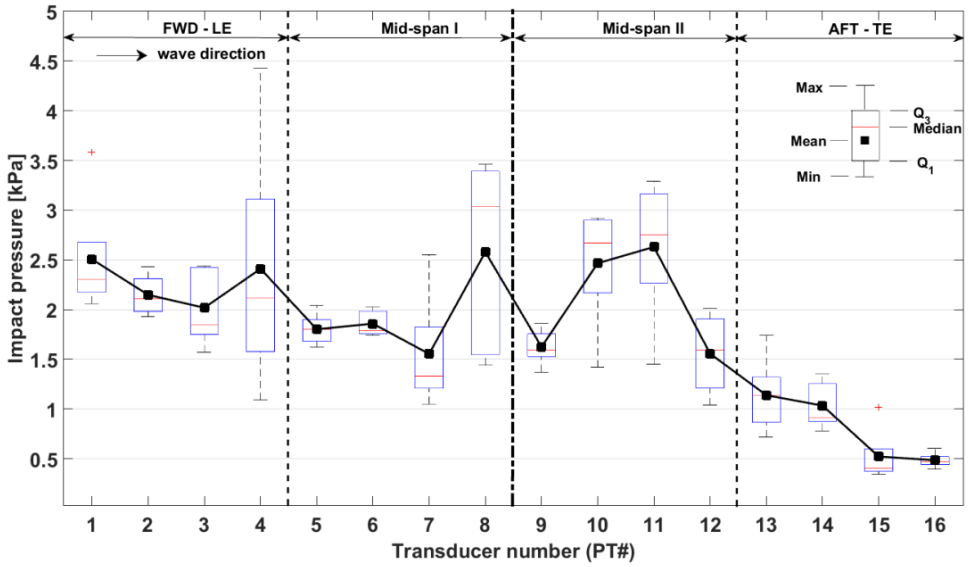

Figure 2-19: Boxplots showing impact pressures measured by sixteen PTs in multiple runs for condition 18 [WE#1: H = 251 mm, T_z = 1.37 s at a_0 = 100 mm].

2.5. Results and discussion

2.5.1. Deck clearance effect

Table 2-9 shows the change in the horizontal force (F_x) for different deck clearances due to 12 wave events. Peak forces from different runs were averaged and listed against each wave event. Wave event WE#5 (u = 0.95 m/s) produced the largest horizontal forces.

Table 2-9. A summary of the averaged peak values of the horizontal force (F_x).

WE#	u (m/s)	η_c/H (-)	Horizontal force, F_x (N)		
			a_0 = 120 mm	a_0 = 110 mm	a_0 = 100 mm
1	0.803	0.610	12.1	15.5	24.6
2	0.920	0.583	16.1	21.4	29.8
3	0.560	0.606	1.2	-	7.7
4	0.420	0.726	5.6	9.8	15.6
5	0.950	0.674	88.2	96.7	-
6	0.710	0.657	1.2	4.31	7.7
7	0.660	0.609	0.9	3.7	6.2
8	0.720	0.667	57.2	61.9	75.1
9	0.290	0.573	-	2.8	3.9
10	0.610	0.702	-	4.1	9.9
11	0.780	0.589	-	-	14.3
12	0.320	0.675	-	-	9.8

The average horizontal force peaks were normalised by $0.5\rho Au^2$, in which A is the impact area in x-direction estimated by $A = B\ (\eta_c - a_0)$. Figure 2-20 shows the normalised peak values (F^*_x) versus the parameter η_c/H at the three deck clearances tested. The ratio of 2.5 is a force coefficient recommended by the certification bodies for end – on and broadside wave directions [7, 8, 33]. In many cases, the force ratio was found to exceed the recommended value (2.5), particularly with increasing η_c/H.

In order to examine the effect of deck clearance reduction on the force magnitude in the x-direction, the averaged peak values obtained at a_0 = 110 mm and a_0 = 100 mm were divided by those measured at the original deck clearance (a_0 = 120 mm). A 10 mm reduction was found to amplify the force peaks by 28% in WE#1 and 33% in WE#2 (Table 2-10). The deck structure experienced much larger forces at a_0 = 100 mm in comparison with a_0 = 120 (20 mm reduction), for instance, the peak values in wave events WE#1 and 2 increased by factors of approximately 2.03 (103% increase) and 1.85 (85% increase).

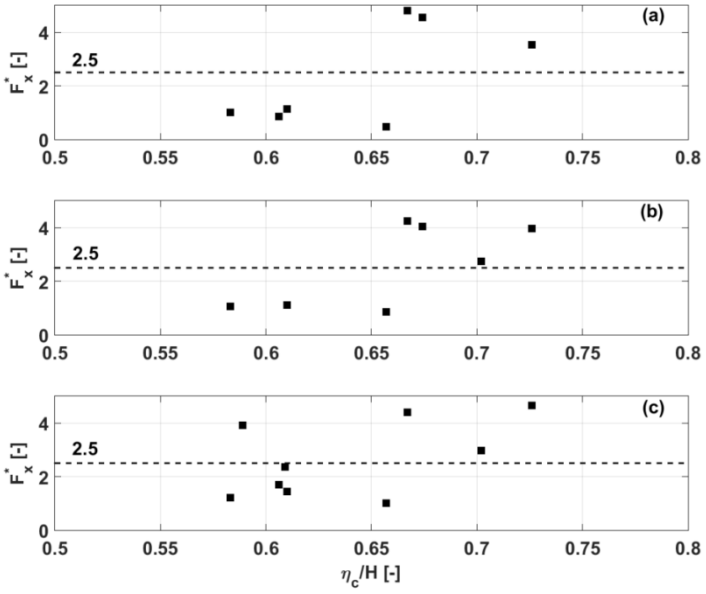

Figure 2-20: Normalised horizontal peak forces [$F^*_x = F_x / 0.5\rho A u^2$] versus wave crest to height ratio, η_c/H: (a) a_0 = 120 mm; (b) a_0 = 110 mm; (c) a_0 = 100 mm.

Table 2-10: The effect of deck clearance reduction on the averaged peak values of the horizontal force (F_x).

WE#	Ratio to F_x measured at a_0 = 120 mm	
	10 mm reduction	20 mm reduction
1	1.28	2.03
2	1.33	1.85
5	1.10	-
8	1.08	1.31

Table 2-11 shows the effect of deck clearance on the peak values of the vertical upward force component, $F_z(+)$, due to the most severe wave events observed in this investigation. $F_z(+)$ peak values were significantly amplified as a result of reducing the deck clearance. For example, a 20 mm reduction (2.5 m full scale) caused amplification ratios in $F_z(+)$ peak values to approximately 2.0 (100%) for WE#1, 1.88 (88%) for WE#2, 1.95 (95%) for WE#5 and 2.24 (124%) for WE#8. Figure 2-21 shows the time history of global wave-in-deck forces due to wave event WE#1 using a single run for test conditions 1, 9 and 18.

Table 2-11: The effect of deck clearance reduction on the averaged peak values of the upward vertical force, $F_z(+)$.

WE#	S [-]	Vertical force, F_z (+) (N)			Ratio to $F_z(+)$ measured at a_0 = 120 mm	
		a_0 = 120	a_0 = 110	a_0 = 100	10 mm reduction	20 mm reduction
1	0.086	28.6	38.6	56.8	1.35	1.99
2	0.098	31.3	42.0	58.8	1.34	1.88
5	0.103	40.5	50.0	79.0	1.23	1.95
8	0.072	30.4	52.6	68.2	1.73	2.24

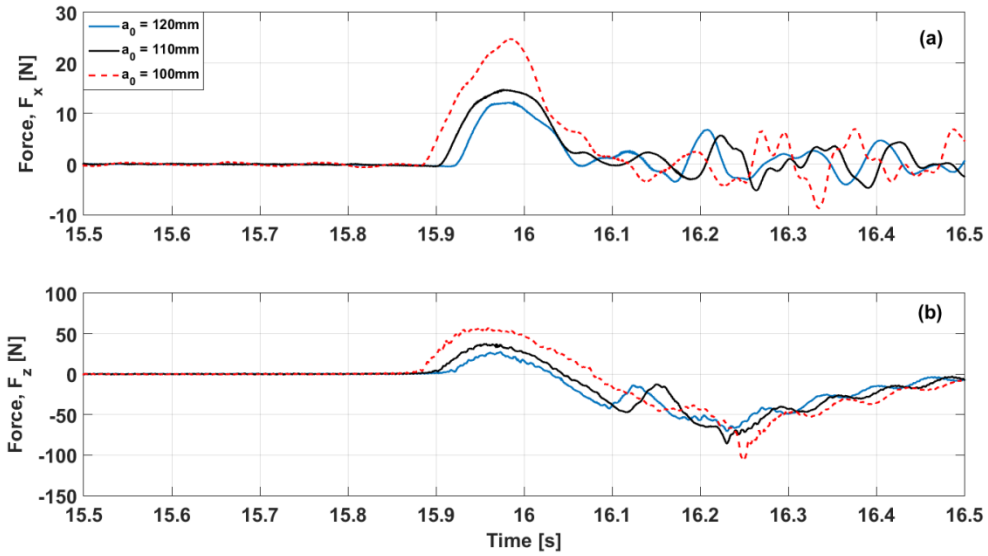

Figure 2-21: Time history of global wave-in-deck forces at different values of a_0: (a) horizontal force, F_x; (b) vertical force, F_z.

2.5.2. Deck clearance versus impact pressures

The effect deck clearance reduction on the magnitude of impact pressures associated with wave events WE#1, 2, 5 and 8 is shown in Figure 2-22 through Figure 2-25. The averaged impact pressure measured was normalised by the dynamic pressure ($0.5\rho C^2$) associated with the wave event for each pressure transducer.

The x-position of each pressure transducer measured from the model's centroid (Table 2-2) was used for x-axis where the LE and TE are denoted by vertical dashed lines at x = -304 mm and x = 304 mm, respectively. The markers represent the number of pressure transducers, PT#1 – PT#16, along the deck.

The results of pressure measurements indicated that the location of the maximum impact pressure(s) moved towards the trailing edge as the deck clearance reduced. Furthermore, the results suggested that the impact pressure at the deck edges were not clearly affected by reducing the deck clearance e.g., PT#1, 2 and PT#15 and 16.

The effect of a_0 was more noticeable for the remaining pressure transducers PT#3 – PT#14. At a_0 = 120 mm the deck structure experienced impact pressures, at most locations, below the associated dynamic pressure of the oncoming wave, whereas the impact pressures experienced by the structure exceeded the dynamic pressure as a result of reducing the deck clearance by 10 mm or 20 mm.

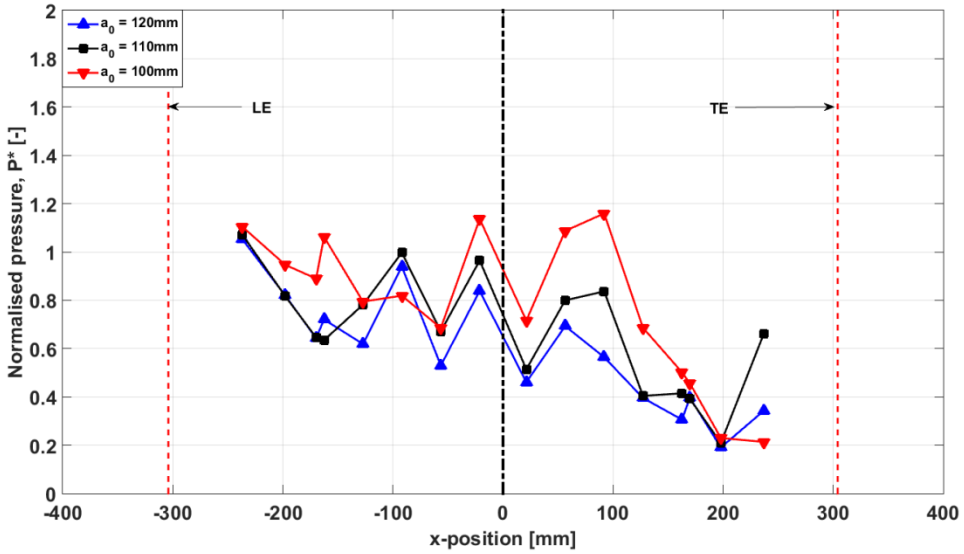

Figure 2-22: Normalised impact pressures [$P^* = P_i/0.5\rho C^2$] associated with WE#1 [H = 251 mm, T_z = 1.37 s, C = 2.13 m/s] along the bottom plate at different values of a_0.

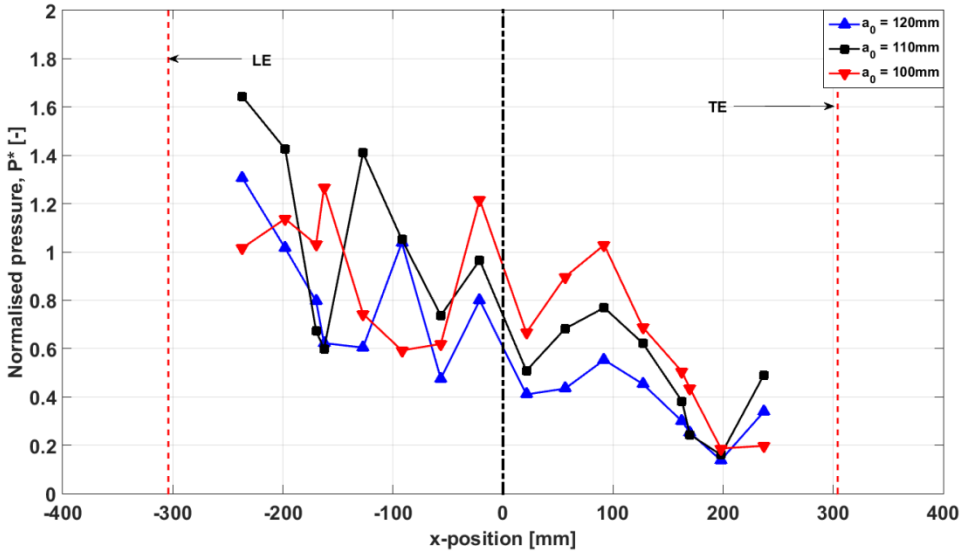

Figure 2-23: Normalised impact pressures [$P^* = P_i/0.5\rho C^2$] associated with WE#2 [H = 271 mm, T_z = 1.33 s, C = 2.08 m/s] along the bottom plate at different values of a_0.

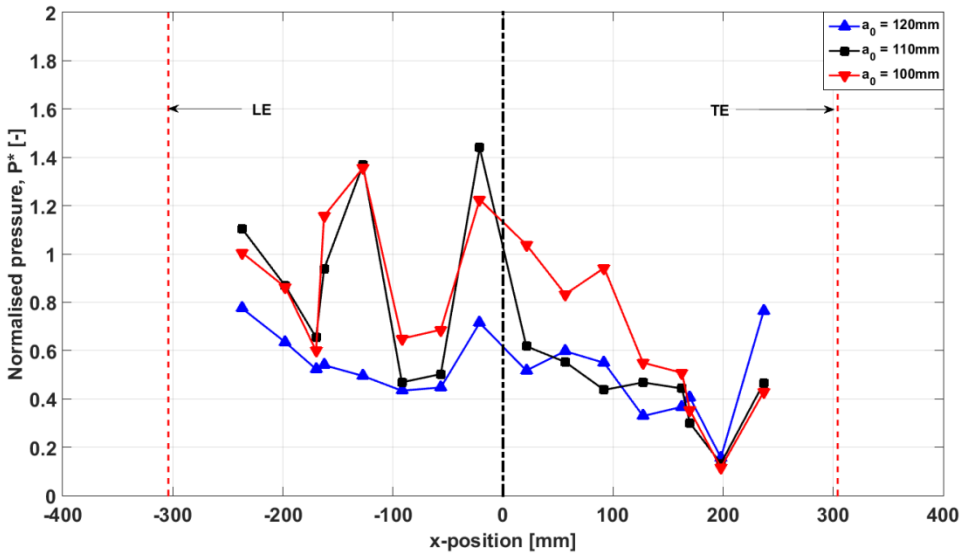

Figure 2-24: Normalised impact pressures [$P^* = P_i/0.5\rho C^2$] associated with WE#5 [H = 242 mm, T_z = 1.23 s, C = 1.92 m/s] along the bottom plate at different values of a_0.

For WE#8 (Figure 2-25) when a_0 = 120 mm, the forward section of the bottom plate was found to experience large pressures captured by PT#1, 4, 5 and 8. Likewise, at a_0 = 110 mm, larger pressures experienced by the bottom plate at PT#2, 5 and 8. By reducing the deck clearance to 100 mm, much larger pressures can be seen at PT#5, 6 and 8. This also implied that the location of larger pressures moves towards the TE as the deck clearance reduced. A total reduction of 20 mm in the deck clearance resulted in twice as much pressure (e.g., PT#5 and 8) as those experienced by the deck structure at a_0 = 120 mm.

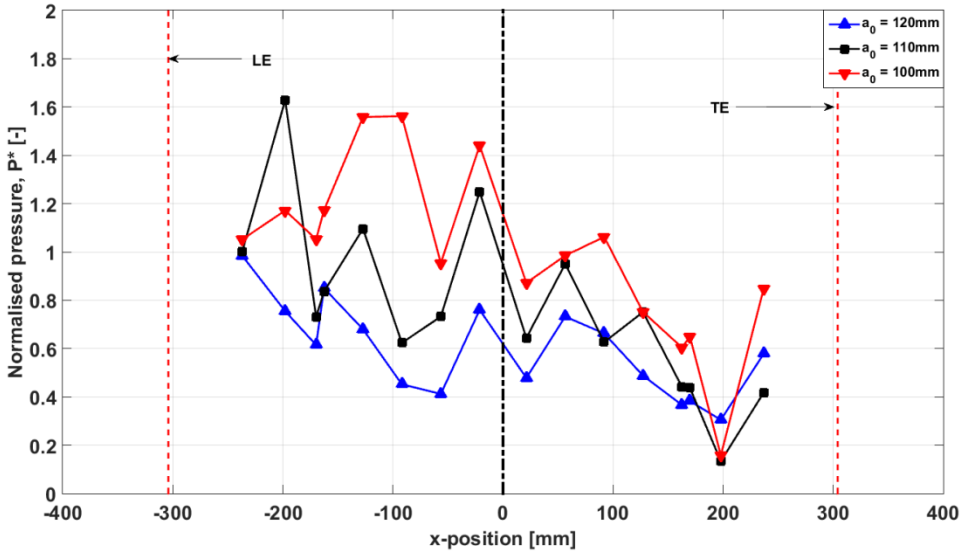

Figure 2-25: Normalised impact pressures [$P^* = P_i/0.5\rho C^2$] associated with WE#8 [H = 249 mm, T_z = 1.49 s, C = 2.31 m/s] along the bottom plate at different values of a_0.

2.5.3. Occurrence time of impact pressures

For condition 1, the occurrence time of wave slamming at the location of each pressure transducer was estimated using the measured pressure signals and the wave elevations. Figure 2-26 (a) shows the time history of WP4 (LE) and WP5 (TE) in Run 1. The start time and the end time of WE#1 at a_0 = 120 mm are denoted by t_o and t_f, respectively, where t_o is to define the initial time in which the wave crest comes into contact with the bottom plate at the LE. The markers in Figure 2-26 (b) represent the number of pressure transducers along the deck. The maximum peak pressure (at PT#8) was found to occur at approximately 130 ms (9.5% T_z) from t_o which was almost equal x/C, where x is the distance from the LE to the centre of PT#8. This indicates that the change of wetted length along the deck may be approximated by the wave phase velocity and/or extracted from pressure data. On average, a time difference of 20 ms was obtained between two following pressure transducers.

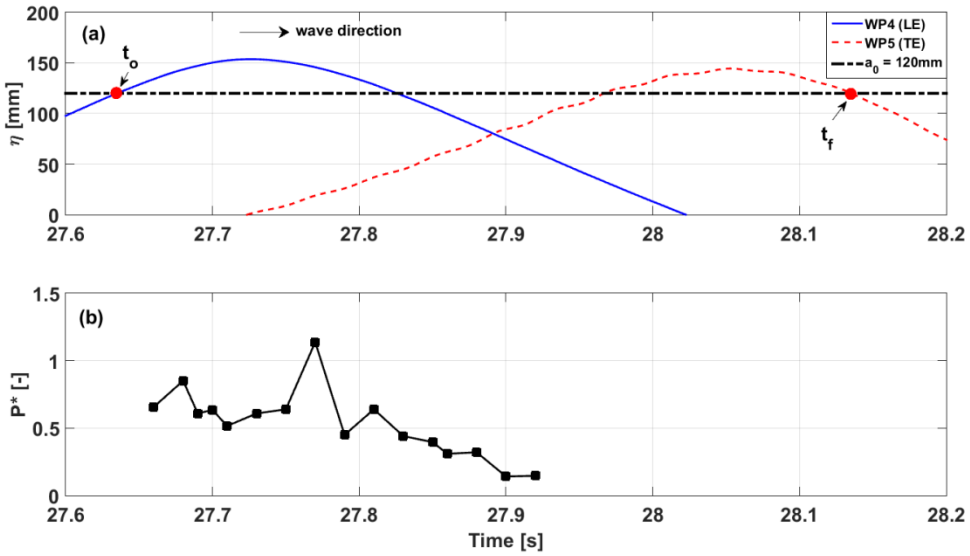

Figure 2-26: A typical time tracking of impact pressures along and across the bottom plate for condition 1 [WE#1: H = 251 mm, T_z = 1.37 s, C = 2.13 m/s at a_0 = 120 mm]: (a) wave elevations measured by WP4 (LE) and WP5 (TE); (b) normalised impact pressures [$P^* = P_i/0.5\rho C^2$], markers (▪) denote the sequence of PT#.

2.6. Summary

This chapter described a series of model tests conducted to examine extreme wave events associated with tropical cyclonic conditions and their impacts on a rigidly mounted box-shaped deck, which represents a simplified topside structure of a tension leg platform (TLP) offshore deck structure. Experimental results presented included global forces and localised slamming pressures acting. The effect of static set-down on the still-water air gap was

investigated by applying an equivalent reduction in the deck clearance. The following conclusions can be drawn:

- In the present investigation, the structural dynamic response was found to have a minimal effect on the peak values of the horizontal force, F_x, and the upward vertical force, $F_z(+)$, and its influence only being noticeable in the water exit phase. This finding should be considered conclusive provided that there are not successive large waves impacting the structure; in which case, the structural and viscous damping appear to strongly influence the force signals, particularly in the direction of wave propagation.
- In many wave events (e.g., WE#1, 2, 5 and 8) the effect of deck clearance reduction on all force components was pronounced. It was found that a 20 mm reduction (2.5 m full scale, ≈17% of the original deck clearance) in the original deck clearance can lead to a doubling of the magnitude of the horizontal force, F_x, and the vertical upward-directed force, $F_z(+)$, components. This large increase in force magnitudes highlighted the threat of wave deck impact due to air gap reduction.
- Most of the test conditions demonstrated that the magnitude of the impact pressure varied considerably among repeated runs, even if identical wave condition was used. In order to reduce the variance on the pressure measurement results, more than five runs per test condition are necessary during tank experiments.
- By investigating the effect of deck clearance on the localised impact pressures, the reduction in the original deck clearance (10 mm or 20 mm) increased the impact pressure magnitude at many locations along and across the deck underside. However, pressure measurements revealed that the impact pressure may not necessarily increase for all pressure transducers with decreasing deck clearance.
- In most test conditions, the front half of the bottom plate (PT#1 – PT#8) experienced larger pressures than the rear section. The results suggested that the location of the maximum impact pressure(s) moves towards the trailing edge (TE) as the deck clearance reduced. Looking at an area rather than a discrete point will be more useful in assessing the severity of the deck

clearance reduction on the local effect of wave-in-deck loading on a fixed platform deck.

- The results of the present investigation provided statistically reliable force (global) and pressure (local) values for a more accurate computational fluid dynamics (CFD) model validation of wave-in-deck impact problems.

Chapter 3: Experimental investigation of extreme wave impacts on a rigid TLP model in cyclonic conditions

The work presented in this chapter has been accepted for publication in the *Journal of Ships and Offshore Structures*. The paper has been edited for inclusion into this thesis to avoid repetition and to improve readability. The citation for this research article is:

Nagi Abdussamie, Roberto Ojeda, Yuriy Drobyshevski, Giles Thomas and Walid Amin (2016). "Experimental investigation of extreme wave impacts on a rigid TLP model in cyclonic conditions", *Ships and Offshore Structures*. 2016: 1-18.

3.1. Scope

The objectives of this experimental investigation are to study the wave forces and wave-in-deck impact pressures on a 1:125 scale TLP model fixed in space in order to obtain good quality wave force and local pressure data. The model was subjected to extreme wave events corresponding to long-crested irregular wave trains of a sea state, representative of the 10,000-year cyclonic sea state offshore Western Australia at different deck clearances.

3.2. Model tests

3.2.1. Model design and construction

The TLP was represented by a box-type deck structure supported by four circular columns; the scaled model dimensions were based on the SNORRE-A tension leg platform. The main particulars of the structure are given in Table 3-1 and Figure 3-1. It can be noted in this table that the 1:125 water depth does not represent the actual operational water depth of SNORRE-A. This was due to the limitations imposed by the maximum operational water depth of the towing tank of 1.5 m.

Table 3-1: Key particulars for the SNORRE-A TLP at full and model scales.

Parameter	Full scale	Tested model scale
Column diameter, D	25.00 m	200 mm
Pontoon height, h	11.50 m	92 mm
Pontoon width, w	11.50 m	92 mm
Platform's draft, d	38.125 m	305 mm
Column spacing, s	76.00 m	608 mm
Column height	63.00 m	505 mm
Deck size, $L \times B \times h_d$	124.50 × 92.00 × 15.00 m	608 × 608 × 210 mm
Water depth	310.00 m	1500 mm
Deck clearance, a_0	27.00 m	120 mm

The hull columns of the TLP model were made of fibreglass tubes internally reinforced by plywood ring frames for added rigidity. The pontoons were made of plywood also reinforced internally by plywood frames. The pontoons and the columns were connected using epoxy glue and reinforcing fibreglass tapes. Column tops were tightly closed using acrylic covers sealed using plasticine.

The 608 mm × 608 mm square deck box was constructed using a 10 mm thick aluminium plate for the deck bottom and 100 mm × 25 mm × 2.5 mm rectangular hollow

section (RHS) aluminium extrusions for the deck sides. A 100 mm tall acrylic wall was mounted on top of the aluminium sides, as shown in Figure 3-2.

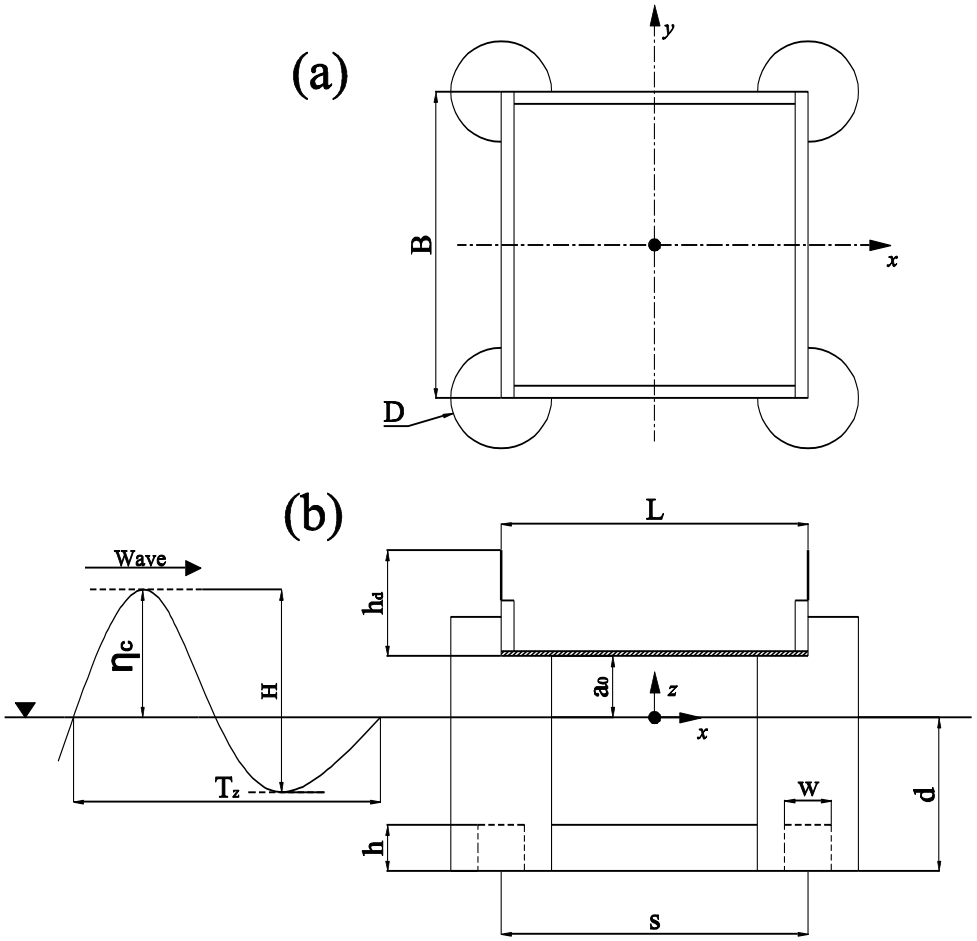

Figure 3-1: A definition sketch of the tested model and incoming wave: (a) plan view at the deck level; (b) side view [not to scale].

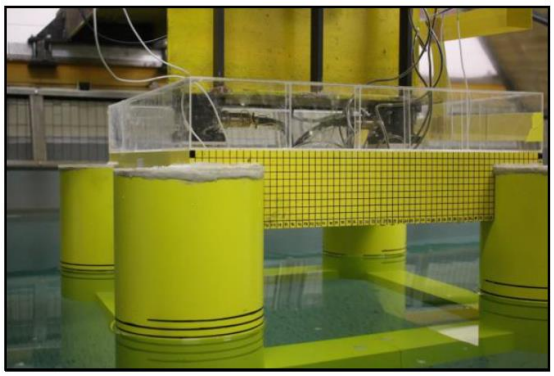

Figure 3-2: A close view showing the deck supported by columns and square pontoons (looking at the starboard side of the model i.e. column#1 and 3; waves propagating from right to left).

3.2.2. Model instrumentation

As already mentioned in Chapter 2, the selection of load cells and pressure transducers was made based on a preliminary CFD study. The combined deck and hull model was subjected to an extreme regular wave condition (H = 240 mm and T = 1.52 s) at a_0 = 100 mm. CFD results showed that the area around the forward and aft columns can experience large slam pressure during wave-in-deck impact events. The deck-column intersection areas, therefore, were instrumented by a set of pressure transducers.

Two load cells were used to measure the global hydrodynamic force generated due to the impact of the wave crest against the model. The layout of the two AMTI MC3A-100 load cells, denoted by LC1 and LC2, is illustrated in Figure 3-3. Each load cell has a square base of 76 mm × 76 mm which was connected to the deck of the box model using a hinge for LC1 and a slider mounted hinge LC2, respectively. The vertical force, Fz, was measured by both load cells, whilst the horizontal force, Fx, was measured by the forward load cell LC1 only. An MTi-30 Xsens accelerometer was installed in the middle of the deck underside.

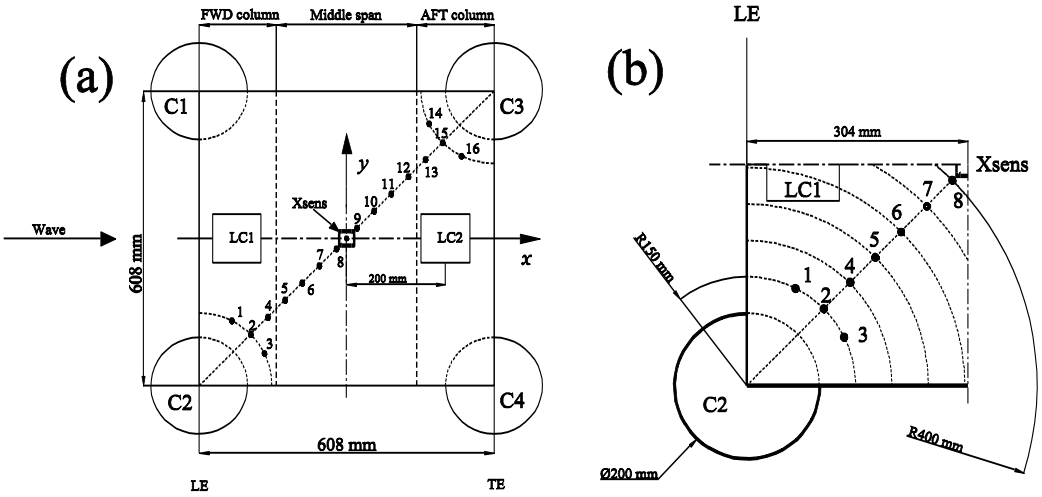

Figure 3-3: Plan view of instrumentation layout: (a) distribution of pressure transducers and load cells (LC) on the deck underside; (b) details of PT#1 – PT#8 around the forward column [not to scale].

As listed in Table 3-2, the localised slamming pressures were measured using sixteen piezoresistive pressure transducers, PT, (seven Endevco 8510C-50, two Endevco 8510B-2 and seven Measurex MRV21-0.5). As shown in Figure 3-3, the pressure transducers were distributed over three regions namely forward (FWD), middle span (Mid-span) and aft (AFT) regions. The area around the forward column (denoted by C2) was instrumented by PT#1 –

PT#4, whilst PT#13 – PT#16 were located to measure wave impact pressures near the aft column (denoted by C3).

Figure 3-3 (b) details the first 8 pressure transducers located in the forward section of the bottom plate, shown using a radial distribution. As seen in Table 3-2 the spatial location for each transducer is given by using the Cartesian coordinate system where *x*- and *y*-coordinate is measured from the model's centroid to the tip centre of each transducer (approximately 4.0 mm in diameter).

Table 3-2: Specifications and Cartesian coordinates of pressure transducers (PT).

PT#	Model	Sensitivity (mV/kPa)	Range (kPa)	Location (*x*, *y*) (mm)
1	8510B-2	16.650	0 – 13.8	(-236.9, -169.8)
2	8510B-2	19.095	0 – 13.8	(-197.9, -197.9)
3	MRV21-0.5	1.038	0 – 50.0	(-169.8, -236.9)
4	MRV21-0.5	1.042	0 – 50.0	(-162.6, -162.6)
5	8510C-50	0.722	0 – 344.0	(-127.2, -127.2)
6	8510C-50	0.638	0 – 344.0	(-91.9, -91.9)
7	MRV21-0.5	1.051	0 – 50.0	(-56.5, -56.5)
8	8510C-50	0.572	0 – 344.0	(-21.2, -21.2)
9	8510C-50	0.652	0 – 344.0	(21.2, 21.2)
10	MRV21-0.5	1.035	0 – 50.0	(56.5, 56.5)
11	8510C-50	0.701	0 – 344.0	(91.9, 91.9)
12	MRV21-0.5	1.110	0 – 50.0	(127.2, 127.2)
13	MRV21-0.5	1.021	0 – 50.0	(162.6, 162.6)
14	MRV21-0.5	1.091	0 – 50.0	(169.8, 236.9)
15	8510C-50	0.731	0 – 344.0	(197.9, 197.9)
16	8510C-50	0.724	0 – 344.0	(236.9, 169.8)

3.2.3. Measurement of wave elevation

The location of five wave probes (denoted as WP) used during model tests is presented in Table 3-3. The position was defined with respect to an origin point located at the model's centroid, with positive *z-axis* pointing upward. The model tests were conducted in the AMC towing tank illustrated in Figure 3-4.

Table 3-3: Location of wave probes used in the model tests with respect to the model's centroid.

Wave probe (WP)	Location (*x*, *y*) (m)
1	(-10.000, 1.275)
2	(-5.000, 1.275)
3	(-1.000, 0.000)
4	(-0.404, 1.200)
5	(0.000, 1.200)

3.2.4. Wave calibration

The Joint North Sea Wave Project (JONSWAP) spectrum was utilised for a representative 10,000-year sea state associated with Australian cyclonic condition: H_s = 22.13 m, T_p = 17.0 s ($T_p/\sqrt{H_s}$ = 3.61). The resulting scaled parameters at 1:125 were H_s = 177 mm, T_p = 1.52 s. A value of 1.0 for the peak shape parameter, γ, was selected. The wavemaker produced a sequence of wave realisations to synthesise short-time long-crested irregular wave trains. The wave realisations of interest were selected based upon an iterative wave calibration process. Using a single wave realisation, the wavemaker was run for approximately 120 s without the model in place (wave probes sampled at 200 Hz during wave calibration).

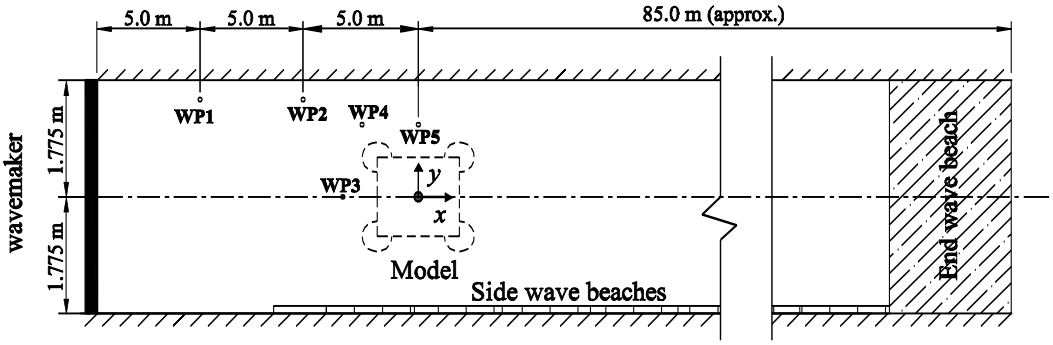

Figure 3-4: Plan view of the AMC towing tank showing the distribution of wave probes (WP) during wave calibration (the same arrangement was used during wave impact tests with the TLP model in-place) [not to scale].

3.3. Model installation and free oscillation tests

3.3.1. Model attachment

The stiffness and rigidity of the system were ensured by attaching the model to a 4500 mm long heavy steel H-beam (334 mm × 170 mm × 6/11 mm) placed across the tank 15.0 m away from the wavemaker as shown in Figure 3-5. The model was then supported by the load cells LC1 and LC2 connected to a 510 mm long I-beam (360 mm × 170 mm × 6/10 mm) suspended from the H-beam.

3.3.2. Tested deck clearances

Table 3-4 shows the three deck clearances tested and the corresponding platform's draft and the related buoyancy force, given at both full and model scales. A 10 mm reduction in deck clearance, which is equivalent to 1.25 m at full scale, could realistically occur due to platform settlement or set-down and/or sea level rise [54].

Table 3-4: Variation of platform's draft and deck clearance tested.

Full scale			Tested model scale		
Draft, d (m)	Deck clearance, a_0 (m)	Buoyancy force, F_B (N)	Draft, d (mm)	Deck clearance, a_0 (mm)	Buoyancy force, F_B (N)
38.125	15.00	10.00×10^8	305	120	511.50
39.375	13.75	10.23×10^8	315	110	523.83
40.625	12.50	10.47×10^8	325	100	536.16

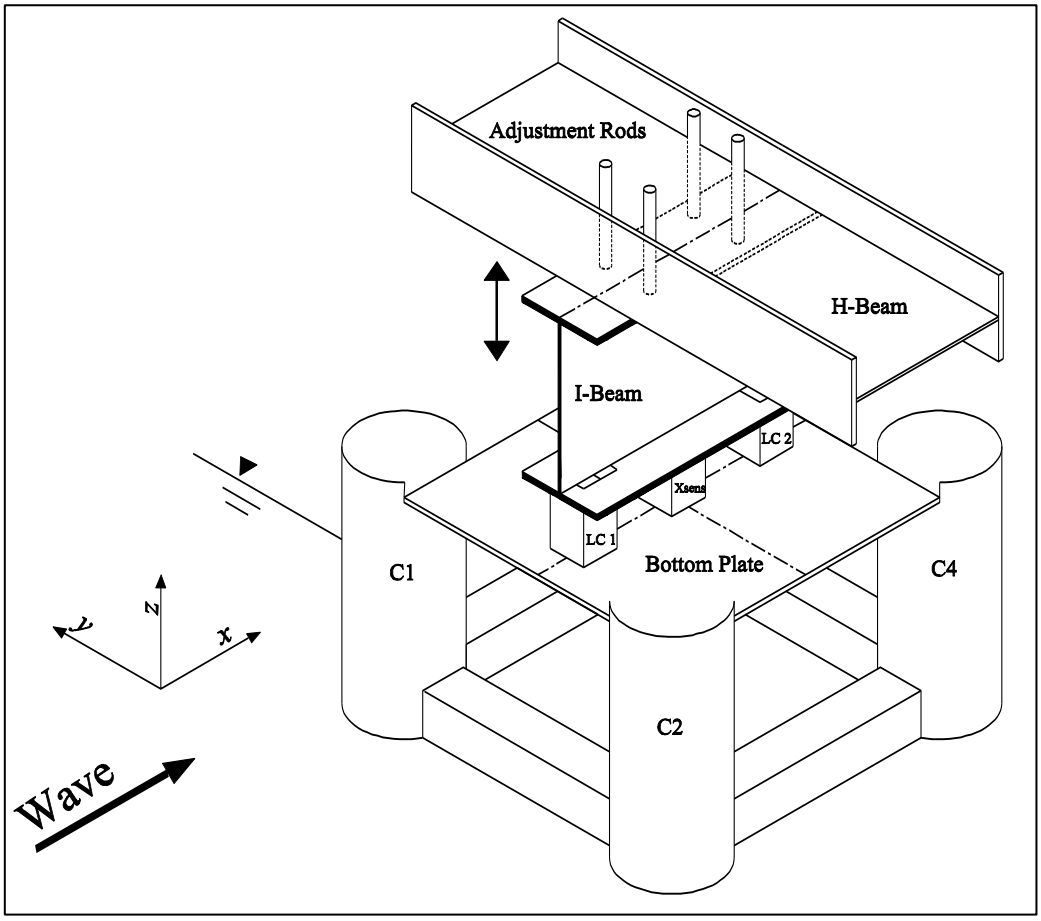

Figure 3-5: Isometric view of model attachments and the adjustment of deck clearance. The I-beam and the TLP model can be moved up and down; the increase in draft equivalently indicated the required reduction in the still-water air gap (deck clearance).

3.3.3. Free oscillation tests

The natural frequency of the testing assembly (TLP model, instruments and force supports) was obtained from the load cells and accelerometer time traces. Table 3-5 shows the results of the tests conducted with the bottom of the TLP pontoons located in air (test 1) and just above the water surface (test 2).

Table 3-5: The lowest frequency, f_n, observed during free oscillation tests.

Test	Description	f_n in x-direction (Hz)	f_n in z-direction (Hz)
1	Decay test in air	8.00	18.00
2	Decay test in water	7.33	15.00

3.4. Wave impact tests

A sampling frequency of 20 kHz was chosen for all channels in order to capture the short-duration slamming pressures. As can be seen in Table 3-6, each wave realisation (denoted as R1, R2 and R10) has two extreme wave events. The wave parameters were derived from the time history of WP4 with the model in place using the zero up-crossing method (see Figure 3-1).

Table 3-6: Wave parameters of wave events extracted from WP4 while the model being in the tank.

Realisation	Wave event (WE)	H (mm)	η_c (mm)	T_z (s)	λ (m)	C (m/s)	S (-)
R1	1	244	143	1.40	3.05	2.18	0.08
R1	2	261	154	1.38	2.96	2.15	0.09
R2	3	186	136	1.77	4.72	2.66	0.04
R2	4	238	153	1.25	2.44	1.95	0.10
R10	5	174	103	1.38	2.96	2.15	0.06
R10	6	237	151	1.48	3.39	2.29	0.07

Table 3-7 summarises the estimated wave event parameters scaled using the input significant wave height (H_s = 177 mm) and the peak wave period (T_p = 1.52 s). All test conditions showed a negative air gap ($a = a_0 - \eta_c$) but for conditions 5 and 11 (WE#5: H = 174 mm, T_z = 1.38s, η_c = 103 mm). Due to wave upwelling, there was an evidence for deck impact at its underside for both conditions using WP5 time histories.

3.5. Data and uncertainty analysis

3.5.1. Wave elevations

In order to obtain high-quality experimental data and ensure repeatability and accuracy in the measurements of both global and local wave impact loads, each test condition was repeated up to five times. Figure 3-6 depicts the wave train of realisation R1 measured by WP4 using data from five runs with the model being in the tank at a_0 = 120 mm (the time vectors being manually synchronised). Excellent repeatability can be seen for the five results over the measured time history of 15.0 s.

Table 3-7: Model test conditions.

Condition	Deck clearance, a_0 (mm)	Wave event (WE)	Wave height ratio, H/H_s (-)	Wave skewness, η_c/H (-)	Wave period ratio, T_z/T_p (-)	Air gap, a (mm)
1	120	1	1.38	0.59	0.92	-23
2	120	2	1.47	0.59	0.91	-34
3	120	3	1.05	0.73	1.16	-16
4	120	4	1.34	0.64	0.82	-33
5	120	5	0.98	0.59	0.91	17
6	120	6	1.34	0.64	0.97	-31
7	110	1	1.38	0.59	0.92	-33
8	110	2	1.47	0.59	0.91	-44
9	110	3	1.05	0.73	1.16	-26
10	110	4	1.34	0.64	0.82	-43
11	110	5	0.98	0.59	0.91	7
12	110	6	1.34	0.64	0.97	-41
13	100	1	1.38	0.59	0.92	-43
14	100	2	1.47	0.59	0.91	-54
15	100	3	1.05	0.73	1.16	-36
16	100	4	1.34	0.64	0.82	-53
17	100	5	0.98	0.59	0.91	-3
18	100	6	1.34	0.64	0.97	-51

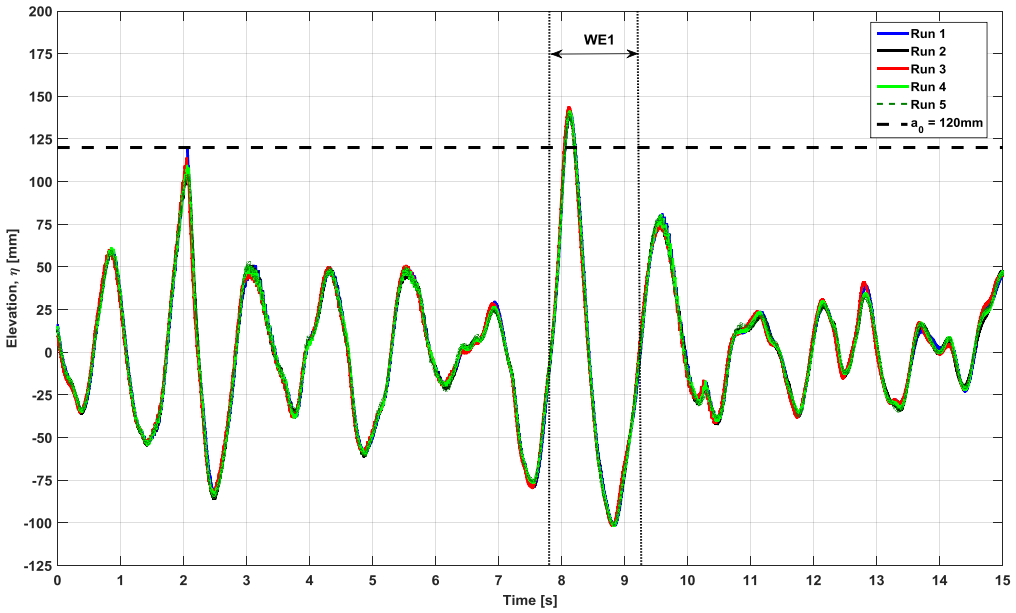

Figure 3-6: A short-time wave train measured by WP4 with the model being in the tank at a_0 = 120 mm using five runs (WE#1 is shown at 7.0 s – 9.0 s).

3.5.2. Force signals

The associated wave impact forces in *x*- and *z*-direction are illustrated in Figure 3-7 (a) and (b), respectively. The time history of both WP4 (Figure 3-6) and F_x (Figure 3-7 (a)) were found to be in-phase and have similar trends. For instance, the crest of each wave and the associated peak force are approximately synchronised.

As summarised in Table 3-8, the generated wave event WE#1 was found to be repeatable at WP4 and WP5 with a mean wave height of 243 mm at WP4 and 256 mm at WP5. It was found that wave troughs (-) measured by WP4 and WP5 are almost identical. However, there was approximately an 8% increase in crest height (+) at WP5 indicating the diffraction effect on the upper region of wave profile. Fx was also found to be repeatable in the positive and negative directions. This was not the case for the Fz component, which was found to have a higher variability in the upward and downward directions; as demonstrated by the larger standard deviation.

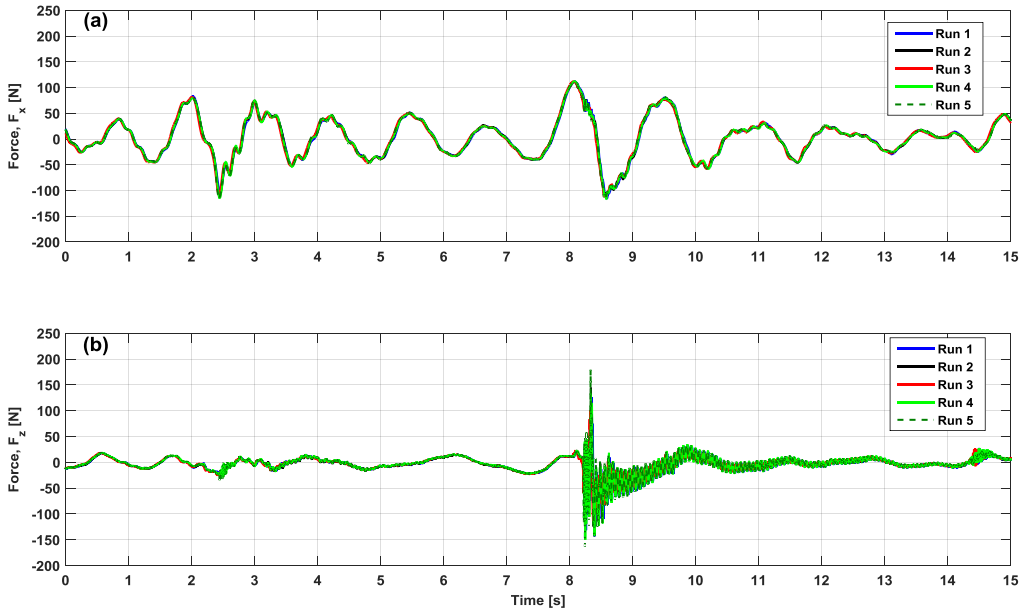

Figure 3-7: Repeatability test of impact force for condition 1: (a) horizontal force, F_x; (b) vertical force, F_z.

3.5.3. Force signal variation analysis

By recalling Figure 3-6 and Figure 3-7 using the data of Run 1, Fast Fourier Transform (FFT) results of F_x and F_z are plotted along with the WP4 frequency components in Figure 3-8 (a) and (b), respectively. In the subplot (a) F_x was found to have frequency components

coinciding within the WP4 FFT results. Apart from wave frequency bandwidth, higher frequencies with a low FFT magnitude can be seen at approximately 6.0 Hz (≈ f_n = 7.33 Hz).

For F_z component shown in Figure 3-8 (b), a frequency of 15.10 Hz was observed (≈ f_n = 15.00 Hz). Another high-frequency component can be seen at 61.1 Hz, which is considered to be due to the coupling effect between *x*- and *z*- vibration modes. The effect of such high frequencies could be attenuated using a low-pass filter with a carefully selected cut-off frequency.

Table 3-8: Simultaneous measurements of wave probes and load cells for condition 1 [WE#1: H = 244 mm, T_z = 1.40 s at a_0 = 120 mm]. Peaks are denoted by (+) and valleys are denoted by (-).

Run id	Wave elevation (mm)				Force (N)			
	WP4 (+)	WP4 (-)	WP5 (+)	WP5 (-)	F_x (+)	F_x (-)	F_z (+)	F_z (-)
1	141	-102	156	-103	112	-116	126	-143
2	140	-102	151	-104	112	-112	145	-125
3	144	-102	152	-102	113	-113	101	-114
4	142	-102	152	-103	112	-117	133	-150
5	140	-102	154	-102	111	-114	179	-163
Mean	141.4	-102	153	-102.8	112	-114	137	-139
σ	1.67	0.00	2.00	0.84	0.71	2.07	28.55	19.58

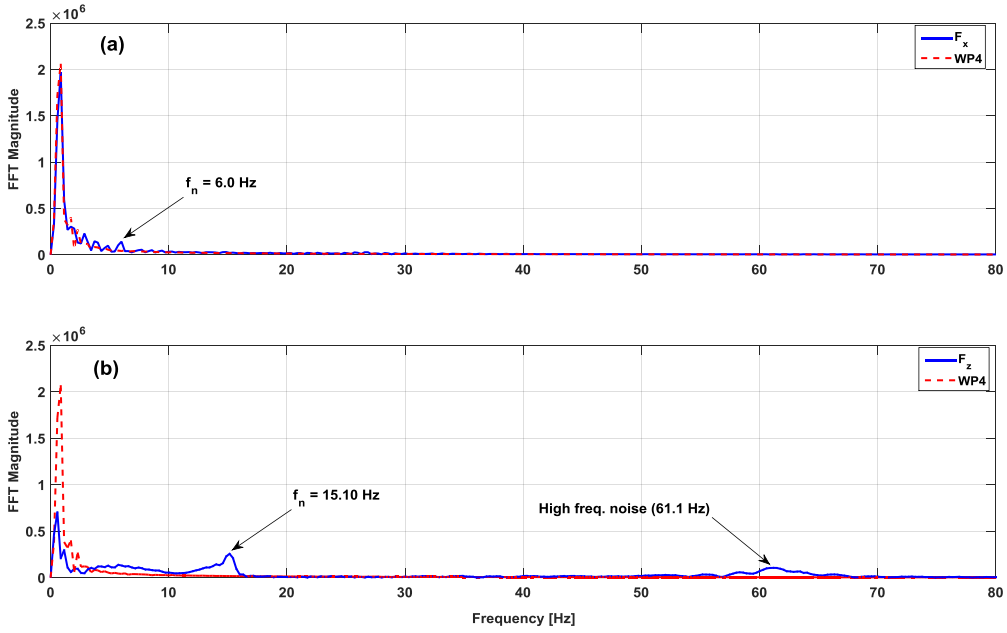

Figure 3-8: FFT results of WP4 and force components based on time histories collected in Run 1 for condition 1: (a) horizontal force, F_x, and WP4; (b) vertical force, F_z, and WP4.

Prior to filtering the observed noise in the force signals, the acceleration time histories corresponding to each wave impact event were analysed. For condition 1, the time history of *x*- and *z*-acceleration components measured in Run 1 are shown in Figure 3-9 and Figure 3-10, respectively. At WE#1 impact, the model's response in *x*- and *z*-direction was in-phase revealing that the model reacted instantaneously in at least two degrees of freedom.

Although large peaks are seen in the a_x time history, they were found to appear after the associated slam event. This suggests that the damping effect (structural and viscous) was high enough to rapidly decay the model's response in the horizontal direction. Therefore, the structural dynamic response had a minimal effect on the maximum measured horizontal forces and can be neglected.

Figure 3-10 shows that the time history of F_z prior to the slam event of WE#1 was almost unaffected by the model's dynamic response. On the other hand, during and subsequent to WE#1 the time history of F_z was largely corrupted. This could also be inferred from the long settling time shown in a_z (time = 8.0 s – 13.0 s).

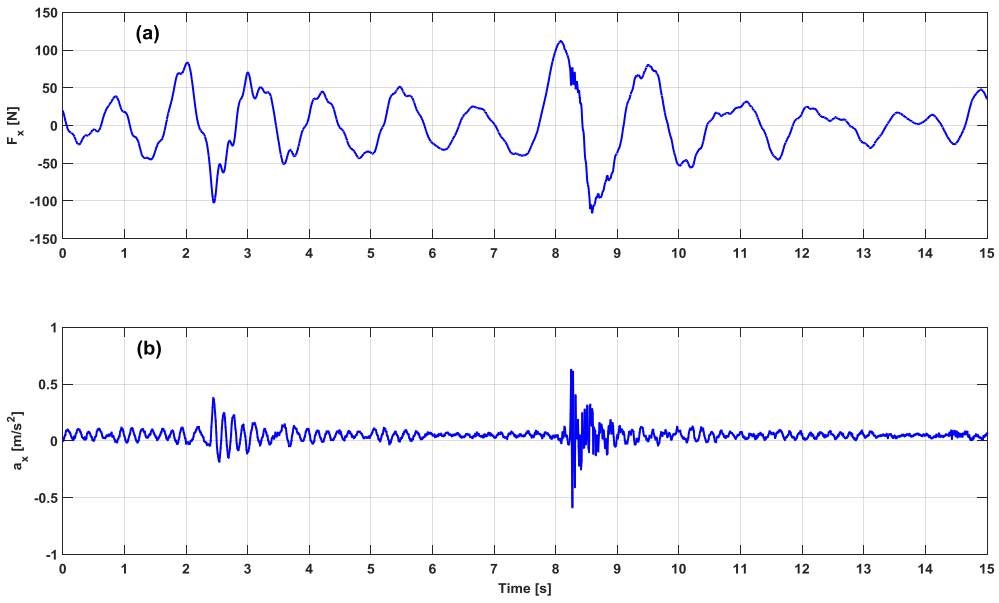

Figure 3-9: Time history of force and acceleration associated with Run 1 for condition 1: (a) horizontal force, F_x; (b) horizontal acceleration, a_x (the associated F_x and a_x with WE#1 are shown at time = 8.0 s – 9.0 s).

3.5.4. Correction of vertical forces

In order to remove the effect of the structural dynamic response, the F_z signal was furthered processed through using a fourth-order Butterworth low-pass filter. Two filters were tested using different values for cut-off frequency of 50.0 Hz (f_{c1}) and 10.0 Hz (f_{c2}). Figure 3-11

shows the time history of wave event WE#1 using both raw and filtered data. The effect of the low-pass filters on the force magnitude can be seen within the measured time history (from time = 8.2 s). The peak value of F_z(+) was reduced by approximately 28% and 65% using f_{c1} and f_{c2}, respectively. The valley value of F_z(-) was reduced by approximately 8% and 39% using f_{c1} and f_{c2}, respectively.

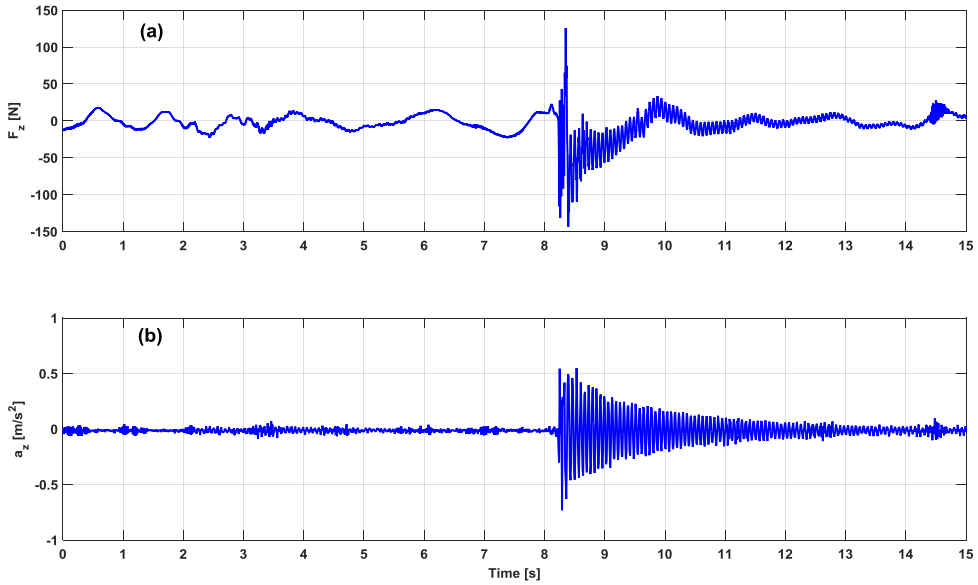

Figure 3-10: Time history of force and acceleration associated with Run 1 for condition 1: (a) vertical force, F_z; (b) vertical acceleration, a_z (the associated F_z and a_z with WE#1 are shown at time = 8.0 s – 9.0 s).

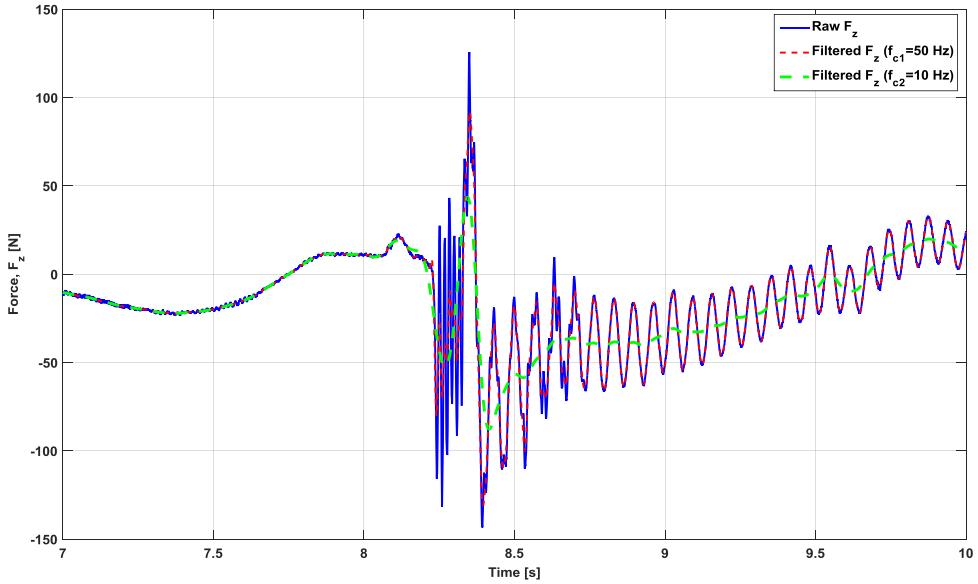

Figure 3-11: The effect of low-pass filtering (type = Butterworth, order = 4.0, f_{c1} = 50.0 Hz, f_{c2} = 10.0 Hz) on the magnitude and duration of the vertical force, F_z, in Run 1 for condition 1 [WE#1: H = 244 mm, T_z = 1.40 s at a_0 = 120 mm].

Since the higher frequency dynamic response of the model is a highly variable phenomenon, it provides a major contribution to the variability of the measured forces. Thus, it is recommended that prior to filtering a noisy force signal the associated time domain and frequency domain should be combined for additional analyses. This implies that signal processing and filtering should be conducted on a case-by-case basis. On the basis of acceleration measurements and FFT results, a cut-off frequency of 50.0 Hz was applied only for the vertical force signals contained a significant noise (observed in force and acceleration time histories) otherwise the raw measured force data was used.

The resulting peaks (+) and valleys (-) of the acceleration components along with the raw and corrected vertical forces for WE#1 in the five runs are presented in Table 3-9. It is evident that a_x and a_z were strongly correlated and affected the magnitude of F_z, for instance, the largest peak values in $a_x(+)$, $a_z(+)$ and $F_z(+)$ occurred in the same run (Run 5).

Table 3-9: Peak values of the raw and corrected (at f_{c1} = 50.0 Hz) vertical forces and model's accelerations for condition 1 [WE#1: H = 244 mm, T_z = 1.40 s at a_0 = 120 mm]. Peaks are denoted by (+) and valleys are denoted by (-).

Run id	Acceleration (m/s^2)				Raw force (N)		Corrected force (N)	
	$a_x(+)$	$a_x(-)$	$a_z(+)$	$a_z(-)$	$F_z(+)$	$F_z(-)$	$F_z(+)$	$F_z(-)$
1	0.62	-0.59	0.57	-0.71	126	-143	92.3	-131
2	0.53	-0.45	0.5	-0.66	145	-125	98.2	-110.3
3	0.36	-0.24	0.46	-0.47	101	-114	81	-106.7
4	0.54	-0.56	0.65	-0.81	133	-150	88.3	-124.6
5	0.83	-0.41	0.76	-0.71	179	-163	96.2	-117.8
Mean	0.58	-0.50	0.59	-0.67	137	-139	91	-118
σ	0.17	0.14	0.12	0.13	28.55	19.58	6.85	9.99

3.5.5. Pressure measurements

From the impact pressures measured in five repeated runs for condition 1, it is evident that the area around the aft columns experienced larger pressures than the area around the forward columns. The averaged slamming pressures at the deck-column intersections indicated that PT#2 (1.81 kPa) and PT#14/PT#15 (5.30/5.25 kPa) measured the maximum discrete pressures around the forward and aft columns, respectively (Table 3-10), whereas lower pressures at these areas were measured by PT#1 (0.33 kPa) and PT#16 (3.21 kPa).

Table 3-10: Deck impact pressures (kPa) around forward and aft columns versus wave crest height for condition 1 [WE#1: H = 244 mm, T_z = 1.40 s at a_0 = 120 mm].

Run id	Forward column			Aft column		
	PT#1	PT#2	PT#3	PT#14	PT#15	PT#16
1	0.407	2.73	0.707	3.56	3.12	1.65
2	0.0436	2.4	0.595	4.69	4.12	2.29
3	0.254	0.68	0.63	6.58	4.95	5.87
4	0.461	2.42	1.68	6.74	5.13	3.53
5	0.493	0.824	0.836	4.95	8.91	2.72
Mean	0.33	1.81	0.89	5.30	5.25	3.21
σ	0.19	0.98	0.45	1.34	2.20	1.64

Overall, a large variation in pressure measurements amongst repeated runs having almost identical wave condition (see Table 3-8) can be appreciated. In order to show the scatter in the measured impact pressures, boxplots were used. Figure 3-12 presents the P_i values along and across the deck underside measured by the 16 pressure transducers for condition 1. The mean value (denoted by ■) is also plotted over the boxplots, as illustrated in the plot legend. A large variation was obtained in all pressure transducers, particularly in PT#14, PT#15 and PT#16.

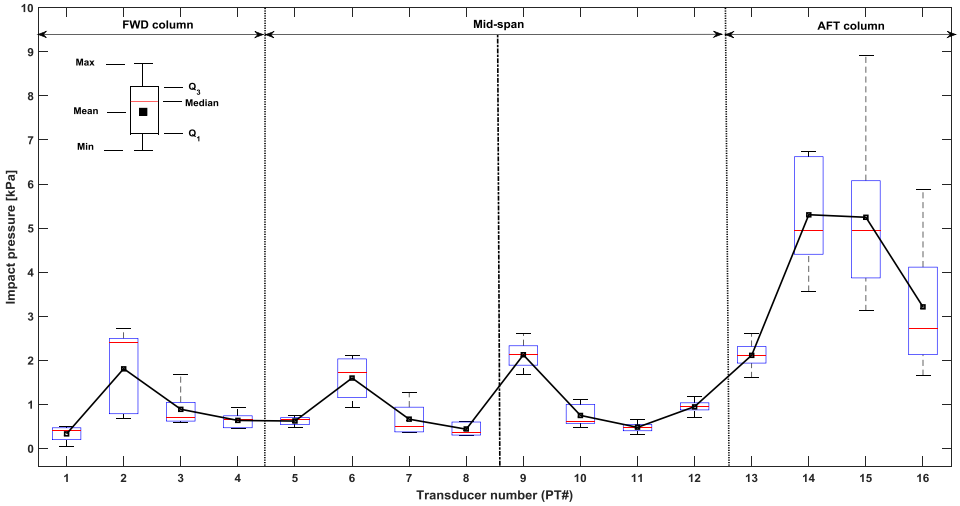

Figure 3-12: Boxplots showing variation in impact pressures measured in five runs by each transducer for condition 1 [WE#1: H = 244 mm, T_z = 1.40 s at a_0 = 120 mm].

3.6. Results and discussion

3.6.1. Time history of wave impact

Figure 3-13 shows the time history of WP4 and WP5 along with the time history of F_x and F_z. By comparing both subplots in (a) and (b), the following observations can be made:

1. As soon as the wave crest contacts the outer surface of the forward columns, the model experienced the maximum $F_x(+)$ in the recorded time history indicating that the measurements of both WP4 and the forward LC were in-phase.
2. In the interval of time from $F_x(+)$ to $F_x(-)$, the model experienced a slam force generated by the wave impacting against the front face of the deck structure; this caused the model to dynamically respond in both the *x*- and *z*-directions.
3. As the wave propagated (passing the model's centroid), the model was suddenly slammed in the upward *z*-direction $F_z(+)$ followed by a rapid decrease in $F_z(-)$. Again the model vibrated and simultaneously the wave impacted the aft columns in the positive *x*-direction near pressure transducers PT#14, 15 and 16 (Figure 3-15).
4. As the wave's trough passed through the model, $F_x(-)$ became minimal and the force started to increase due to the following wave.

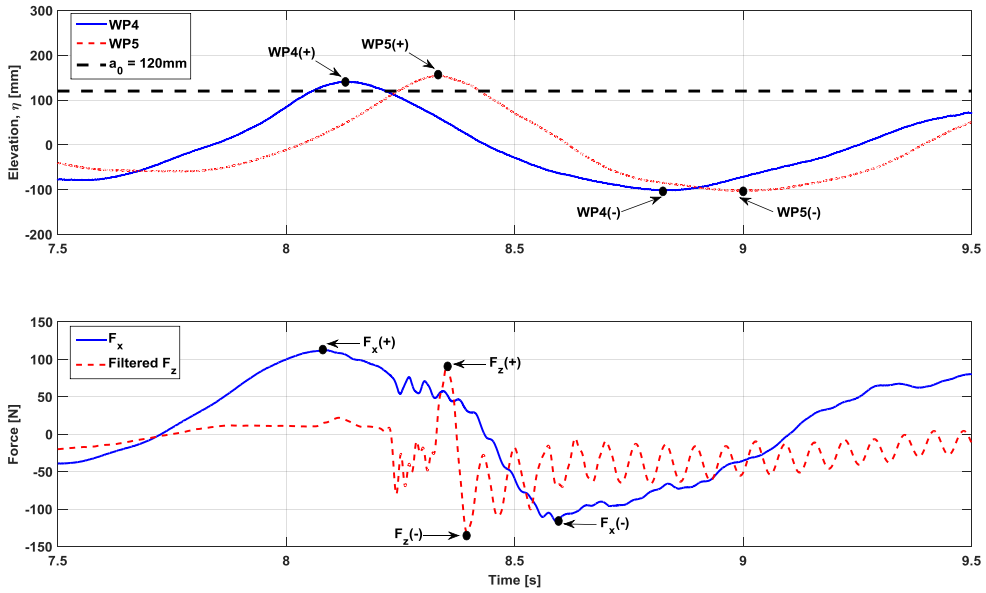

Figure 3-13: Simultaneous measurements of wave surface elevations and impact forces collected in Run 1 for condition 1 [WE#1: H = 244 mm, T_z = 1.40 s at a_0 = 120 mm]: WP4 and WP5 (top); F_x and filtered F_z at f_{c1} = 50.0 Hz (bottom).

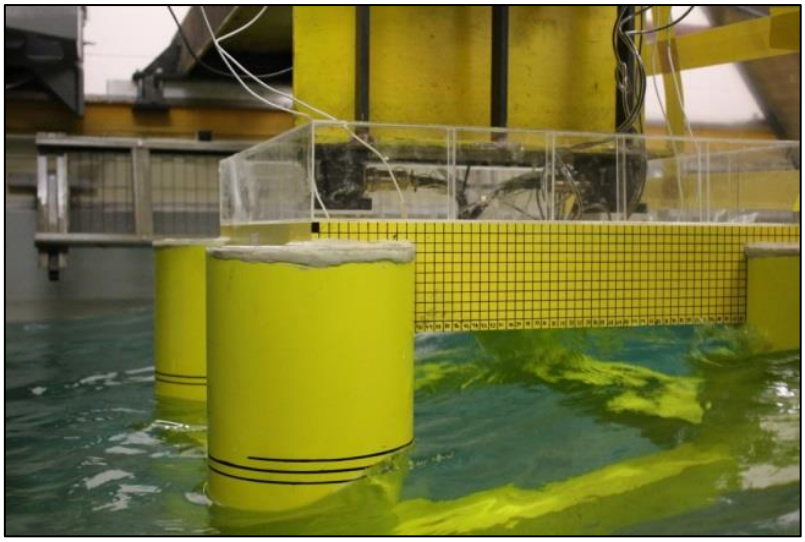

Figure 3-14: Photograph showing wave impact on the forward columns and the front face of the deck structure (waves propagating from right to left).

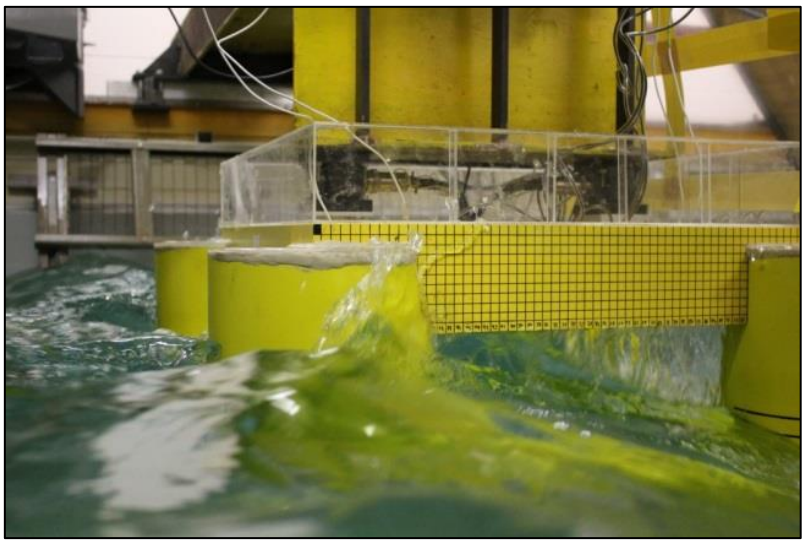

Figure 3-15: Photograph showing a water-jet impact on the aft columns and water de-attachment from the bottom plate of the deck structure (waves propagating from right to left).

For condition 1, Figure 3-16 shows the time history of PT#14, PT#15 and PT#16. The pressure signal can typically be idealised by an impulse-like shape with a peak value, P_i (slam/impact pressure) followed by a slowly-varying phase.

It should be noted that the measured pressure signals can have irregularities during the slowly-varying phase, particularly near the side edges (PT#14). This can be attributed to the air content involved in such an interaction process. It could also be due to the dynamic response of the model in the *z*-direction. The topic of hydro-elastic effects on localised wave-in-deck pressure measurements requires a further investigation.

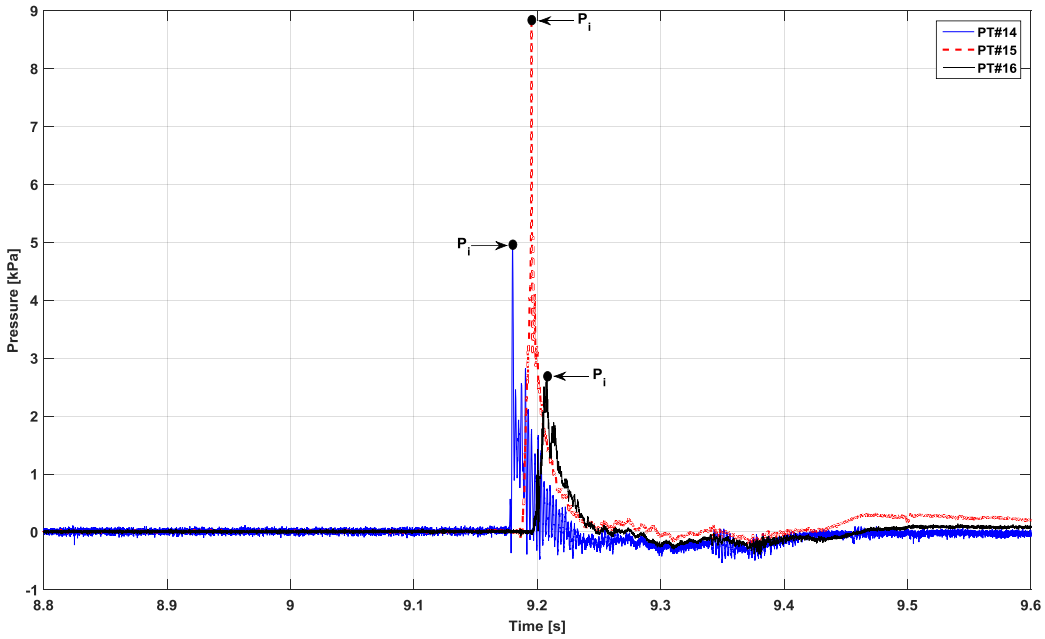

Figure 3-16: Time history of pressure transducers PT#14, 15 and 16 around the aft column measured in Run 5 for condition 1 [WE#1: H = 244 mm, T_z = 1.40 s at a_0 = 120 mm].

3.6.2. Force Peaks

Peaks of force magnitude obtained from repeated runs per test condition were averaged to provide a unique mean value. Table 3-11 summarises the averaged peak values of F_x and F_z components. In order to examine the effect of deck clearance reduction on the magnitude of F_x, the averaged force peaks measured at a_0 = 110 mm and a_0 = 100 mm were normalised by the corresponding values experienced by the model at its original deck clearance, i.e., a_0 = 120 mm (Table 3-11).

An obvious trend can be observed in Figure 3-17 between the deck clearance reduction of 10 mm and 20 mm and the force magnitude of Fx(+) and Fx(-). A consistent rise in force magnitude can be seen as the wave steepness, S, increases. For instance, at WE#5 (S = 0.10) an increase of approximately 22% for Fx(+) and 30% for Fx(-) was obtained due to a reduction of the deck clearance by 20 mm (16% of the original).

Table 3-11: Summary of averaged magnitude of the horizontal and vertical wave impact forces extracted from load cell time histories. Peaks are denoted by (+) and valleys are denoted by (-).

Condition	a_0 (mm)	H (mm)	T_z (s)	Force (N)			
				F_x(+)	F_x(-)	F_z(+)	F_z(-)
1	120	244	1.40	112.0	-114.00	91	-118
2	120	261	1.38	136.0	-130.00	98	-89
3	120	186	1.77	113.0	-78.00	18	-34
4	120	238	1.25	135.0	-112.00	56	-90
5	120	174	1.38	103.0	-90.00	76	-34
6	120	237	1.48	112.0	-101.00	54	-114
7	110	244	1.40	117.4	-142.20	48	-118
8	110	261	1.38	140.4	-141.20	168	-122
9	110	186	1.77	116.0	-92.36	71	-64
10	110	238	1.25	150.6	-124.60	78	-54
11	110	174	1.38	107.6	-82.38	147	-70
12	110	237	1.48	125.4	-117.00	72	-132
13	100	244	1.40	123.6	-143.20	75	-24
14	100	261	1.38	150.6	-145.00	210	-154
15	100	186	1.77	122.4	-96.02	42	-66
16	100	238	1.25	166.4	-143.60	51	-118
17	100	174	1.38	110.2	-93.56	191	-101
18	100	237	1.48	127.2	-126.40	85	-135

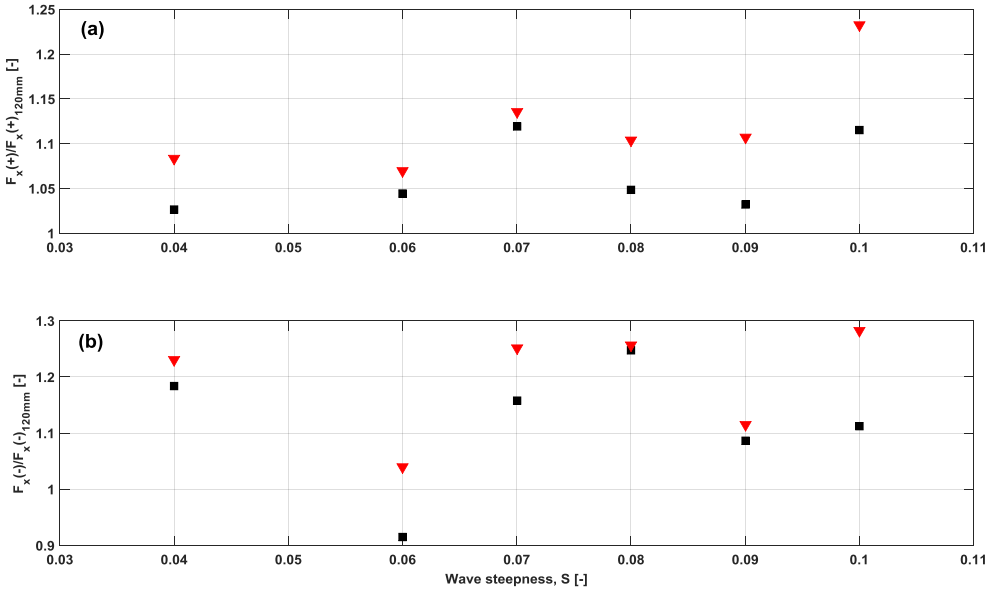

Figure 3-17: Effect of deck clearance reduction on the averaged normalised peaks of the horizontal force versus wave steepness, *S*: (a) positive *x*-direction, F_x(+); (b) negative *x*-direction F_x(-). Legend: ■ 10 mm reduction, ▼ 20 mm reduction.

The magnitude of the vertical force associated with a deck clearance or draft (see Table 3-4) due to deck impact event was assessed by normalising the averaged force peaks of F_z measured at each deck clearance with the buoyancy force F_B. The normalised increase in F_B due to the upward vertical force $F_z(+)$ is shown in Figure 3-18 (a), whilst the normalised decrease in F_B due to the downward vertical force $F_z(-)$ is shown in Figure 3-18 (b).

The effect of deck clearance on the magnitude of $F_z(-)$ is pronounced but for WE#1 (S = 0.08) such that the force magnitude was found to amplify as the deck clearance reduces. For $F_z(+)$, however, it was found that in many pairwise comparisons no effect of the reducing deck clearance can be observed. For example, at wave steepness of 0.04 (WE#3), 0.08 (WE#1) and 0.10 (WE#4) the maximum upward force does not exhibit a trend. In contrast, at S = 0.09 (WE#2) and a_0 = 100 mm the vertical force on the platform is as large as 40% of its static buoyancy. The same wave event caused a significant negative force which reached (≈ 30%) in the platform's buoyancy. It is worth mentioning that the downward vertical force may exceed the total tendon pretension for TLPs and thus, cause one or more tendons to become slack.

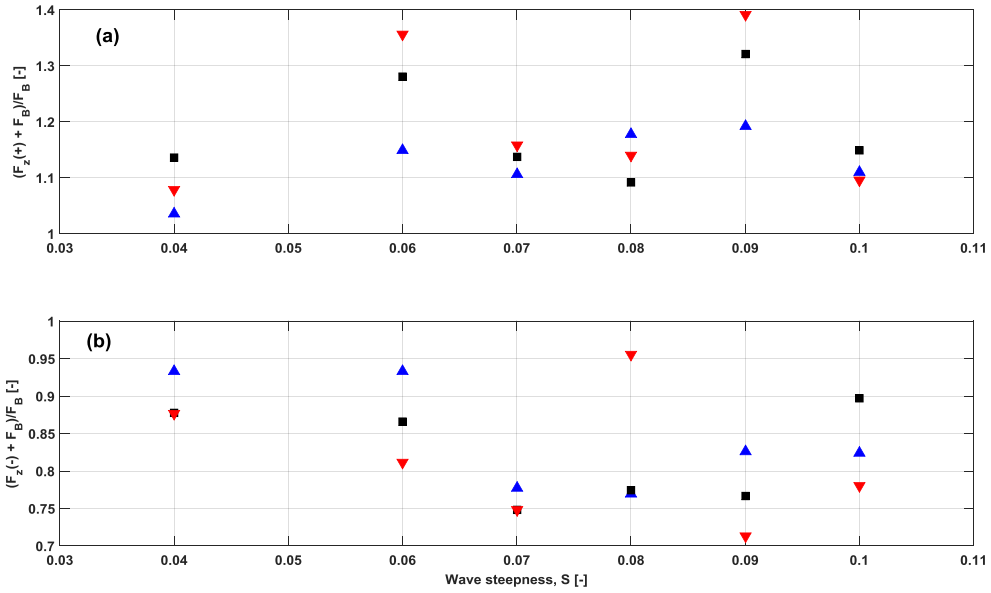

Figure 3-18: Average normalised force peaks of the vertical force versus wave steepness at different deck clearances: (a) upward direction, $F_z(+)$; (b) downward direction, $F_z(-)$. Legend: ▲ a_0 = 120 mm, ■ a_0 = 110 mm, ▼ a_0 = 100 mm.

3.6.3. Wave-in-deck loading

The mean value of P_i obtained from repeated runs was normalised by the reference dynamic pressure of a wave event and reported for all test conditions ($P^* = P_i/0.5\rho C^2$), see Table 3-6.

The average normalised values (P^*) corresponding to wave events WE#1 and WE#2 are shown in Figure 3-19. All plotted values associated with WE#1 show that the aft column region experienced large impact pressures at the different deck clearances. At lower deck clearance (a_0 = 110 mm or a_0 = 100 mm), the model experienced lower impact pressures at the aft column region (PT#14 – PT#16) than those measured at the original deck clearance, a_0 = 120 mm. This confirms the finding from the analysis of the global wave impact force $F_z(+)$ versus deck clearance, see Figure 3-18. In contrast, WE#2 against a_0 showed an increase in the localised impact pressures (the same finding was reached with $F_z(+)$, see Figure 3-18) as the deck clearance reduces.

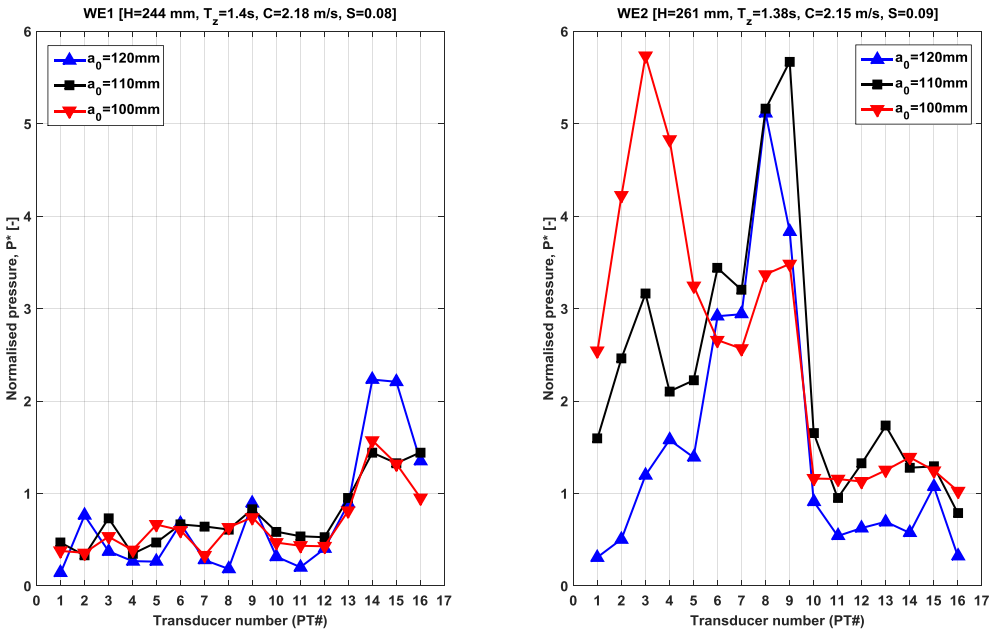

Figure 3-19: Average normalised impact pressures [$P^* = P_i/0.5\rho C^2$] measured by sixteen pressure transducers (PT) at different deck clearances: wave event WE#1 (left); wave event WE#2 (right).

Pairwise comparisons can be made between $F_z(+)$ and P^* shown in Figures 18(a) 20 and 21. The findings in pressure measurements versus deck clearance are in-line with $F_z(+)$ against deck clearance. The observed changes in P^* values versus deck clearance are consistent with those for $F_z(+)$. For instance, WE#4 (S = 0.10) shown in Figure 3-20 and WE#5 (S = 0.06) shown in Figure 3-21 indicates that there was found an effect from reducing the deck clearance on the pressure magnitudes (localised in a certain area). Despite this, no clear correlation can be seen between P^* and a_0.

The fact that the reduction in the deck clearance does not result in the increased vertical force $F_z(+)$ and localised slamming pressures may appear counterintuitive and

deserves further investigation. The following considerations may provide at least partial explanations for the observed effects:

- First, when a_0 = 110 mm the model draft is increased with the model being sunk deeper against the oncoming waves, which will increase the distortion and reflection of the waves caused by the forward columns. With an additional effect of the column overtopping, the amount of wave energy reaching into the underdeck region will be decreased and the underside of the deck will, therefore, experience decreased vertical force (F_z) and/or lower localised impact pressures.
- Second, when a_0 = 100 mm the contribution of the submerged pontoons into the vertical wave-in-deck impact force is less significant than at a_0 = 120 mm (pontoons are further from the still-water level and, therefore, attract less wave force contributing less to wave entrapment under the deck).

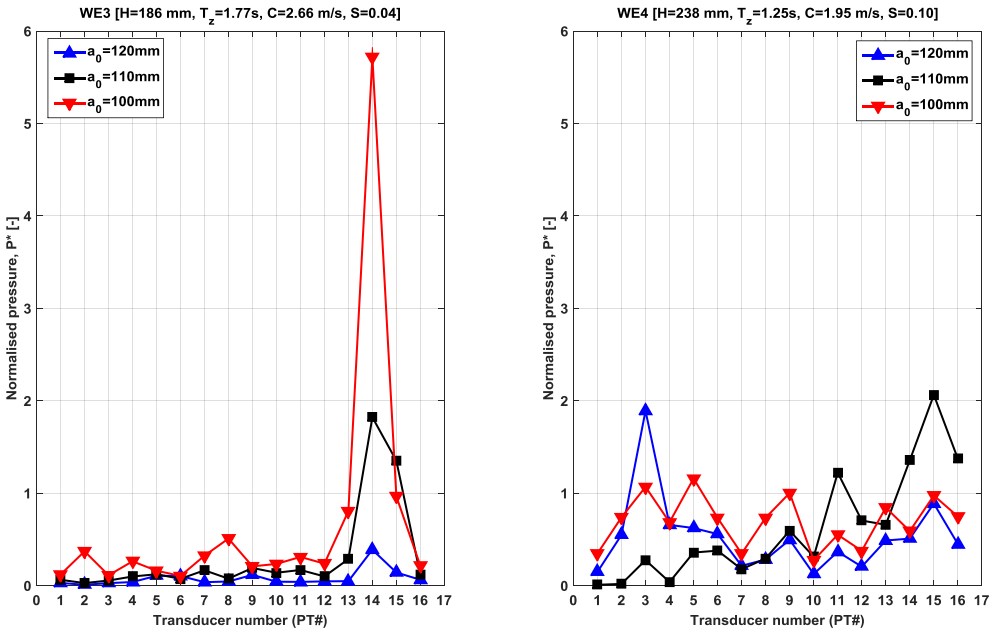

Figure 3-20: Average normalised impact pressures [P* = P_i/0.5ρC^2] measured by sixteen pressure transducers (PT) at different deck clearances: wave event WE#3 (left); wave event WE#4 (right).

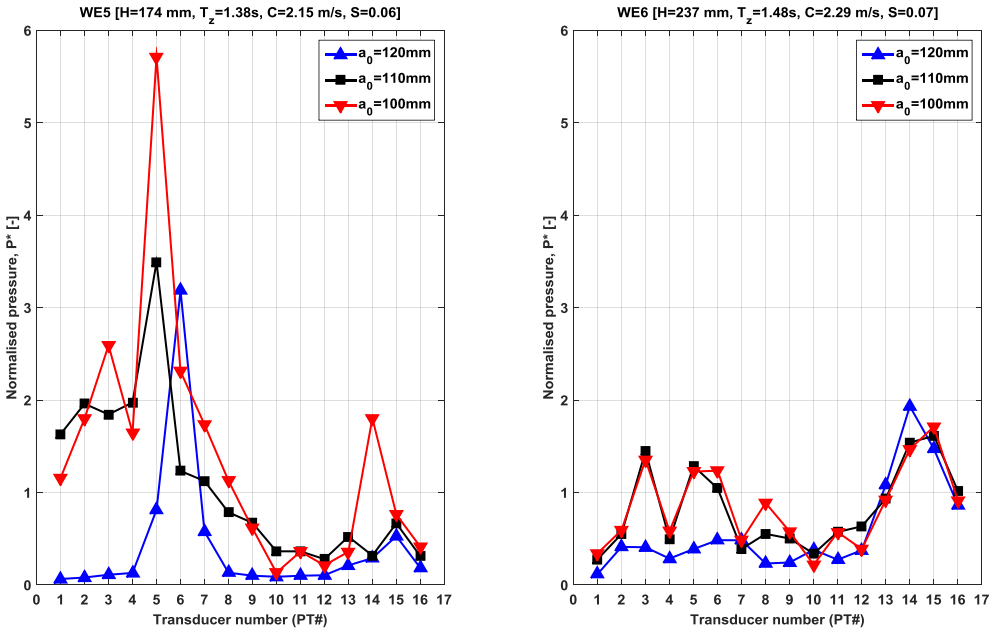

Figure 3-21: Average normalised impact pressures [P* = $P_i/0.5\rho C^2$] measured by sixteen pressure transducers (PT) at different deck clearances: wave event WE#5 (left); wave event WE#6 (right).

The results for local slamming pressure for all test conditions are combined in Figure 3-22 so that the effect of deck clearance reduction on the wave-in-deck slamming pressures at the areas of interest, i.e., the forward and aft columns can be further explained. The wave steepness, *S*, was used to establish the effect of deck clearance reduction on the average normalised impact pressures, *P**. Only with WE#2 (*S* = 0.09) the deck clearance reduction was found to have a consistent effect on the *P** values at all pressure transducers, except for PT#3 (near the side edge).

Since PT#2 and PT#15 are symmetric along the diagonal of the deck underside, when PT#2 measured larger pressures at *S* = 0.09 (short wave), PT#15 measured much lower pressures. At *S* = 0.04 (longer wave) PT#2 measured lower pressures but PT#15 measured much larger pressures. Same pairwise comparisons can be made on PT#1 versus PT#16 and PT#3 versus PT#14. This finding indicates that when the area around the forward columns experienced large slamming pressures, the area around aft columns received lower pressures and vice versa.

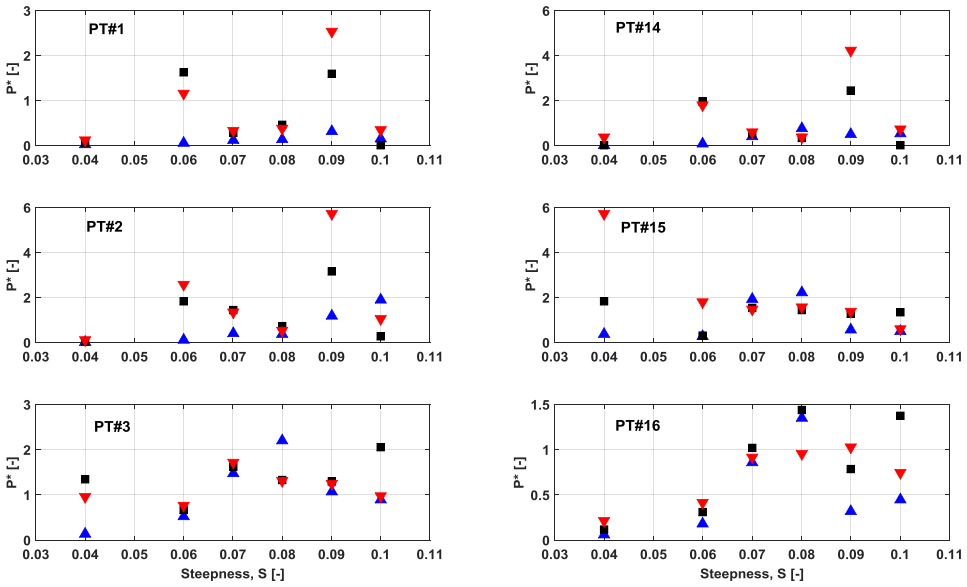

Figure 3-22: Average normalised impact pressures [$P^* = P_i/0.5\rho C^2$] versus wave steepness at different deck clearances: deck-forward column region (left); deck-aft column region (right). Legend: ▲ a_0 = 120 mm, ■ a_0 = 110 mm, ▼ a_0 = 100 mm.

3.7. Summary

On the basis of the findings reported in this chapter, the following conclusions can be drawn:

- Data analyses conducted showed that extreme wave events and the associated global horizontal forces acting on the TLP model could be generated with very good repeatability. However, the global vertical forces were found to be significantly corrupted by the structural dynamic response as observed in the force and acceleration time series and thus, this undesired effect was removed by using a low-pass filter with a carefully selected cut-off frequency.
- For local pressures, the deck-column intersection areas were found to experience large wave-in-deck slamming pressures, in particular around the aft columns. The impact pressure was found to be extremely variable in magnitude and duration, particularly at regions experience strong wave slams; large local pressures were found to be associated with high standard deviation.
- In all conditions tested, the magnitude of horizontal forces acting on the TLP model was found to be clearly affected by a small reduction in the deck clearance of 10 mm and 20 mm (1.25 m and 2.5 m full-scale, ≈ 8 %– 17% of the original deck clearance) such that the force magnitudes may be amplified by 7% to 22%.

- Conversely, the global vertical forces and local wave-in-deck slamming pressures did not show the straightforward increase when the deck clearance reduced. With an additional effect of the water reflection and the column overtopping at lower deck clearance, the amount of wave energy reaching into the underdeck region may be decreased. Further work is required to fully understand this effect.

Chapter 4: Dynamic behaviour of a tension leg platform due to wave-in-deck impact events

The work presented in this chapter is to be submitted for publication in *Ocean Engineering*. The paper has been edited for inclusion into this thesis to avoid repetition and to improve readability.

The contributing authors are: Nagi Abdussamie, Roberto Ojeda, Giles Thomas, Yuriy Drobyshevski and Walid Amin.

4.1. Scope

The present study investigates the global response of a conventional TLP due to extreme wave-in-deck events by performing experimental tests that provide both qualitative and detailed quantitative insights on the wave-in-deck impact events, rigid body motions, tendon tensions and deck slam pressures. The response of a TLP model was examined in several irregular wave events of different wave kinematics, which were taken from a typical 10,000-year return period cyclonic sea state at the Australian NWS. By conducting model tests for several extreme wave events with repeated realisations, the study aims at providing conclusions which may be broadly applicable to many floating structures of this type. The present study also aims at providing detailed results which can be used for calibrating global performance analysis software for CFD simulations. To enable the comparison of the model test results with future numerical simulations, detailed information is presented on the model and the test results, including the wave elevations measured at different wave probes which are provided in Appendix A. The time series of the measured wave elevations can be provided on request.

4.2. Model tests

4.2.1. TLP model

A box-type deck structure supported by four circular columns was designed and built to represent a TLP model. The 1:125 scaled model dimensions were based on the SNORRE-A tension leg platform [50]. The main particulars of the structure are given in Table 4-1 and Figure 4-1. Due to the limitations imposed by the 1.5 m maximum water depth of the towing tank, the scaled water depth does not represent the actual water depth of SNORRE-A. Within the constraints of the tank, a full-scale water depth of 187.5 m was deemed acceptable since this study was aimed at investigating the hydrodynamic deck loads and not the TLP response at a specific water depth. As already mentioned, wave-in-deck impact events occur when the dynamic air gap becomes negative as a result of a reduction in the static air gap i.e., deck clearance or when a huge/extreme wave exceeds the deck clearance. As the objective of the present investigation was to get an insight in typical wave-in-deck events (at small air gaps), the height of the deck of the scaled TLP model had to be defined carefully. A study of hydrodynamic loads of offshore structures due to extreme waves requires that a sufficient number of impact events due to irregular or regular waves are investigated [7]. Consequently, it was decided to decrease the deck clearance of the model by 92 mm (120 mm total deck

clearance) to ensure a sufficient number of deck impacts during irregular wave tests. The differences in deck clearance between SNORRE-A and the model used in this investigation are illustrated in Figure 4-2.

Table 4-1: Key particulars for the SNORRE-A TLP at full and model scales.

Parameter	Full scale	Tested model scale
Column diameter, D	25.00 m	200 mm
Pontoon size, $h \times w$	11.50 × 11.50 m	92 × 92 mm
Column spacing, s	76.00 m	608 mm
Column height	63.00 m	505 mm
Deck size, $L \times B \times h_d$	124.50 × 92.00 × 15.00 m	608 × 608 × 210 mm
Deck clearance, a_0	27.00 m	120 mm
Platform's draft, d	38.125 m	305 mm
Displacement, Δ	101840 t	52.15 kg
Total mass, M	77640 t	39.75 kg
Initial pretension per leg, T_o	6055 t	3.10 kg
Number of tendon per leg, n	4	1
Total tendon length at zero offset, L_o	307.00 m	1195 mm
Axial stiffness per leg, nEA/L_o	2.42×10^8 N/m	15.80 N/mm
Riser tension	3320 t	1.70 kg
Centre of gravity, C_g (x, y, z)	n/a	(0.0, 0.0, 5.0) mm
Mass moment of inertia (I_{xx}, I_{yy}, I_{zz})	n/a	(5.23, 5.23, 5.63) kg.m^2
Water depth	310.00 m	1500 mm

The model was divided into two modules, namely a hull module (columns and pontoons) and a topside deck module. Having these separate modules allowed testing of the deck individually and the deck and hull as a combined structure [61, 62] (Chapters 2 and 3 in this thesis). The model was designed to be as stiff and as watertight as possible, so as to avoid any contribution from vibrations and water sloshing in the force measurements. The hull columns of the TLP model were made of fibreglass tubes internally reinforced by plywood ring frames for added rigidity. The pontoons were made of plywood also reinforced internally by plywood frames. The pontoons and the columns were connected using epoxy glue and reinforcing fibreglass tape. As overtopping on columns was expected, the column tops were tightly closed using acrylic covers sealed using plasticine.

The 608 mm × 608 mm square deck box was constructed using a 10 mm thick aluminium plate for the deck bottom and 100 mm × 25 mm × 2.5 mm rectangular hollow section aluminium extrusions for the deck sides. A 100 mm tall acrylic bulkhead was

mounted on top of the aluminium sides to prevent green water ingress onto the deck space, as can be appreciated in the overall view of the TLP model presented in Figure 4-3.

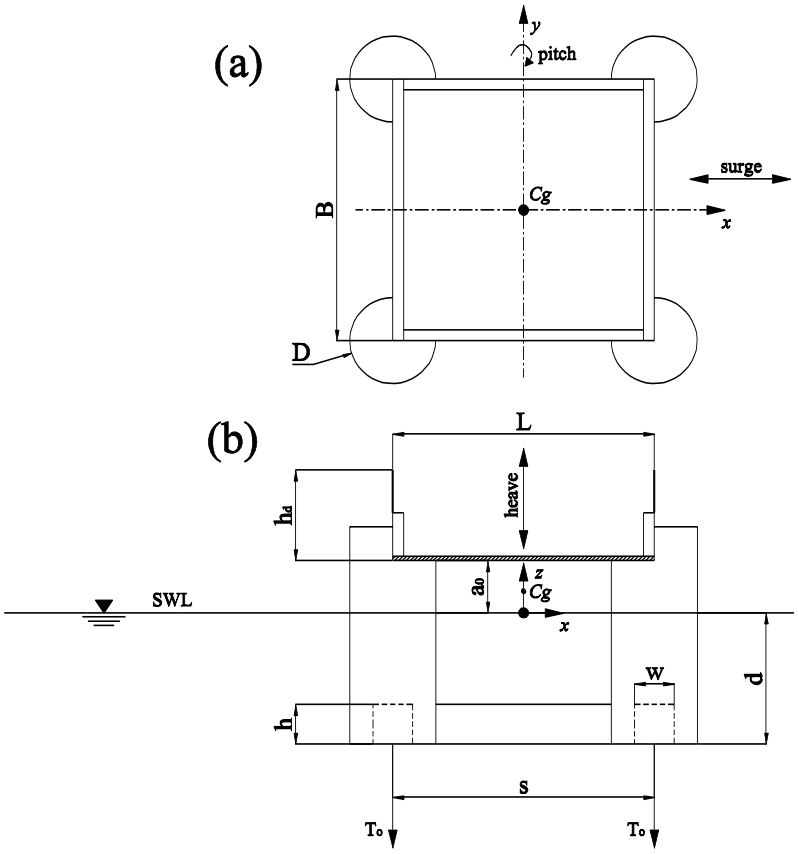

Figure 4-1: TLP model particulars: (a) top view; (b) profile view [not to scale].

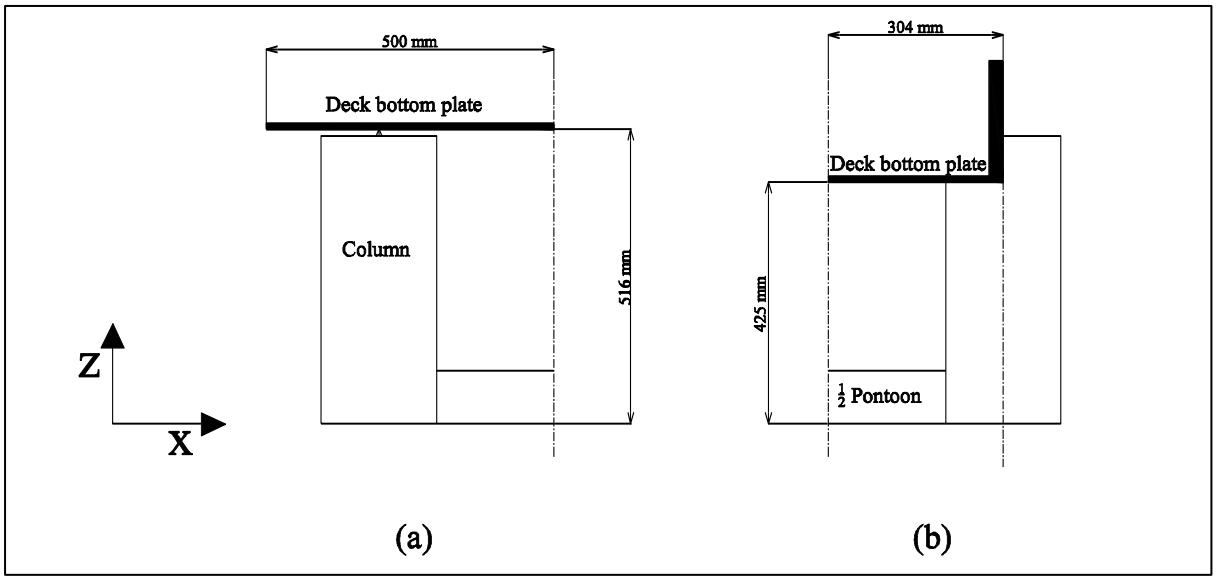

Figure 4-2: One-quarter of SNORRE TLP Deck and Hull showing a cross-section of the original and modified deck clearance given at model scale: (a) Original deck; (b) Modified deck.

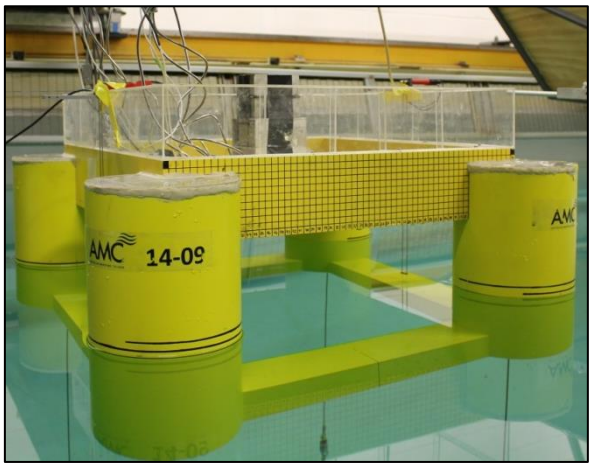

Figure 4-3: Photograph showing the TLP model (waves propagating from right to left).

4.2.2. Tendon system

In order to represent the mooring system of the SNORRE-A TLP, i.e., four tendons at each corner, one single tendon per corner was used at model scale with equivalent stiffness. The tendon rotation points at the TLP model end were located at the column base by installing a 3 axis hinge in each column at z = -305 mm, i.e., the model's keel, as shown in Figure 4-4. The anchor point of each tendon was fixed at z = -1470 mm on the towing tank floor. The actual axial compliance of the four SNORRE-A TLP tendons was modelled using custom stainless steel extension coil springs manufactured to represent the appropriately scaled stiffness. The light-mass spring (0.06 kg) with the axial stiffness of 15.80 N/mm was installed between a 3.20 mm stainless steel wire rope and an anchor base (Figure 4-4). For Leg#1 and Leg#4, the spring was connected to the wire rope and a waterproof load cell. The total mass of each 1165 mm long tendon (wire rope + spring + load cell) was measured to be approximately 0.10 kg. The use of such an assembly implies that gravity and hydrodynamic loads acting on the tendon are neglected in model tests. The 30 mm × 30 mm × 30 mm anchor base block manufactured of plastic provided a strong fixture for the model through its connection to the tank floor using stainless steel studs. In order to adjust the initial pretension, each tendon was connected to a 1.20 mm stainless steel wire run through the anchor base block to an adjustable turnbuckle with short pitch threads which was attached to the tank side; hence providing a mechanism to remotely control tendon tension.

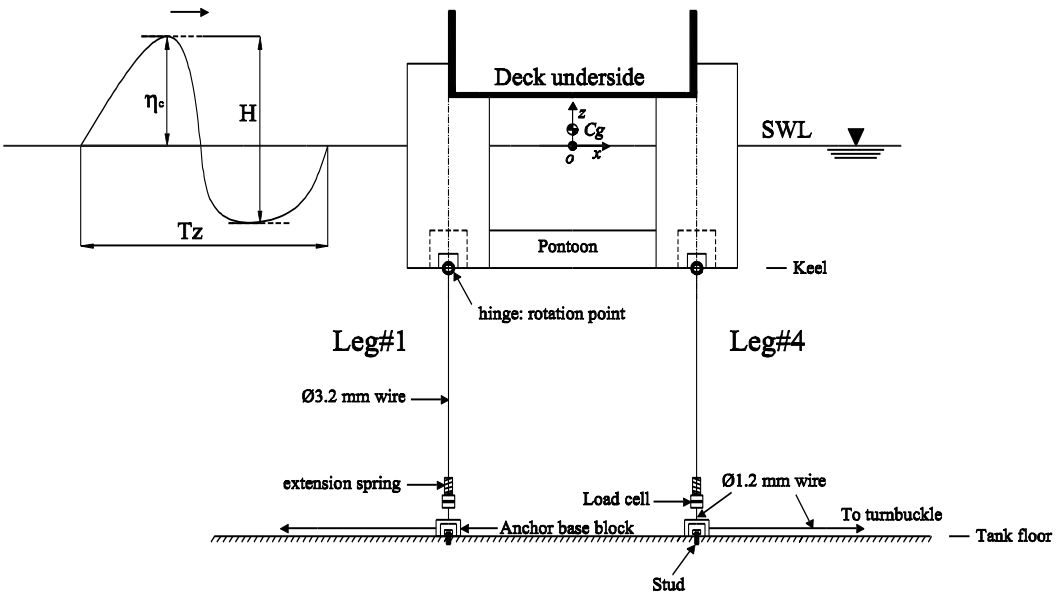

Figure 4-4: Profile view of the setup showing the TLP model attached to the tank floor; the adjustment of pretension for each leg was performed through a turnbuckle connected to the tank side.

Inclining experiments and bifilar tests were conducted to determine the vertical centre of gravity and mass moment of inertia, as given in Table 4-1. The model was ballasted to ensure that the vertical centre of gravity was maintained at approximately 5.0 mm above the SWL, or 310 mm above the keel (see Table 4-1 and Figure 4-4). The additional draft generated by the riser tension was modelled by a 1.70 kg lumped mass located 515 mm above the keel at the platform centre.

4.2.3. Instrumentation

Wave elevations

The location of the five wave probes (denoted as WP) is presented in Table 4-2 defined with respect to the origin point of the right-handed coordinate system (Figure 4-5). Wave probes WP1 – WP3 were used to measure the wave height of the incident incoming waves travelling in the positive *x*-direction. During wave impact tests wave probes WP4 and WP5 were attached to the leading and trailing edges of the topside deck.

Table 4-2: Location of wave probes used in the model tests with respect to the model's centroid.

Wave probe (WP)	Location (*x*, *y*) without the model (m)	Location (*x*, *y*) with the model (m)
1	(-10.000, 1.280)	(-10.0, 1.280)
2	(-5.000, 1.280)	(-5.0, 1.280)
3	(-1.000, 0.000)	(-1.0, 0.000)
4	(-0.404, 1.200)	(-0.304, 0.000) moving with the model
5	(0.000, 1.2000)	(0.304, 0.000) moving with the model

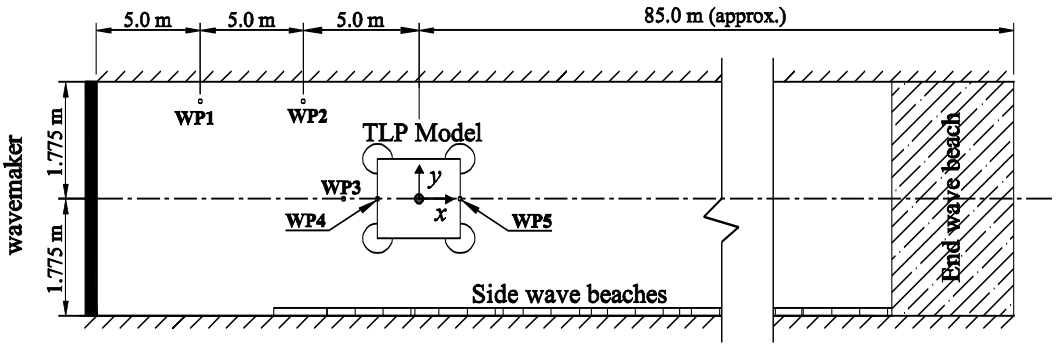

Figure 4-5: Plan view of the AMC towing tank showing the distribution of wave probes (WP) with the TLP model in-place [not to scale].

TLP motions

The model's surge motion was measured by a MagneRule magnetostrictive linear displacement transducer (MLDT), as illustrated in Figure 4-6 (b). In addition, an MTi-30 Xsens, six degrees of freedom motion measurement system was installed on the TLP model to measure the translational acceleration components as well as the model's pitch angular motion. Due to equipment limitations, this particular measurement system was not synchronised with the wave elevations, loads and surge data.

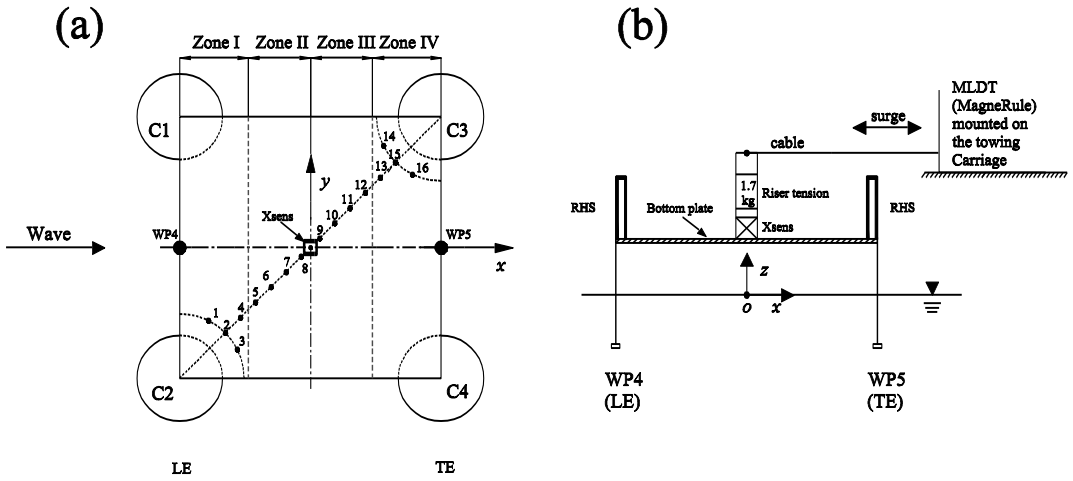

Figure 4-6: Instrumentation layout: (a) distribution of pressure transducers (PT) on the bottom plate; (b) profile view showing the instrumented deck structure by Xsens accelerometer and the MLDT.

Tendon tensions and slamming pressures

The up-wave and down-wave tendons, denoted by Leg#1 and Leg#4, respectively, were instrumented by two FUTEK submersible S-beam junior load cells (Model LSB210), see Figure 4-4. The underside of the topside deck structure was instrumented by sixteen piezoresistive pressure transducers (PT). The model specifications of the different pressure transducers (approximately 4.0 mm in diameter) and their spatial locations are the same of

those reported in Chapter 3. As already mentioned in Chapter 3, the distribution of pressure transducers along and across the deck underside was made based on a preliminary CFD study. The CFD results showed that the area around the forward and aft columns can experience large slam pressure associated with a wave-in-deck impact event (see Appendix D).

Special care was taken to ensure that the tip of each transducer was mounted flush with the underside of the deck. The pressure transducers were distributed over two main regions: forward (FWD) and aft (AFT) (Figure 4-6). The area around the forward column (C2) was instrumented by PT#1 – PT#4, whilst PT#13 – PT#16 measured wave impact pressures near the aft column, C3. The remaining pressure transducers, PT#5 – PT#12, were installed in the mid-span area. By referring to, Figure 4-6 four zones along and across the deck underside were instrumented by four pressure transducers each. Table 4-3 shows the definition of each zone. This arrangement of local pressure transducers will enable the detailed pressure distribution to be established.

Table 4-3: Definition of pressure zones at the deck underside.

Zone	Definition	Pressure Transducers (PT)
I	Around forward columns	1, 2, 3, 4
II	Forward middle section	5, 6, 7, 8
III	Aft middle section	9, 10, 11, 12
IV	Around aft columns	13, 14, 15, 16

Qualitative observations

High-speed cameras were used to capture both photographs and videos in various instants of several wave-in-deck impact events.

4.3. Experimental setup

The model tests were conducted at the Australian Maritime College towing tank, which is 100 m long and 3.55 m wide and can be operated at a maximum water depth of 1.5 m.

4.3.1. Wave calibration

A number of time series of irregular waves were generated at the towing tank using the JONSWAP spectrum for a representative 10,000-year sea state associated with a cyclonic condition at the Australian NWS: H_s = 22.13 m, T_p = 17.0 s (T_p /$\sqrt{H_s}$ = 3.61). The

corresponding scaled parameters at 1:125 were H_s = 177 mm, T_p = 1.52 s. A value of 1.0 for the peak shape parameter, γ, was selected which yields the Pierson-Moskowitz spectrum.

Short-time long-crested irregular wave trains were synthesised by the wavemaker including nine (9) wave realisations, approximately 40 s long each. These wave realisations were selected using an iterative wave calibration process without the model being in the tank by running a single wave realisation initially for approximately 120 s using a sampling frequency of 200 Hz for wave probes. The wave realisation would be selected for the subsequent tests with the TLP model if it had one or more wave events with a crest height exceeding a_0 = 120 mm at wave probes WP3 – WP5 (Table 5-1). Although this study did not aim at investigating a multitude of possible wave events, a probabilistic interpretation of this selection could be made.

Based on the Forristall short-term distribution of wave crest [7], it is expected that on average 46 wave events will exceed the static air gap a_0 = 120 mm in this sea state within a 3-hour storm. Therefore, nine (9) randomly selected realisations that contained eight (8) such events correspond to 17.4% of all waves exceeding the static deck level of a_0 = 120 mm (15.0 m full scale). This selection was considered to be sufficient for making generalisations with respect to the TLP extreme responses, although broadening the range of wave events would provide more confidence in the findings.

4.3.2. Model setup

The TLP model was set up on the tank centreline with its centroid ($x = y = 0.0$) located 15.0 m away from the wavemaker (Figure 4-5). The remaining 85.0 m of towing tank allowed for sufficiently long run times without interference from reflected waves travelling back up the tank [51].

A sampling frequency of 20 kHz was chosen for all channels in order to capture the short-duration slamming pressures. Twenty-four channels (1 for linear displacement transducer, 2 for load cells, 16 for pressure transducers and 5 for wave probes) sampled at 20 kHz produced a data file of approximately 220 MB for 40 s of acquisition time.

4.3.3. Natural periods and damping

Decay tests were conducted for the combined TLP-tendon system to measure the natural periods and system damping ratios. The logarithmic decrement method was used to determine the damping ratios. The natural periods of the TLP model were compared with the full-scale values obtained from [20], see Table 4-4. A large discrepancy in the surge natural

period was found between the target and actual experimental data, as expected, due to the incorrect water depth. The objective of the present investigation is to provide statistically reliable measurements for more accurate CFD model validations which can model the actual water depth. The natural period of surge motion was predicted by CFD with 1% error (see Chapter 5). Modelling the actual scaled water depth and the effect of truncation in the tendon length on the model's response are to be carried out in future numerical analyses. Heave and pitch natural periods agree with the full-scale data within 10% and 3.7%, respectively.

Table 4-4: Natural periods and damping ratios of the TLP.

Motion	Full scale [s]	Model: target [s]	Model: tested [s]	Model : Damping [-]
Surge	84.0	7.513	5.660	0.106
Heave	2.3	0.205	0.225	0.023
Pitch	2.4	0.214	0.222	0.123

4.3.4. Test matrix

With the TLP model being in the tank the wave parameters for each wave event (denoted by WE#) were derived from the time history of WP3 (Figure 4-5). The zero up-crossing method was employed to estimate zero crossing period, T_z, crest height, η_c, and crest to trough height, H, see Figure 4-4. Table 4-5 summarises these parameters where λ is the wavelength which was iteratively estimated from the dispersion relationship. The generated wave events were non-breaking at WP3 as indicated by the wave steepness ($S = H/\lambda$). The phase celerity, C, was estimated by λ/T_z for each wave event. The horizontal particle velocity, u, at the wave crest was estimated using the Stokes second order wave kinematics at $z = \eta_c$. It should be noted that Stokes wave theories may not be accurate in predicting the kinematics of extreme waves [36], yet, it was employed here to simplify an approximate measure of comparison between the wave events.

Table 4-5: Wave event parameters extracted from WP3 with the TLP model in-place using the zero up-crossing method.

Wave event (WE#)	H (mm)	η_c (mm)	T_z (s)	λ (m)	C (m/s)	u (m/s)	S (-)
1	231	145	1.48	3.39	2.29	0.65	0.068
2	260	163	1.37	2.92	2.13	0.85	0.089
3	238	171	1.65	4.16	2.52	0.60	0.057
4	227	137	1.35	2.84	2.10	0.72	0.080
5	186	156	1.76	4.67	2.65	0.42	0.040
6	168	126	1.73	4.53	2.62	0.37	0.037
7	191	144	1.44	3.22	2.24	0.55	0.059
8	261	160	1.46	3.31	2.27	0.77	0.079

The experimentally measured slam pressures on the deck underside, P_i, were compared with the analytical results obtained using Wang [63] formula for wave-induced uplift pressure (impact pressure) on a fixed horizontal flat plate. Although the TLP model is not a fixed, Wang's formula was used for comparison as no alternative methodology currently exists for the calculation of slam pressures on a moving deck structure. The predicted and measured P_i values were normalised by the hydrostatic wave pressure $\rho g \eta_c$ as follows:

$$P_i^* = \frac{P_i}{\rho g \eta_c} = \pi \tanh(kd) \sqrt{1 - \left(\frac{a_0}{\eta_c}\right)^2} \quad (4\text{-}1)$$

where ρ is the mass density of water, g is the acceleration due to gravity, η_c is the crest height for each wave events extracted from WP3, a_0 is the deck clearance above the still-water line, d is the water depth, k is the wave number (= $2\pi/\lambda$) and λ is the wave length, see Table 4-5.

4.4. Uncertainty analyses

The uncertainty in both time (qualitative) and magnitude (quantitative) is discussed in this section. A total of 360 s of data consisting of 9 wave realisations was collected and each of them was repeated up to five times in order to assess repeatability and accuracy in the measurements. A wave realisation that contained wave events WE#2 and WE#3 described above was employed to analyse the uncertainty in the measurements of wave elevations, surge motions, tensions in the up-wave and down-wave tendons and wave-in-deck impact/slamming pressures.

Figure 4-7 shows a 40 s long time history signal for the wave elevation measured by WP3 with the TLP model in-place during repeated runs. Two deck impacts caused by wave events WE#2 and WE#3 can be observed at time = 5.0 s – 7.0 s (WE#2) and at time = 23.0 s – 25.0 s (WE#3). Three additional crests in this time history exceeded the static deck clearance without severely impacting the deck.

The results of the uncertainty tests for the corresponding surge motion are presented in Figure 4-8 where the four repeated runs show similar results over the measured time series. The tendon tension time histories are presented in Figure 4-9 for the up-wave tendons (Leg#1) and the down-wave tendons (Leg#4) of the model.

Overall, wave elevations, tendon tension and surge motion associated with extreme wave events were found to have low qualitative uncertainty within the measured time history. On the other hand (similar to the findings reported in Chapters 2 and 3), the localised pressure measurements at discrete points of the deck were found to have much higher variability in space, time, magnitude and duration.

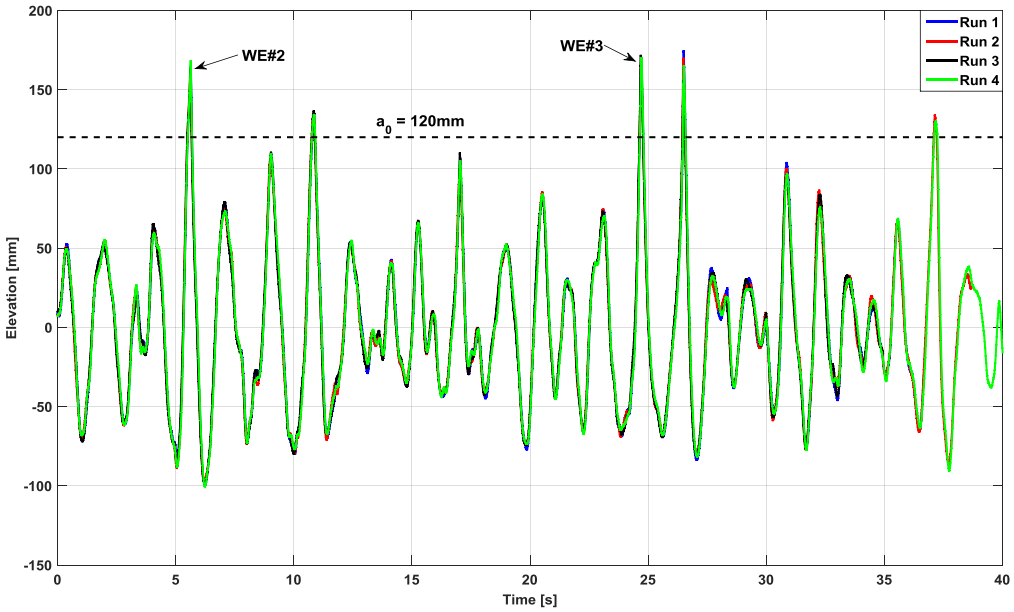

Figure 4-7: Short-time history of wave elevation measured by WP3 at 1.0 m from the model's centroid using four repeated runs.

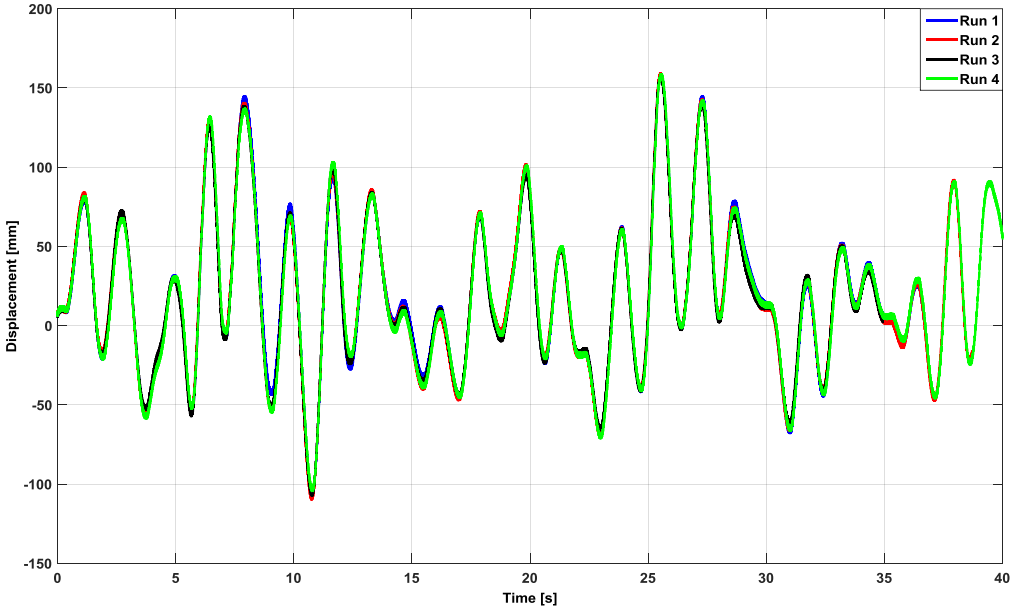

Figure 4-8: Time series showing surge motion measured using four repeated runs.

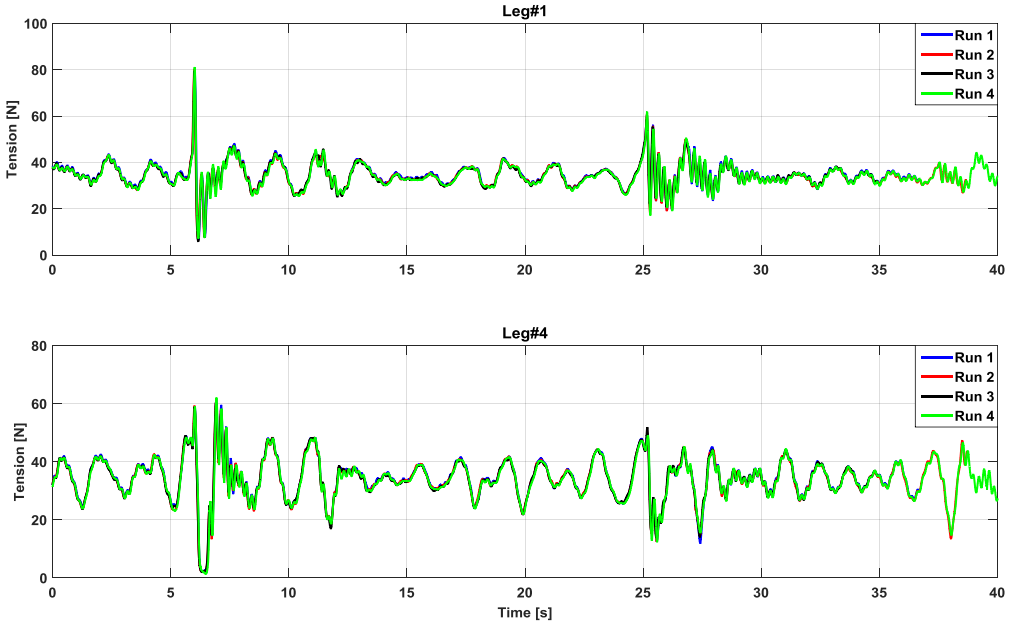

Figure 4-9: Time series showing tension in the platform's tendons measured using four repeated runs: up-wave tendon (top); down-wave tendon (bottom).

In order to illustrate the uncertainty of the pressure measurements, the time series of PT#8 (Mid-span region) and PT#16 (AFT region, near TE) corresponding to WE#2 collected in four runs is presented in Figure 4-10. All time histories of both pressure transducers show a typical trend of the pressure signal, i.e., rapid increase in magnitude followed by a slow reduction.

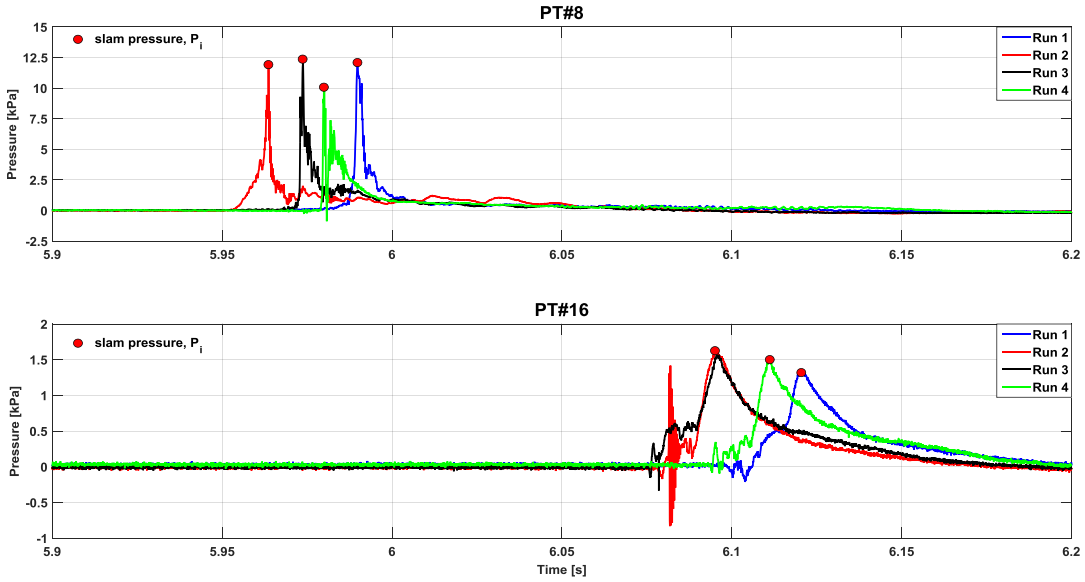

Figure 4-10: Time history of wave-in-deck pressures due to wave event WE#2 [H = 260 mm, T_z = 1.37 s] measured in four repeated runs: at PT#8 (top); at PT#16 (bottom).

In order to quantify the variability of the measured parameters in wave events WE#2 and WE#3 shown above, the peak values of the measured wave elevations at WP3, maximum and minimum tendon tensions (denoted by T_{max} and T_{min}), and slamming pressures (P_i) at PT#8 and PT#16 are summarised in Table 4-6 – Table 4-8, respectively.

Using pairwise comparisons in the associated runs (Table 4-7), the maximum tension (denoted by T_{max}) in Leg#1 was found to be consistently larger than that of Leg#4, whereas the minimum tension (denoted by T_{min}) in Leg#4 was much lower than that of Leg#1 almost to the point of experiencing slack (zero tension). The coefficient of variation (CV) for the maximum tendon tension is within 2.8% which demonstrates limited variability (or good repeatability) of these results. Maximum CV of approximately 17% for the minimum tension can be explained by small mean values, while the standard deviation of the measured results is generally the same as for the maximum tension. Another contributing factor may be the dynamic response of the load cell under impulse loading and unloading.

Table 4-6: Uncertainty analysis of wave crests and troughs (mm) at WP3 using four repeated runs for wave events WE#2 and WE#3.

Run id	WE#2		WE#3	
	WP3(+)	WP3(-)	WP3(+)	WP3(-)
1	158	-100	163	-68
2	162	-97	169	-67
3	163	-98	171	-69
4	168	-100	170	-67
Mean (mm)	162.75	-98.75	168.25	-67.75
σ (mm)	4.11	1.50	3.59	0.96
CV (%)	2.53	1.52	2.14	1.41

Table 4-7: Peak values of measured tension (N) in the up-wave tendon (Leg#1) and down-wave tendon (Leg#4) using four repeated runs for wave events WE#2 and WE#3.

WE#2 [H = 260 mm, T_z = 1.37 s]								
Leg#	Tension	Run 1	Run 2	Run 3	Run 4	Mean	σ	CV (%)
1	T_{max}	77.9	80.2	79.6	81.2	79.7	1.4	1.8
	T_{min}	6.6	7.1	5.8	7.1	6.7	0.6	9.0
4	T_{max}	61.4	60.3	60.6	62.1	61.1	0.8	1.3
	T_{min}	2.1	1.9	1.9	1.3	1.8	0.3	16.7
WE#3 [H = 238 mm, T_z = 1.65 s]								
1	T_{max}	60.1	60.6	58.2	61.6	60.1	1.4	2.3
	T_{min}	20.8	18.7	22.6	17.6	19.9	2.2	11.1
4	T_{max}	48.5	48.8	51.6	49.1	49.5	1.4	2.8
	T_{min}	17.4	15.6	16.9	13.1	15.8	1.9	12.0

The magnitude of impact pressure was found to vary among runs with a standard deviation of approximately 1.0 kPa for PT#8 and 0.122 kPa for PT#16 (Table 4-8). This corresponds to the coefficient of variation of up to 9% which is about 3 times higher than that for the maximum tension. For other pressure transducers, much higher variability was recorded, as discussed below.

Table 4-8: Impact pressures, P_i, [kPa] measured in four repeated runs at PT#8 and PT#16 due to wave event WE#2 [H = 260 mm, T_z = 1.37 s].

PT#	Run 1	Run 2	Run 3	Run 4	Mean	σ	CV (%)
8	12.08	11.96	12.32	10.05	11.6	1.05	9.0
16	1.34	1.62	1.57	1.51	1.51	0.12	8.0

In order to demonstrate the variability of the impact pressure measured by all transducers in different test runs, boxplots were used, refer Figure 4-11 for wave event WE#2. A large variability can be seen along and across the impacted deck underside, particularly at PT#6. For instance a coefficient of variation (≈ 70%) was obtained at PT#1 and PT#6. Boxplots corresponding to all wave events analysed in this study are given in Appendix A.

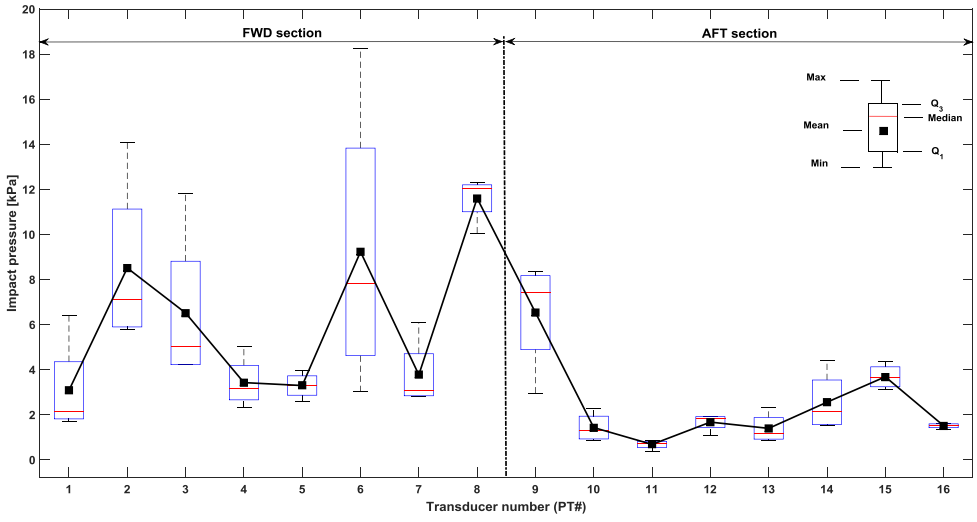

Figure 4-11: Boxplots showing variation in impact pressure at different pressure transducers due to wave event WE#2 [H = 260 mm, T_z = 1.37 s].

4.5. Results and discussion

A complete set of results for all wave events, including time histories of wave elevations at deck leading edge (LE) and trailing edge (TE), surge motion of the platform and tendon

tensions are presented in Appendix A. In this section, selected results are discussed to interpret the observed behaviour of the TLP model.

4.5.1. Model's dynamics due to wave-in-deck impact

Short time histories of the wave elevations at LE and TE, platform surge motion and tendon tensions are shown in Figure 4-12 for wave event WE # 1, as an example. For the interpretation of the platform dynamics, it is convenient to introduce several parameters, which are schematically illustrated in Figure 4-13. In this figure, the position of the deck is defined in the local coordinate system (x, z) with its origin at the deck LE in the static condition. The following parameters are defined:

- Time instances of the initial contact t_o, maximum tension in the up-wave tendon t_i, end of contact with the LE t_m and end of contact with TE t_f.
- Relative coordinates of the deck LE at the corresponding time instances $x(t)$.
- Time of the up-wave tendon tension build up $dt = t_i - t_o$.
- Time of interaction with LE : $dt_{LE} = t_m - t_o$.
- Platform velocity at the initial contact U_o.
- Platform velocity at time of maximum tension in the up-wave tendon $U = (x(t_i) - x(t_i))/dt$;
- Relative velocity of the wave crest and the platform $u_r = u - U$.

With reference to Figure 4-12and Figure 4-13, the behaviour of the platform due to the wave-in-deck event can be described as follows:

- At time t_o = 31.74 s, the wave contacted the deck LE at $z = a_0$ = 120 mm. The horizontal position of the deck LE was x_o = -61.28 mm and the model was moving in the positive x-direction (along with the wave) with the velocity U_o = 0.09 m/s. The up-wave tendon (Leg#1) was under tension $T' = T_o + \Delta T \approx$ 37.40 N.
- At time t_i = 31.90 s, the wave crest was in contact with the deck LE, which was at the position x_i = -19.95 mm. The model was now moving with a higher velocity $U = dx/dt \approx$ 0.30 m/s and the relative horizontal velocity ($u_r = u - U$) between the wave crest and the model was 0.39 m/s. At this time, the up-wave tendon came under the maximum tension T_{max} = 48.00 N.
- At time t_m = 32.03 s, the wave crest was leaving the deck LE, which was at x_m = 21.40 mm. During the time interval $[t_i, t_m] \approx$ 0.13 s, the tension in the up-

wave tendon decreased rapidly to approximately the same value T' that was experienced at the initial contact. As such, the up-wave tendon experienced impulse-like loading over 0.28 s at model scale (3.13 s at full scale).

- At time t_f = 32.03 s, the wave was tangentially leaving the deck TE. The position of the deck LE was at x_f = 93.40 mm. The down-wave tendon (Leg#4) was under very low tension (3.60 N) while the tension in the up-wave tendon also reduced (24.93 N).

Based on Figure 4-12, the minimum tensions in both tendons occurred after time t_f, when the down-wave tendon became slack. This was followed by a rapid increase in tension and a number of ringing oscillations in the down-wave tendon. The up-wave tendon also showed ringing response with smaller amplitudes.

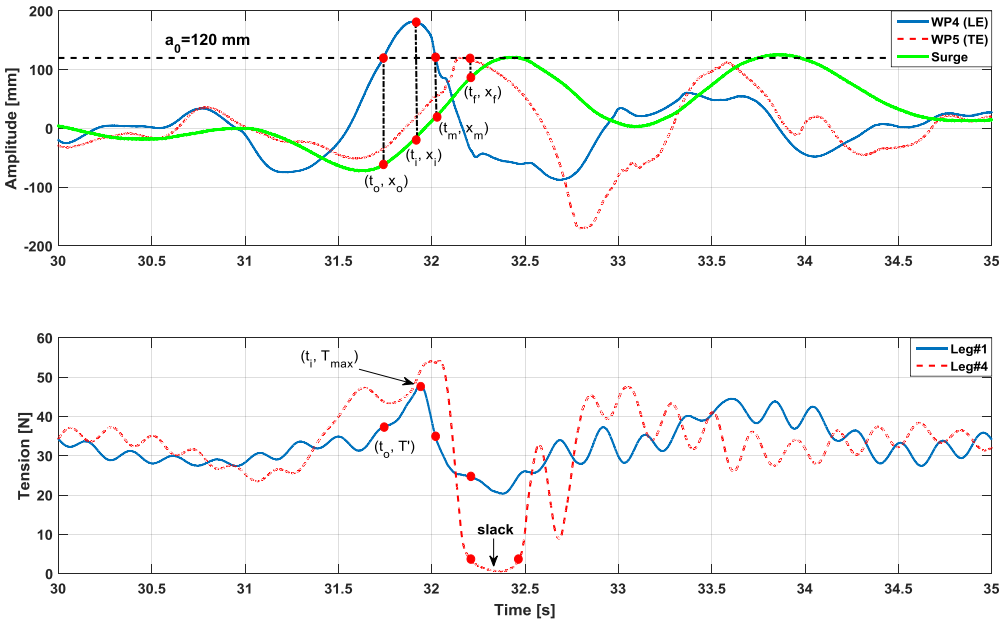

Figure 4-12: Simultaneous measurements corresponding to wave event WE#1 [H = 231 mm, T_z = 1.48 s]: wave elevations at WP4 and WP5 and surge motion (top); tension in the up-wave and down-wave tendons (bottom).

Table 4-9 summarises all the key parameters for all wave events. The following observations were made:

- In all cases, at the time of the initial contact between the wave and the deck LE, the model was moving in the positive x-direction with velocity, U_o, in the range of 0.09 – 0.32 m/s. The fact that the model was always moving with the waves at the time of the initial contact suggests that such behaviour is caused

by wave-induced hydrodynamic forces on the columns and pontoons in the time immediately before the deck impact.

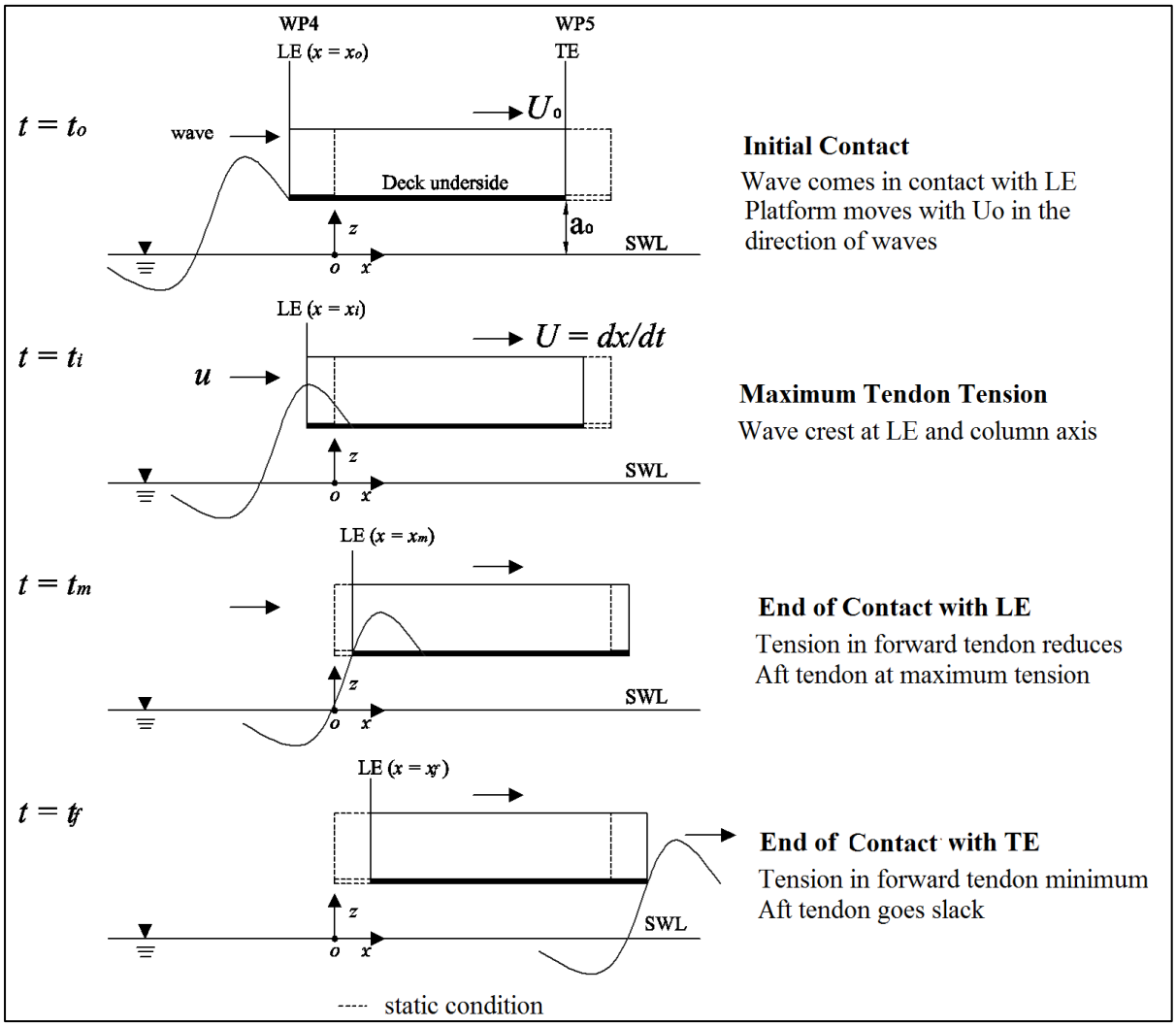

Figure 4-13: Sketch definition showing the interaction between wave event WE#1 and the topside deck structure both moving in the positive *x*-direction. The time sequence is given from top to bottom [not to scale].

Table 4-9: Summary of time instants and model response during the wave-structure interaction.

Wave event (WE#)	T_z (s)	u (m/s)	x_o (mm)	x_i (mm)	dt (s)	U_o (m/s)	U (m/s)	u_r (m/s)	dt_{LE}/T_z (%)
1	1.48	0.65	-61.28	-19.95	0.16	0.09	0.26	0.39	19
2	1.37	0.85	-3.44	20.64	0.06	0.32	0.37	0.48	9
3	1.65	0.60	27.17	62.59	0.09	0.30	0.39	0.21	9
4	1.35	0.72	10.88	34.38	0.09	0.24	0.27	0.45	11
5	1.76	0.42	-33.46	-15.27	0.12	0.09	0.15	0.27	16
6	1.73	0.37	-55.83	-36.55	0.08	0.14	0.24	0.13	10
8	1.46	0.77	-47.43	-5.86	0.14	0.16	0.30	0.47	20

- In all cases, the model's translational velocity increased to a higher value of U = 0.15 – 0.39 m/s during the active phase of the wave-in-deck event (dt). As a result, the relative horizontal velocity, u_r, between the wave crest and the deck was always smaller compared with a similar situation for a fixed structure. This reduction in the relative velocity is of the order of 50% on average, compared with the wave particle velocity u in the undisturbed wave crest.
- On average, the wave remained in contact with the deck LE over the time of approximately 13% T_z, and during this time, the up-wave tendon experienced its peak loading.
- Similar wave events (WE#2 and WE#8) were found to cause similar model's dynamics in terms of the relative velocity. However, differences in dt_{LE}/T_z were obtained, which could be attributed to the difference in T_z and the initial position x_o between various wave events.

Figure 4-14 shows the interaction between WE#1 and the model during the water-entry and water-exit phases.

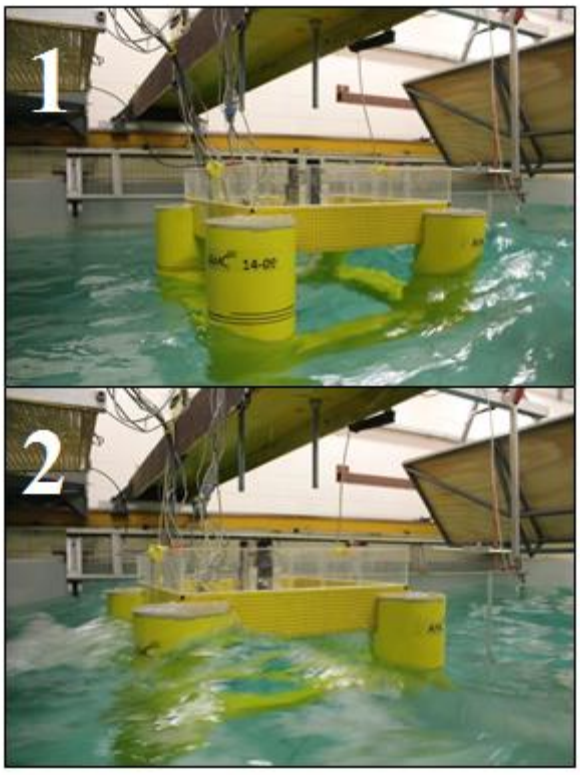

Figure 4-14: Photograph showing wave impact at the TLP model due to wave event WE#1: (1) water entry at time ≈ t_o; (2) water exit at time ≈ t_f (wave propagating from right to left).

4.5.2. Slack tendon situations

The slack tendon situations were only observed in the down-wave tendon due to wave events WE#1, WE#2 and WE#8. The measurements of wave elevation at TE suggest that these wave events must have caused significant downward forces on the model.

Wave events WE#2 and WE#8, which showed similar wave characteristics, were found to produce similar slack tendon situations, both in terms of magnitude and duration. The time during which the down-wave tendon remained slack (t_{slack}) was found to be 0.30 s for WE#1 (Figure 4-12), 0.34 s for WE#2 (Appendix A: Fig.A 3) and 0.25 s for WE#8 (Appendix A: Fig.A 15), see Table 4-10. As such, the full-scale platform may experience the slack tendon situation over a period of 3 – 4 s. Consistent with these situations, large pitch response was measured with the maximum pitch angles in the down-wave direction of 0.80° for WE#1, 0.67° for WE#2 and 0.65° for WE#8.

Table 4-10: Slack tendon situations in the down-wave tendon.

Waver event (WE#)	Minimum tension, T_{min} [N]	Slackness duration, t_{slack} [s]	t_{slack}/T_z [%]	Max pitch angle (°)
1	0.46	0.30	20	0.80
2	1.78	0.34	25	0.67
8	1.41	0.25	17	0.65

4.5.3. Tendon ringing response

In all wave events, the TLP model was found to experience high-frequency vertical motions with the period close to its natural heave period (0.225 s), known as "ringing". The short-term transient ringing response was observed in both up-wave and down-wave tendons. The energy spectra of both tendon tensions for wave event WE#1 are presented in Figure 4-15, for the time window of 31.9 s – 40 s (starting from t_i in Figure 4-12). The figure shows significant energy around the heave natural frequency, whereas the spectrum of the wave elevation (measured by WP 4) has almost no content at this frequency. This indicates that the tendon ringing is caused mostly by the wave-in-deck impact.

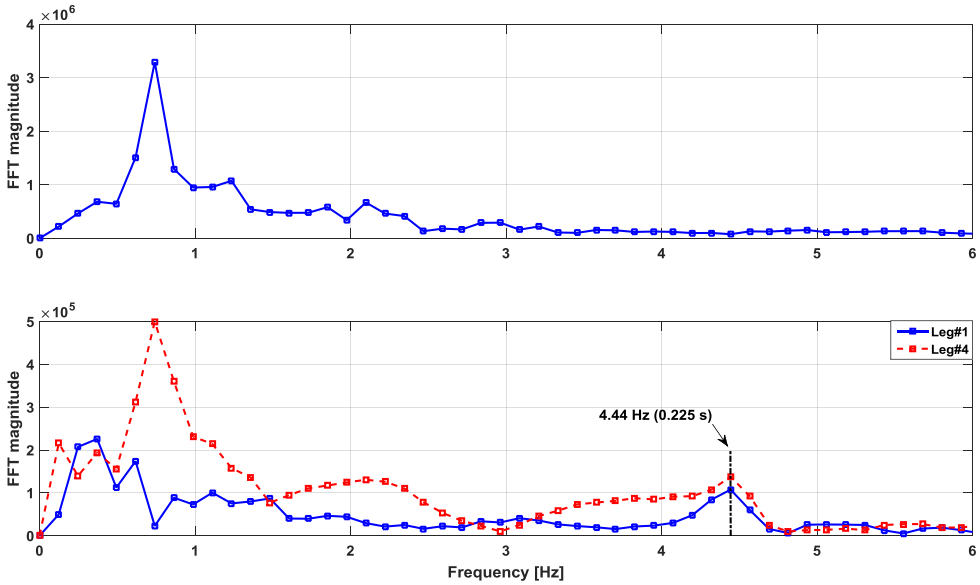

Figure 4-15: FFT results for time series of wave elevation at wave probe WP4 (top) and tension in the up-wave and down-wave tendons (bottom) acquired during and subsequent to the deck impact caused by wave event WE#1 [H = 231 mm, T_z = 1.48 s].

The extended set of results, presented in the Appendix, indicates that ringing response was presented in almost all wave events. In some cases, the high-frequency content in the tendon tensions was detected before or even without the wave-in-deck impact event. In these situations, further analysis is required to separate the ringing response caused by the wave-in-deck events from "springing" response likely caused by the sum-frequency second order loading. Nevertheless, such analysis falls outside the scope of this study. The tension time histories of ringing response associated with each wave event was identified using the following procedure:

- If the TLP was subjected to a single wave-in-deck impact the ringing was found to be noticeable in the tendon time history only after the point of minimum tendon tension. In the rare cases where the TLP was subjected to two consecutive wave-in-deck impacts, the ringing response caused by the preceding wave was found to be noticeable along the entire time history of the second impact after the point of minimum tendon tension.
- The ringing duration was defined by the number of oscillations observed in the tendon tension time history for each leg until the ringing magnitude approximately vanished;

- The maximum and minimum magnitude of each oscillation observed within the ringing time history was extracted to obtain a tendon tension range *(T_r)* for each significant cycle (T_r = maximum tension – minimum tension); and
- The tendon tension ranges were then grouped as a portion of the tendon pretension such that the number of occurrences of the ringing response could be determined for the sea state under investigation.

Examples of the ringing response identified in wave events WE#1 – WE#8 for the up-wave and down-wave tendons are presented in Figure 4-16 where the tendon tension range was normalised using the tendon pretension ($T^*_r = T_r / T_o$).

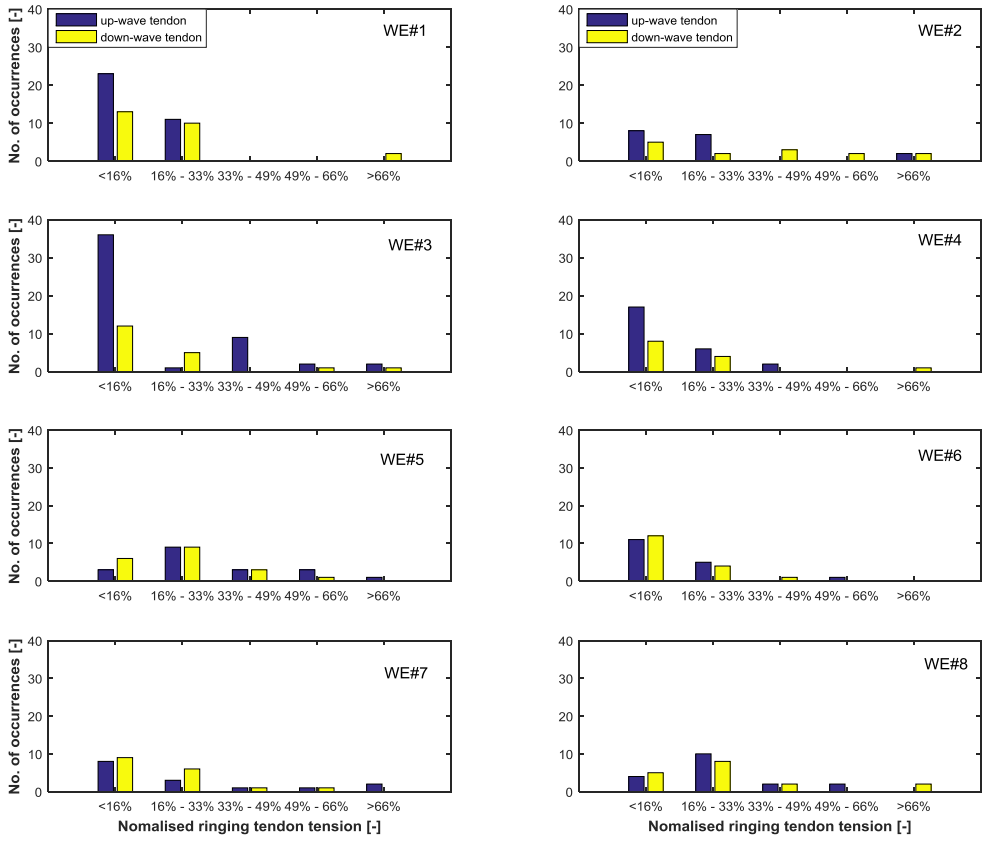

Figure 4-16: Normalised ringing tension in the up-wave and down-wave tendons caused by the examined wave events versus the number of occurrences.

In most cases, as expected, the number of occurrences (*N*) was inversely proportional to the tendon tension range for both tendons. Wave events WE#3 and WE#1 caused the largest number of occurrences, such large *N* values occurred in the up-wave tendons, with ringing magnitudes exceeding the tendon pretension by approximately 15%. As already seen in Figure 4-7, wave event WE#3 was followed by a successive steep wave which may have

lead the platform to oscillate in heave for a long time. This finding revealed that while the platform may avoid the second deck impact from a successive large wave (due its dynamic response), the successive wave might largely contribute to the ringing response. On the other hand, the ringing response due to long-crested steep waves in the down-wave tendon (Leg#4) was found to be less significant than that was observed in the up-wave tendon (Leg#1). This may be attributed to the large contribution of localised wave slams being acting in the up-wave section of the deck underside in most cases. On average, the mean magnitude of ringing tension for Leg#1 and Leg#4 was found to be almost equal for all wave events. Wave events WE#2 and WE#8 were found to be similar and led to a quite similar ringing response in terms of ringing tension magnitude and number of occurrences.

4.5.4. Maximum and minimum tension

The magnitudes of maximum and minimum tendon tension measured in repeated runs were averaged and summarised in Table 4-11 for all wave events. The maximum tensions in the up-wave and down-wave tendons corresponding to each wave event are of approximately the same level, except for wave events WE#1 – 3, without a clear trend of higher tension being experienced by the up-wave or down-wave tendon. The minimum tension in Leg#4 is significantly lower than that in Leg#1, particularly in wave events WE#1, WE#2 and WE#8, when the down-wave tendon became slack. In order to compare the extreme tensions, they were normalised using the tendon pretension, T_o = 30.4 N. The normalised maximum tension ($T^*_{max} = T_{max}/T_o$) and minimum tension ($T^*_{min} = T_{min}/T_o$) are shown in Figure 4-17 against the wave steepness. In most conditions, T^*_{max} seems to increase as the wave steepness does which is in line with the expected trend. Notably, two extreme events WE#2 and WE#3 produced the maximum tendon tension of approximately 2.5 times the pretension. It is important to note that, out of all wave events studies, the maximum tendon tension occurred in the up-wave tendon in wave event WE#2, which is characterised by the highest wave steepness rather than the highest wave crest.

With respect to the minimum tension, there is a trend for the down-wave tendon to experience less tension as the wave steepness increases, whereas the minimum tension in the up-wave tendon does not show a significant change. Another observation is that out of all events studied, that minimum tendon tension occurred in wave event WE#1, which is characterised by moderate crest height and also moderate wave steepness. This indicates that selection of a particular wave event which may produce the highest tension or the lowest tension (including the slack tendon situation) is not a straightforward task.

Table 4-11: Average maximum and minimum tensions (N) measured in the up-wave tendon (Leg#1) and down-wave tendon (Leg#4) for different wave events.

WE#	H [mm]	T_z (s)	S (-)	Leg#1		Leg#4	
				T_{max}	T_{min}	T_{max}	T_{min}
1	231	1.48	0.068	47.08	18.83	54.33	0.46
2	260	1.37	0.089	79.69	6.66	61.11	1.78
3	238	1.65	0.057	60.13	19.92	49.51	15.75
4	227	1.35	0.080	39.90	28.70	43.73	14.90
5	186	1.76	0.040	50.48	13.04	45.30	13.43
6	168	1.73	0.037	38.30	21.67	45.82	15.27
7	191	1.44	0.059	53.78	22.00	49.64	8.00
8	261	1.46	0.079	67.63	17.99	67.34	1.41

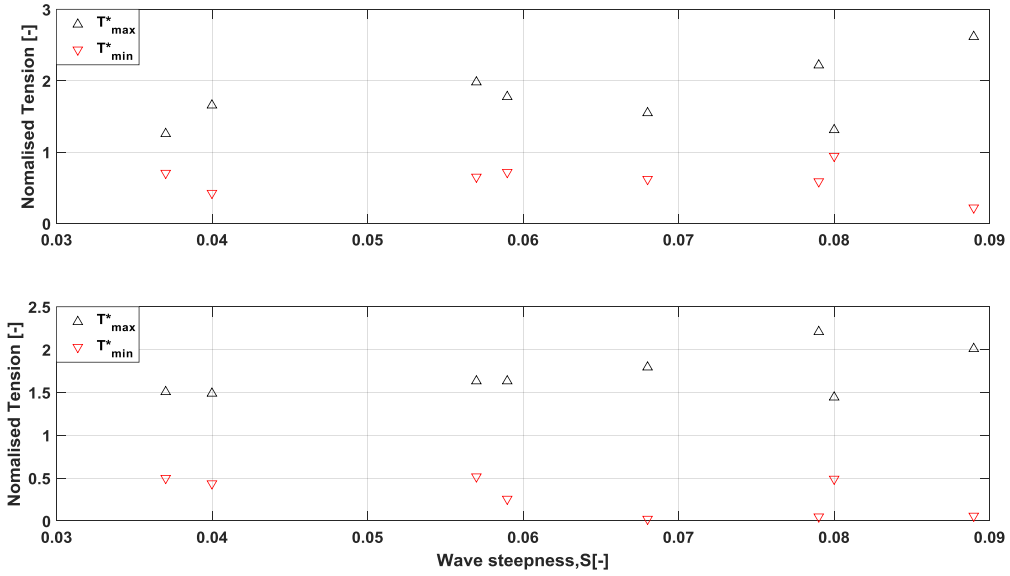

Figure 4-17: Average normalised tension ($T^*_{max} = T_{max}/T_o$, $T^*_{min} = T_{min}/T_o$, T_o = 30.4 N) versus wave steepness: up-wave tendon, Leg#1 (top); down-wave tendon, Leg#4 (bottom).

4.5.5. Wave-in-deck slamming pressures

The normalised measured slam pressures (average) for all wave events were compared with the ones obtained using Wang's equation (Eq. 4-1). Figure 4-18 through Figure 4-21 show the normalised slam pressure in zones I – IV of the model, respectively. For the definition of each zone, refer to Table 4-3. There is a general trend for the pressure to increase with increasing deck exceedance $\epsilon = 1 - a_0/\eta_c$. With the exception of very extremities of the deck (i.e., except PT #1, 16 and #2, 15) the impact pressure in the forward part of the deck is higher than in the aft part (data in Figure 4-19 versus data in Figure 4-20). By check-crossing between the areas of forward and aft columns (PT #1, 16 and #2, 15), in

most cases, pressure near the aft end of the model deck is higher than that near the front end (i.e., pressure at PT#16 is larger than that at PT#1; similarly for PT#15 and PT#2).

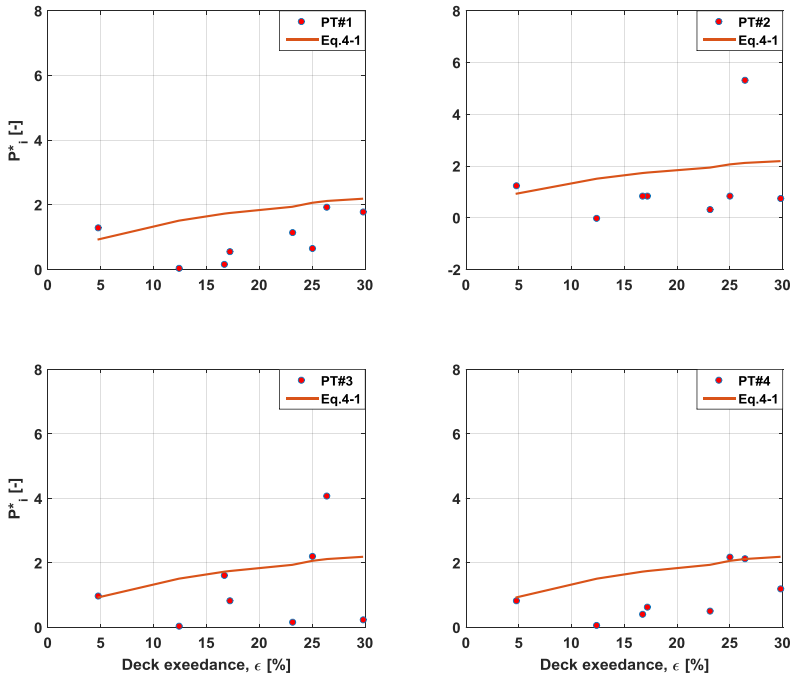

Figure 4-18: Normalised slam pressure distribution in the zone I (around the forward columns).

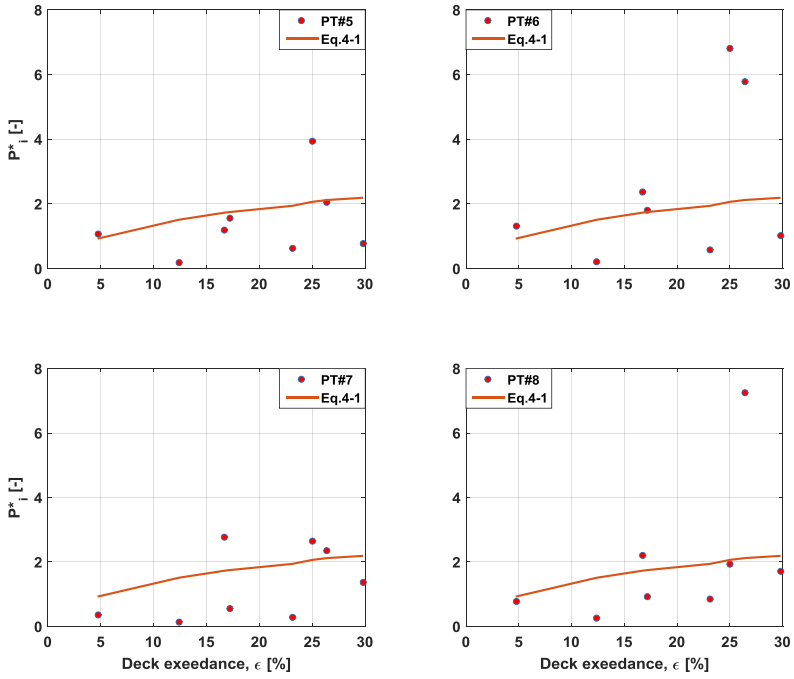

Figure 4-19: Normalised slam pressure distribution in the zone II (forward middle section).

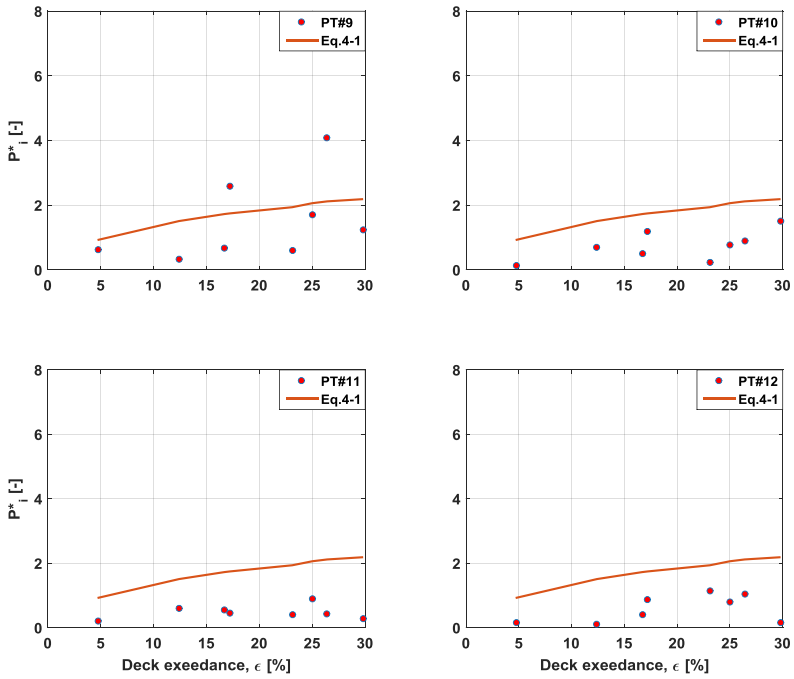

Figure 4-20: Normalised slam pressure distribution in the zone III (aft middle section).

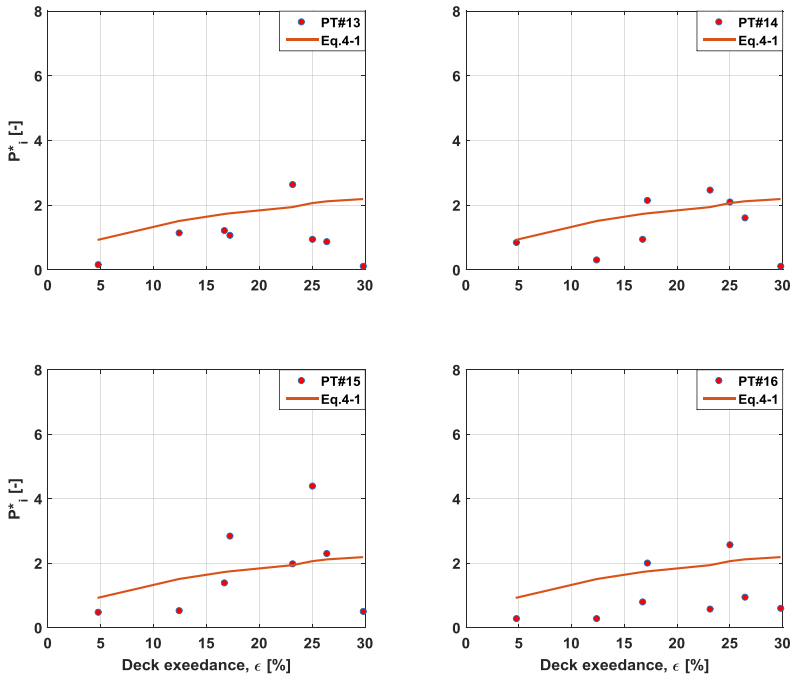

Figure 4-21: Normalised slam pressure distribution in the zone IV (around the aft columns).

4.5.6. Tendon tensions versus impact pressure

Maxima of tendon tensions and localised pressures in the forward and aft regions are presented in Figure 4-22. This presentation suggests that correlation exists between the maximum tendon tension and the localised pressure measured around the columns of the deck underside in the respective part of the structure. This is an expected result, which confirms that wave-in-deck local loads are sufficiently large to affect the maximum tendon tensions, over a number of wave events considered in this study.

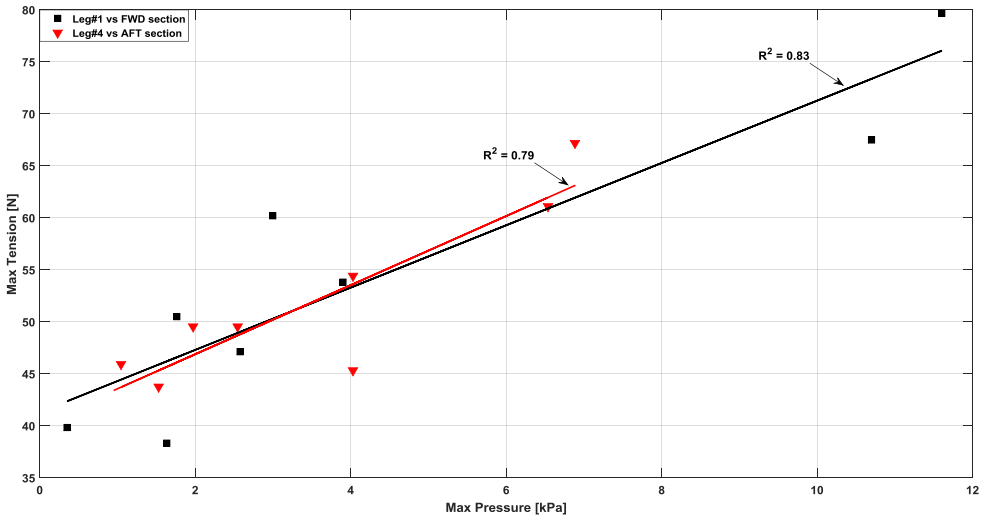

Figure 4-22: Maximum tension measured in the up-wave tendon (Leg#1) and down-wave tendon (Leg#4) versus maximum pressure measured in the forward and aft sections of the deck underside.

4.6. Summary

This experimental investigation has provided detailed information on the global behaviour of a TLP due to wave-in-deck events in abnormal waves, which can be used for calibrating analytical tools and CFD models. Analysis of measured results and observations of the model response also enabled several general conclusions to be drawn:

Variability of measurements in model test

- Based on repeated test runs (4 – 5 times) with an identical irregular wave train, it was found that wave elevations, tendon tension and surge motion of the platform were repeatable parameters, with limited variability (coefficient of variation within 2.8 %).
- The localised impact pressures at discrete points on the deck underside had higher variability in space, time, magnitude and duration. The coefficient of variation for the maximum pressures over 4 – 5 test runs was up to 72%. A

sufficient number of runs (more than five) are therefore recommended to obtain reliable mean pressure values in such model tests.

Platform dynamics due to extreme wave impact

- In all extreme wave events, the wave came in contact with the leading edge of the deck when the platform was moving in the direction of the wave. As the platform surge velocity further increased, this effect must have reduced the relative horizontal velocity between the wave crest and the platform (by the order of 50% on average) and therefore alleviated the wave-in-deck impact compared with a fixed structure. This feature of the wave-structure interaction may be affected however by the presence of the wind and current, which were not considered in this study.
- The maximum tension in the up-wave tendons usually occurred when the wave crest reached the deck leading edge. Because for the particular model configuration this location coincided with the forward columns, the columns attracted maximum buoyancy at this very instant.
- The maximum tension in the down-wave tendons occurred at about the same time as in the up-wave tendon and exceeded tension in the up-wave tendons in some cases.
- On average, the wave remained in contact with the deck LE over about 13% of wave period, which is about 2.5 s at full scale; during this time the up-wave tendon experienced its peak loading;
- In many cases, the down-wave tendons experienced a rapid reduction in tension even up to zero (slack tendon situation), which also coincided with a large pitch angle in the down-wave direction. This effect is consistent with a large suction force applied to the deck immediately following the impact when the wave crest was still in contact with the deck surface. The slack tendon situations lasted for about 3 – 4 s at full scale; such situations may result in tendon disconnection and, potentially, failure of the platform.
- The wave crest exceedance measured at the deck leading edge was always higher than that at the trailing edge. This indicates the presence of diffraction (distortion of the impacting wave profiled) caused by the deck itself;

Tendon tensions

- Based on several wave events, maximum and minimum tensions experienced by the up-wave and down-wave tendons appeared to correlate with the steepness of the extreme wave. The maximum tension in both up-wave and down-wave tendons increased and the minimum tension in the down-wave tendon reduced as the wave steepness increased.
- The wave events that produced the maximum and minimum tendon tension generally did not correspond to the largest wave crest or the largest wave steepness. This indicated that selection of the design wave, in the same sea state, may require special attention.
- Extreme waves with or even without deck exceedance caused noticeable vertical oscillations of the platform and ringing response in all tendons. The mean magnitude of ringing tensions was found to exceed the initial pretension by 15 % and could elapse 8.2 wave periods after the deck impact.

Impact pressure on the deck underside

- Over all the wave events tested, the maximum impact pressures around the forward and aft columns correlated qualitatively with the maximum tension in the up-wave and down-wave tendons.

Chapter 5: Wave-in-deck loads and response of a TLP model in unidirectional regular waves

This work presented in this chapter is to be submitted for publication in the *Journal of Ships and Offshore Structures*. The paper has been edited for inclusion into this thesis to avoid repetition and to improve readability.

The contributing authors are: Nagi Abdussamie, Yuriy Drobyshevski, Roberto Ojeda, Giles Thomas and Walid Amin.

5.1. Scope

The scope of the present investigation is to examine the global response of a conventional TLP at a model scale of 1:125 due to extreme wave events corresponding to a 10,000-year cyclonic condition. Regular wave tests were conducted in the AMC towing tank. Using data from repeated runs, uncertainty tests of wave elevations, tendon tensions, surge motion and slam pressures at the deck underside were performed. In addition, the commercial CFD code STAR-CCM+ was used to investigate the characteristics of unidirectional regular wave impact on the model. The overset grid technique was used to model rigid body motions. The TLP tendons were modelled using massless spring lines. The numerical results were then validated against the measurements acquired in model tests.

5.2. Experimental investigation

5.2.1. Experimental setup

The TLP model (Figure 5-1) was divided into two parts namely a hull module (columns and pontoons) and a topside deck module. The TLP hull module was represented by four circular columns and four square pontoons; the scaled model dimensions were based on the SNORRE-A TLP. The actual axial compliance of the four SNORRE-A TLP tendons was modelled using a custom stainless steel extension spring with the appropriately scaled stiffness (Figure 5-2). Wave elevations around the TLP model were recorded using five wave probes, denoted as WP (Table 5-1 and Figure 5-3).

Figure 5-1: Photograph showing the TLP model prior to model tests.

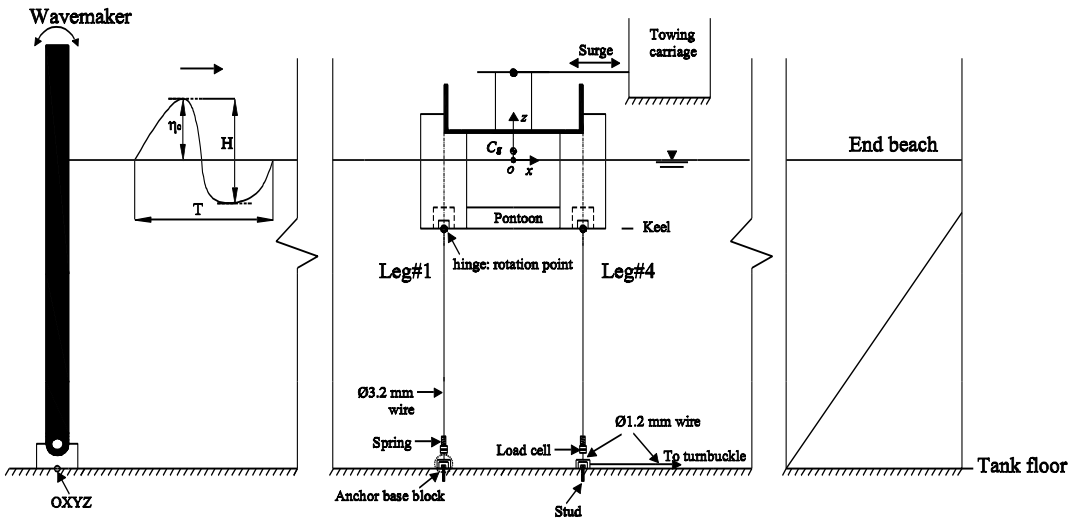

Figure 5-2: Profile view showing sketch definition of wave and the model setup at the AMC towing tank [not to scale]. The adjustment of pretension for each leg was performed through a turnbuckle connected to the tank side.

Table 5-1: Location of wave probes used in experiments with respect to the model's initial centroid.

Wave probe (WP)	Location (x, y) without the model (m)	Location (x, y) with the model (m)
1	(-10.000, 1.275)	(-10.000, 1.275)
2	(-5.000, 1.275)	(-5.000, 1.275)
3	(-1.000, 0.000)	(-1.000, 0.000)
4	(-0.404, 1.200)	(-0.304, 0.000) at deck LE
5	(0.000, 1.200)	(0.304, 0.000) at deck TE

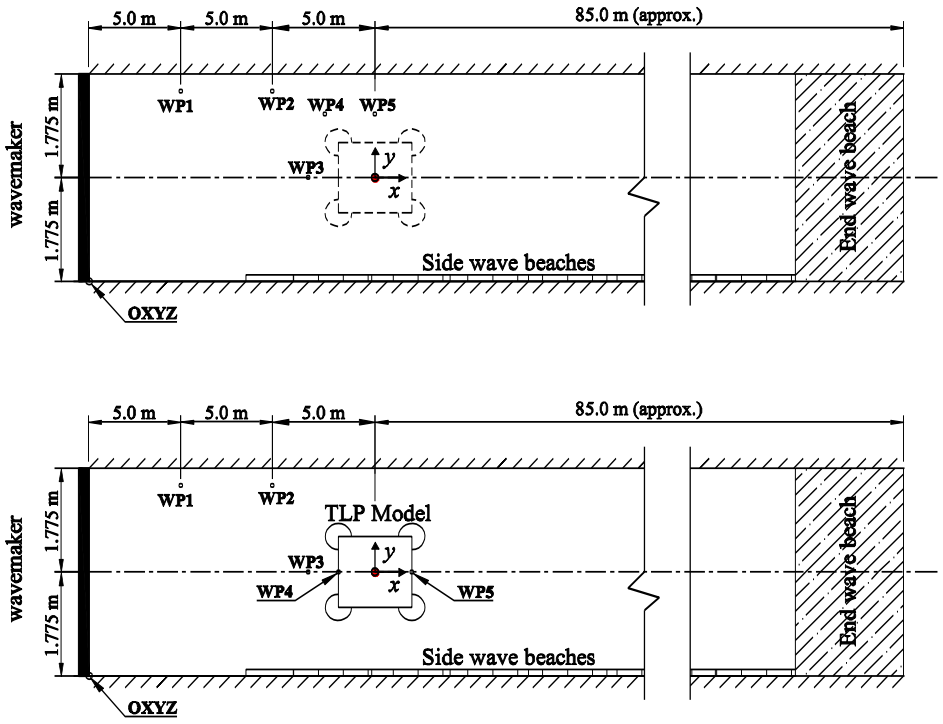

Figure 5-3: Plan view of the AMC towing tank showing the distribution of wave probes (WP): during wave calibration (top); during wave impact tests with the TLP model in-place (bottom) [not to scale].

The model's surge motion was measured by a MagneRule magnetostrictive linear displacement transducer (MLDT). The up-wave and down-wave tendons were instrumented by two FUTEK submersible S-beam junior load cells (Model LSB210), see Figure 5-2. Besides, the underside of the topside deck structure was instrumented with sixteen piezoresistive pressure transducers (denoted by PT#) distributed in *xy* plane to measure localised wave-in-deck slamming pressures (Figure 5-4). The model specifications of the different pressure transducers (approximately 4.0 mm in diameter) and their spatial locations are the same of those reported in Chapter 3. A sampling frequency of 20 kHz was chosen for all channels to capture the short-duration slamming pressures.

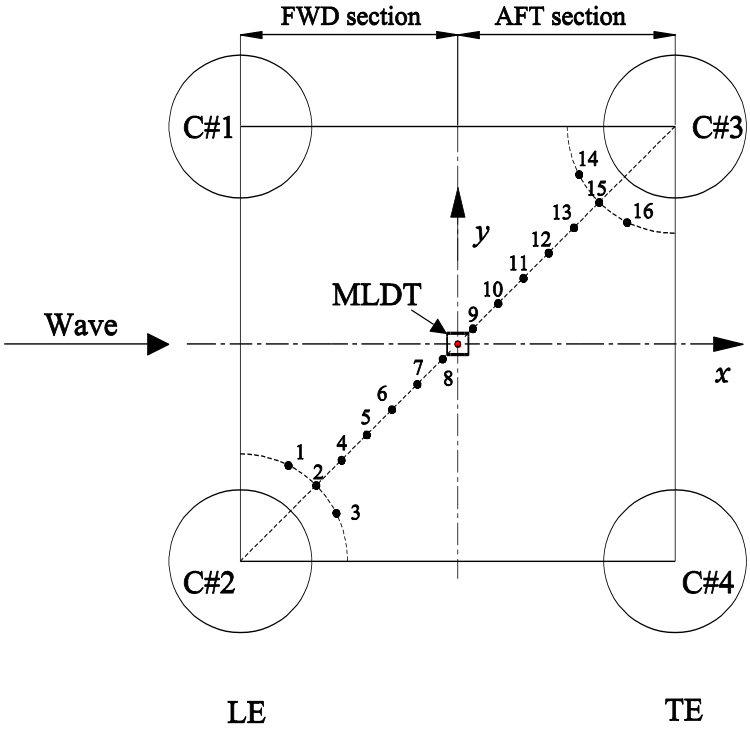

Figure 5-4: Plan view of the deck underside showing the distribution of pressure transducers (PT).

The two cyclonic sea states at the Australian NWS, 100-year and 10,000-year, were represented by several deterministic regular wave trains (Table 5-2). The input wave parameters for 8 wave conditions are summarised in Table 5-3 where λ is the wavelength iteratively estimated from the dispersion relationship.

The wave steepness ($S = H/\lambda$) indicates that all generated wave conditions were within non-breaking wave limits. At zero offset/set-down, test conditions 3 and 8 had a crest height, η_c, exceeding the static deck clearance of 120 mm ($a = a_0 - \eta_c$), as approximated by the Stokes second order.

Table 5-2: Sea states selected.

Sea state	Full scale		Model scale (1:125)	
	H_s (m)	T_p (s)	H_s (mm)	T_p (s)
10,000-year	22.125	17.0	177	1.520
100-year	14.000	14.5	112	1.297

Table 5-3: Input wave parameters for wave conditions.

Condition	H (mm)	T (s)	η_c (mm)	λ (m)	Sea state	H/H_s	S (-)	a (mm)
1	177.0	1.520	95.60	3.61	10,000-yr	1.00	0.049	24.4
2	200.0	1.520	109.10	3.61	10,000-yr	1.13	0.055	10.9
3	220.0	1.520	121.00	3.61	10,000-yr	1.24	0.061	-1.0
4	148.0	1.163	82.20	2.11	Arbitrary	-	0.070	37.8
5	201.6	1.163	115.90	2.11	Arbitrary	-	0.095	4.1
6	112.0	1.297	59.80	2.63	100-yr	1.00	0.043	60.2
7	168.0	1.297	92.50	2.63	100-yr	1.50	0.064	27.5
8	224.0	1.297	127.10	2.63	100-yr	2.00	0.085	-7.1

5.2.2. Uncertainty analyses of experimental data

To ascertain the uncertainty in the model test results, a single wave period associated with condition 2 (H = 200 mm, T = 1.52 s) is discussed below.

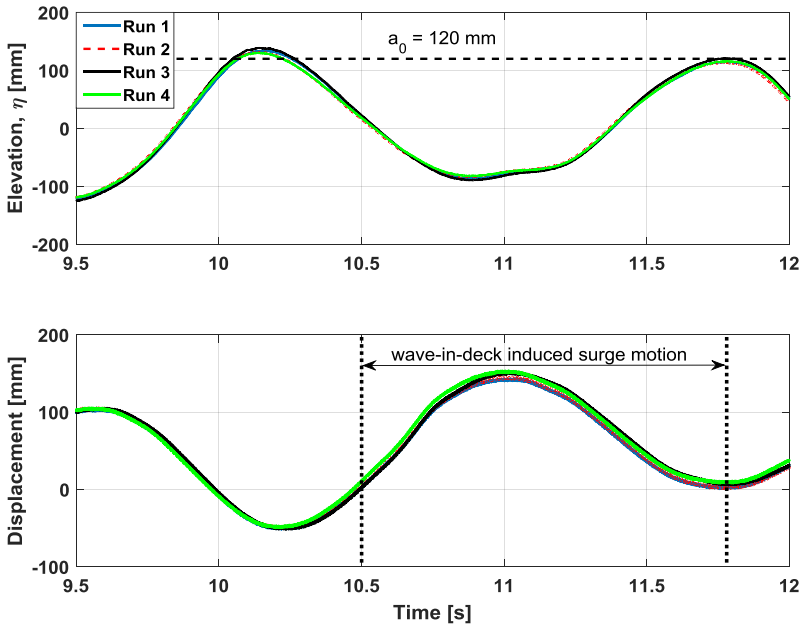

Figure 5-5: Time history of measured wave elevation of a single wave for condition 2 (H = 200 mm, T = 1.52 s) using four repeated runs: wave probe WP3 (top); surge motion (bottom).

Wave elevation measured by WP3 over four repeated runs and the resulting surge motion measured by the MLDT are shown in Figure 5-5, wave elevations measured at the

topside deck LE (WP4) and TE (WP5) are plotted in Figure 5-6. The tendon tensions measured in the up-wave tendon (Leg#1) and down-wave tendon (Leg#4) are given in Figure 5-7. A good repeatability (low variability) can be appreciated for all measured parameters.

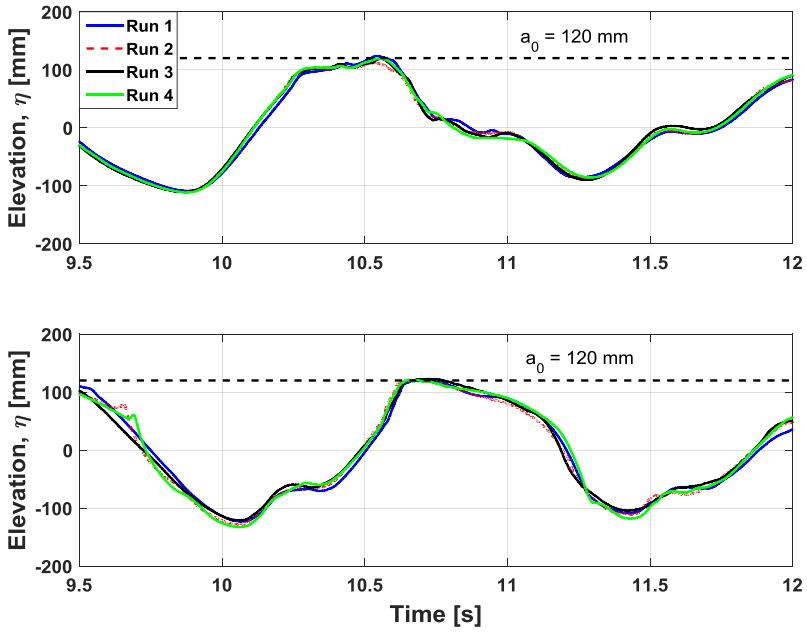

Figure 5-6: Time history of measured wave elevation of a single wave for condition 2 (*H* = 200 mm, *T* = 1.52 s) using four repeated runs: wave probe WP4 at LE (top); wave probe WP5 at TE (bottom).

As a result of deck impact, the model seems to experience a large offset and is then decelerated to its neutral position, i.e., displacement ≈ 0.0 (Figure 5-5). Besides, the up-wave and down-wave tendons were both found to experience high-frequency loadings (Figure 5-7). A significant variability in loading magnitude was observed at a frequency band of 4 – 5 Hz amongst the repeated runs (Figure 5-8), particularly in Leg#1, which demonstrates the nonlinear effects of ringing loads (occurred at the heave natural frequency ≈ 5.0 Hz).

The maximum (+) and minimum (-) values were extracted from the time history of WP3 and MLDT (Table 5-4), and WP4, WP5 and the submersible load cells (Table 5-5). The data variation was assessed by means of standard deviation (σ) and coefficient of variation (CV = σ/mean). The measured wave at WP3 had a mean wave height of 219.60 mm which is approximately 10% larger than the input H = 200 mm used by the wavemaker. All peak values (+) demonstrated good repeatability with a small CV (≤ 5%).

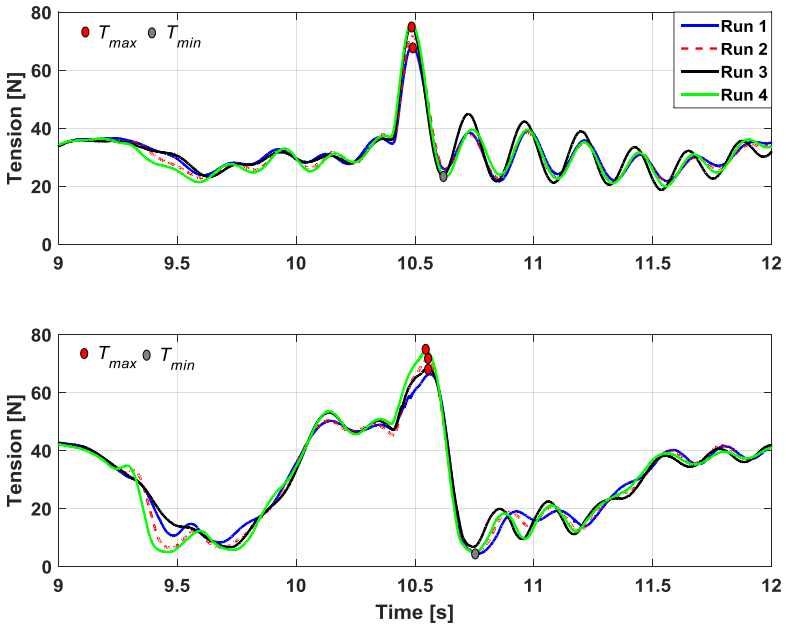

Figure 5-7: Time history of measured tension for condition 2 (*H* = 200 mm, *T* = 1.52 s) using four repeated runs: up-wave tendon (top); down-wave tendon (bottom).

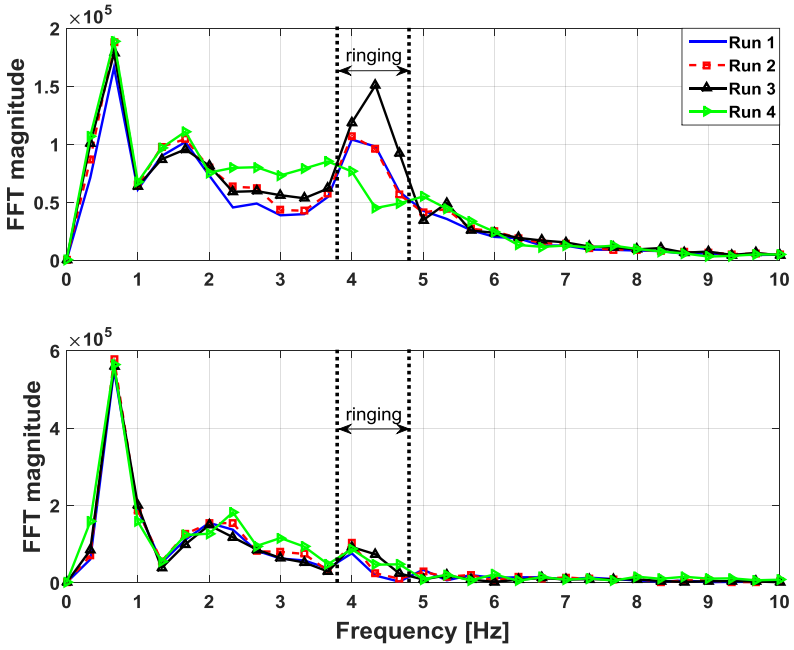

Figure 5-8: FFT results corresponding to the time history of tendon tensions for condition 2 (*H* = 200 mm, *T* = 1.52 s) using four repeated runs: up-wave tendon (top); down-wave tendon (bottom).

While T_{max} was comparable in both legs, T_{min} in Leg#4 was found to be much lower than that measured in Leg#1. The down-wave tendons were found to be susceptible to slack situations (≈ zero tension) caused by a large suction force, as evident from the trough amplitude (-) at TE (WP5) compared to that at LE (WP4), see Table 5-5.

Table 5-4: Variation of measured wave elevations at WP3 and surge motions for condition 2 (H = 200 mm, T = 1.52 s).

Run	WP3 (mm)		Surge (mm)	
	(+)	(-)	(+)	(-)
1	134.60	-86.86	144.00	4.28
2	131.64	-83.82	145.90	4.34
3	139.43	-89.39	152.18	5.15
4	130.53	-82.14	154.14	7.14
Mean	134.05	-85.55	149.06	5.23
σ	3.98	3.22	4.87	1.34
CV	3%	4%	3%	26%

Table 5-5: Variation of measured wave elevations at WP4 and WP5 and tensions for condition 2 (H = 200 mm, T = 1.52 s).

Run#	WP4 (mm)		WP5 (mm)		up-wave tendon (N)		down-wave tendon (N)	
	(+)	(-)	(+)	(-)	T_{max}	T_{min}	T_{max}	T_{min}
1	124.82	-86.77	120.46	-109.54	68.17	21.63	66.32	4.38
2	113.20	-89.00	121.64	-111.66	71.81	22.90	71.49	4.86
3	120.15	-91.06	123.62	-105.06	75.00	21.61	68.42	6.71
4	119.92	-86.82	121.52	-118.81	76.21	23.04	74.28	4.79
Mean	119.52	-88.41	121.81	-111.27	72.80	22.30	70.13	5.19
σ	4.78	2.05	1.32	5.73	3.60	0.78	3.49	1.04
CV	4%	2%	1%	5%	5%	4%	5%	20%

The observed initial pretension for tendons was found to vary and be sensitive to the initial condition for each individual test run in model tests. The measured leg pretension was obtained to be within 91% – 115% of the theoretical tendon pretension of 31.60 N (used in the hereafter CFD tests) (Table 5-6).

Table 5-6: Measured tendon pretension (T_o) and its ratio to the theoretical pretension (31.60 N).

Condition	H (mm)	T (s)	S (-)	up-wave tendon		down-wave tendon	
				T_o (N)	Ratio (-)	T_o (N)	Ratio (-)
1	177.00	1.52	0.049	30.13	0.95	30.94	0.98
2	200.00	1.52	0.055	30.19	0.96	31.34	0.99
3	220.00	1.52	0.061	28.76	0.91	29.65	0.94
4	148.00	1.163	0.070	35.71	1.13	36.49	1.15
5	201.60	1.163	0.095	34.53	1.09	35.47	1.12
6	112.00	1.297	0.043	32.50	1.03	33.29	1.05
7	168.00	1.297	0.064	32.93	1.04	33.57	1.06
8	224.00	1.297	0.085	34.91	1.10	35.59	1.13

The wave-in-deck pressures around the forward and aft columns for the selected wave event are presented in Figure 5-9 and Figure 5-10, respectively. High-frequency components were observed in the pressure signals of PT#3 (5.0 Hz and 385 Hz) and PT#14 (5.0 Hz and 485 Hz) which can be attributed to the vertical vibration (≈ 5.0 Hz) experienced by the model during wave impact.

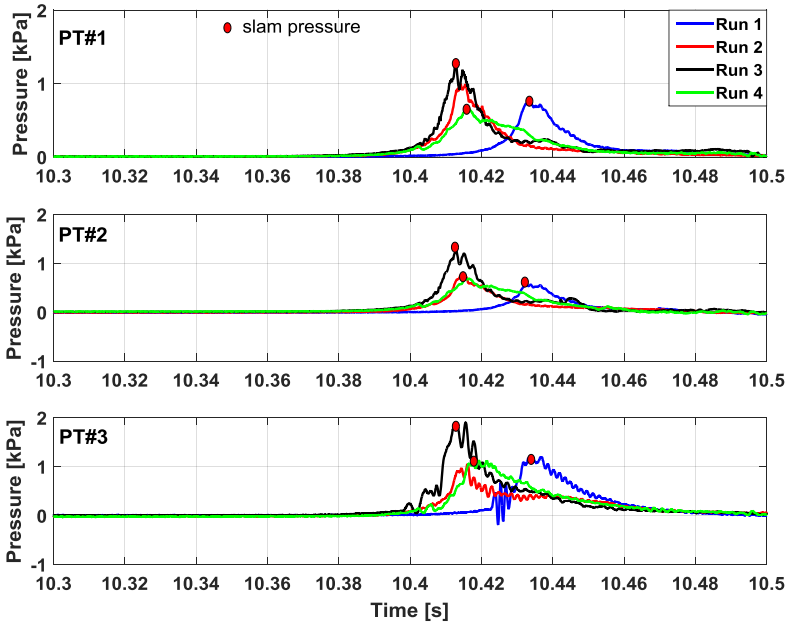

Figure 5-9: Resulting wave-in-deck pressures around the forward column (PT#1 – PT#3) using four repeated runs ($H_{meas.}$ = 219.60 mm, $T_{meas.}$ = 1.52 s).

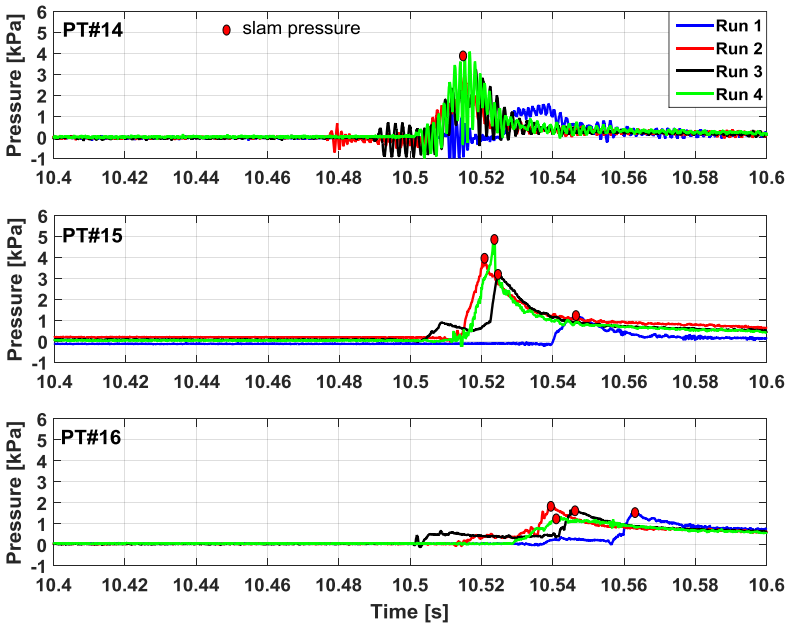

Figure 5-10: Resulting wave-in-deck pressures around the aft column (PT#14 – PT#16) using four repeated runs ($H_{meas.}$ = 219.60 mm, $T_{meas.}$ = 1.52 s).

The measured wave height, $H_{meas.}$, and the corresponding impact (maximum) pressures are summarised in Table 5-7. Using pairwise comparisons between $H_{meas.}$ and the impact pressures, there was no evidence of a correlation between the two parameters. For instance, in run 4 $H_{meas.}$ = 212.67 mm (the lowest wave height) caused the largest impact pressure at PT#14 and PT#15. Figure 5-11 show boxplots of the measured slam pressure values. The square symbol (▪) represents the mean value of peak pressures. The forward section PT#1 – PT#8 captured approximately same slam pressure ≈ 1.25 kPa. The area around the aft columns had larger slam pressures than those measured around the forward columns.

Table 5-7: Variation of measured wave height and impact pressures.

Run#	$H_{meas.}$ (mm)	Forward column (kPa)			Aft column (kPa)		
	WP3	PT#1	PT#2	PT#3	PT#14	PT#15	PT#16
1	221.46	0.75	0.56	1.16	1.45	1.23	1.49
2	215.47	1.00	0.67	1.02	2.95	3.84	1.78
3	228.83	1.24	1.29	1.81	3.13	3.17	1.68
4	212.67	0.65	0.74	1.11	3.96	5.05	1.27
Mean	219.60	0.91	0.82	1.28	2.88	3.32	1.55
σ	6.20	0.23	0.28	0.31	0.91	1.39	0.19
CV	3%	25%	35%	24%	31%	42%	13%

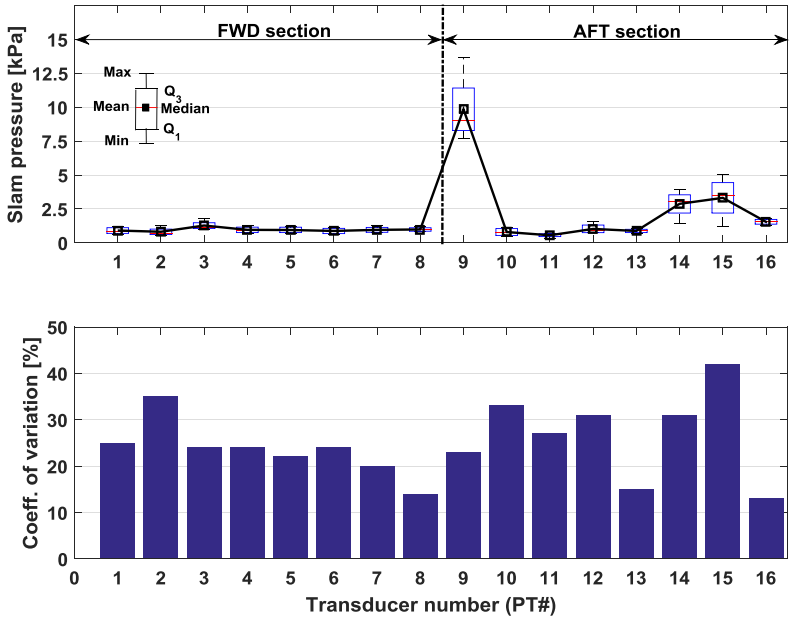

Figure 5-11: Variation of impact pressures measured by sixteen pressure transducers ($H_{meas.}$ = 218.8 mm, $T_{meas.}$ = 1.52 s): boxplots (top); coefficient of variation, CV (bottom).

A very large variation in the magnitude of the impact pressure was obtained of up to 42% at PT#15. It must be noted that PT#9 presents a value completely different from its neighbours (PT#8 and PT#10); such a value can be attributed to a spurious measurement caused by the transducer itself [64].

5.3. Numerical investigation

The commercial Navier-Stokes CFD code STAR-CCM+ (Release 10) developed by CD-adapco was used for simulating the physics of the wave-in-deck problem. Since the CFD results were validated against model test results at a small scale, laminar flow was assumed for all numerical simulations. The VOF model implemented in STAR-CCM+ was used for capturing the interface between two immiscible fluids, herein water and air phases. Both water and air phases were firstly modelled as an incompressible fluid. The air compressibility was then tested by defining the air density and its pressure derivative by means of user-defined field functions. Further theoretical details of the numerical method can be found in the STAR-CCM+ user guide [37].The CFD analyses were conducted as per the following procedure:

1. Wave generation (similar to the wave calibration conducted in model tests) – a numerical wave tank (NWT) or wave generation domain was created without the TLP model being present to investigate wave quality.
2. Wave-structure interaction (similar to the wave impact tests conducted in towing tank) – the TLP model was setup in the domain using overset mesh and subjected to unidirectional regular waves tested in step 1.

5.3.1. Discretisation of the wave generation domain

A 3D trimmed mesh with 1 cell layer into the *y*-direction was generated to investigate the numerical quality of the generated waves. The numerical wave tank used was 22 m long (approximately 6 wavelengths), 0.1 m wide and 2.0 m deep (Figure 5-12). It was divided into three identical zones in the *x*-direction, 2λ long each where λ is the maximum wave length tested (λ = 3.61 m). Wave damping was applied over the last 2λ "damping zone" before the downstream boundary. The method proposed by Choi and Yoon [65] is implemented into STAR-CCM+ for damping the vertical motion of the free surface.

The mesh domain was divided into several parts with different levels of mesh refinement (Table 5-8). Previous work by the authors [23, 39] has identified that

approximately 20 – 30 cells per wave height and 80 cells per wavelength were essential for the accurate prediction of wave propagation in the lower and upper free surface parts.

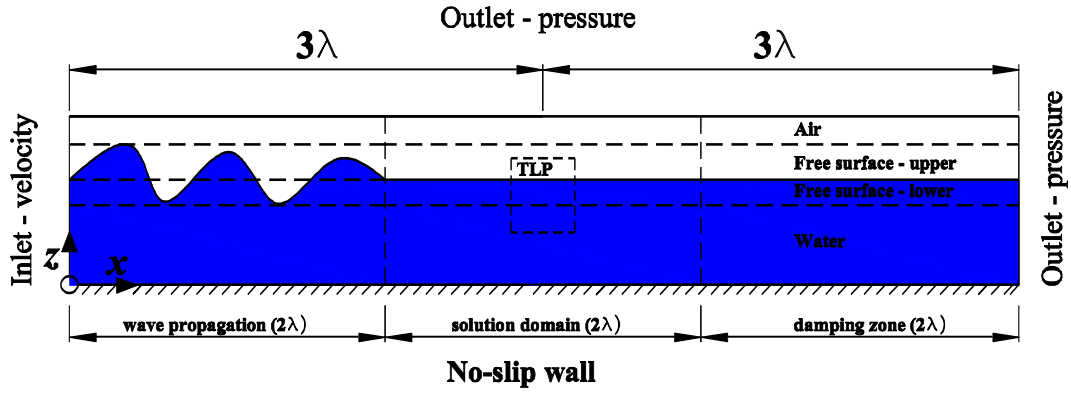

Figure 5-12: Numerical wave tank used in CFD simulations during wave generation without the model being present in the domain.

Table 5-8: Relative mesh size to the base cell size of 0.2 m used for the NWT.

Part	Dimensions: Length × Width × Depth (m)	Relative size (%)		
		dx	*dy*	*dz*
Water	22 × 0.10 × 1.35	100	100	100
Air	22 × 0.10 × 0.30	100	100	100
Free surface	22 × 0.10 × 0.35	12.5	100	3.125
Total cell count	112,420			

5.3.2. Discretisation of the wave-structure interaction domain

The dynamic fluid body interaction (DFBI) model implemented in STAR-CCM+ is capable of computing the 6DOF motions of a rigid body [37]. In this investigation, unidirectional waves allowed the model to be free in only 3DOF motions, namely surge, heave and pitch.

Two regions, a background region and an overset region, with two different coordinate systems, were defined (Table 5-9) as illustrated in Figure 5-13. The overset region, which includes the TLP body, moves with the body over a static background region.

Table 5-9: Domain size for the background and overset regions and overlapping zone.

Dimension	Background region		TLP model		Overset region		Overlapping zone	
	Start	End	Start	End	Start	End	Start	End
Length, *x* (m)	0.0	22.0	10.396	11.204	10.296	11.304	10.196	11.404
Width, *y* (m)	0.0	1.775	0.0	0.404	0.0	0.604	0.0	0.504
Depth, *z* (m)	0.0	2.0	1.195	1.83	1.095	1.93	1.0	2.0

The global coordinate system *OXYZ* of the background region was set to coincide with the right handed-coordinate system used in the model test and during NWT simulations. Each tendon was modelled by a spring line with the axial stiffness of 15.8 N/mm and a

relaxation length of 1193 mm (2 mm initial elongation or equivalently T_o = 31.6 N). The fairlead point was located at z = 1195 mm (column base), and the anchor point was fixed at z = 0.0 (tank floor).

When generating the overset mesh, particular attention should be given to:

1. Minimising errors in the interpolating variables between the overset and background meshes. It is recommended that the same order of magnitude of grid density, in the overlapping zone of the two, is employed.
2. The grid must be finer around the model and the free surface zone to capture relevant free surface details (Table 5-10 and Figure 5-14).

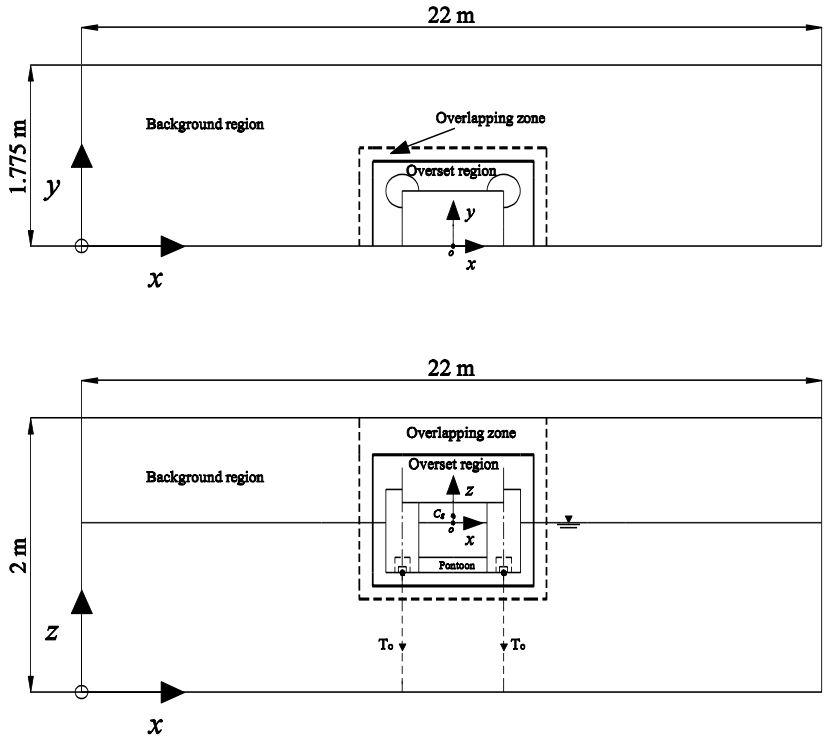

Figure 5-13: A sketch showing overlapping between background and overset regions: plan view (top); side view (bottom) [not to scale].

Table 5-10: Mesh size details in the background and overset regions.

Region	Base cell size	Part	Relative size (%)			Cell count
			dx	*dy*	*dz*	
Background	0.2 m	Water	100	100	100	743,700
		Air	100	100	100	
		Free surface	12.5	100	3.125	
		Overlapping	12.5	12.5	3.125	
Overset	0.1 m	Water	100	100	100	1.26×10^6
		Air	100	100	100	
		Free surface	25	100	6.25	
		Overlapping	25	25	6.25	
		Total				2.00×10^6

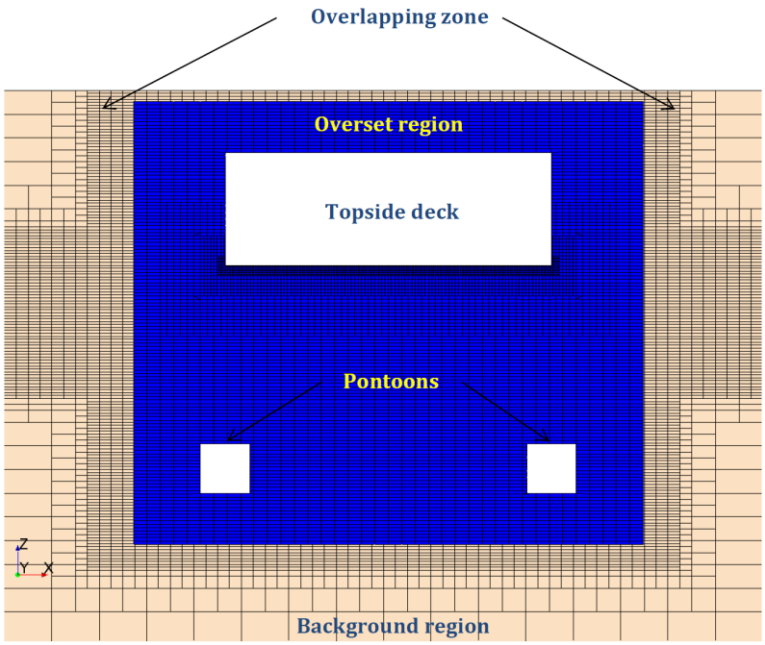

Figure 5-14: Snapshot at *xz* plane showing mesh distribution near the TLP model.

5.3.3. Boundary and initial conditions

An incoming wave with appropriate height and wave period was specified using the Stokes fifth order at the inflow domain boundary (x = 0.0), see Figure 5-12. Hydrostatic pressure boundary condition was assigned at the top of the tank and its end on the right side. No-slip boundary condition was used on the tank bottom (z = 0), tank side (y = 1.775 m) and the TLP model boundary surfaces. Whilst the other side of the domain (y = 0) was set with a symmetry boundary condition.

At time = 0.0, the wave field was initialised such that the wave profile was fully developed in the "wave propagation" zone; from x = 0 to x = 2λ (Figure 5-12). This minimised the time required for incoming waves to reach x = 10.8 m (model's centroid) in the wave-structure interaction simulations.

As the body is assumed to be rigid, elastic deformations effects were not considered.

5.3.4. Prediction of wave-in-deck slam pressures

To capture slam pressure distribution at the deck underside, different levels of mesh refinement were investigated (Table 5-11 and Figure 5-15). The diameter of transducer tip ($D_{trans.}$ ≈ 4 mm) was divided into a number of 2D (surface) cells. The local mesh refinement led to a dramatically increase in the total cell count.

Table 5-11: Mesh refinement at the deck underside relative to the base cell size of 0.10 m.

Level	Relative size (%)	Absolute size (mm)	$D_{trans.}$/absolute size (-)	Total cell count
1	3.12500	3.12500	1.28	2.00×10^6
2	1.56250	1.56250	2.56	2.37×10^6
3	0.78125	0.78125	5.12	4.10×10^6

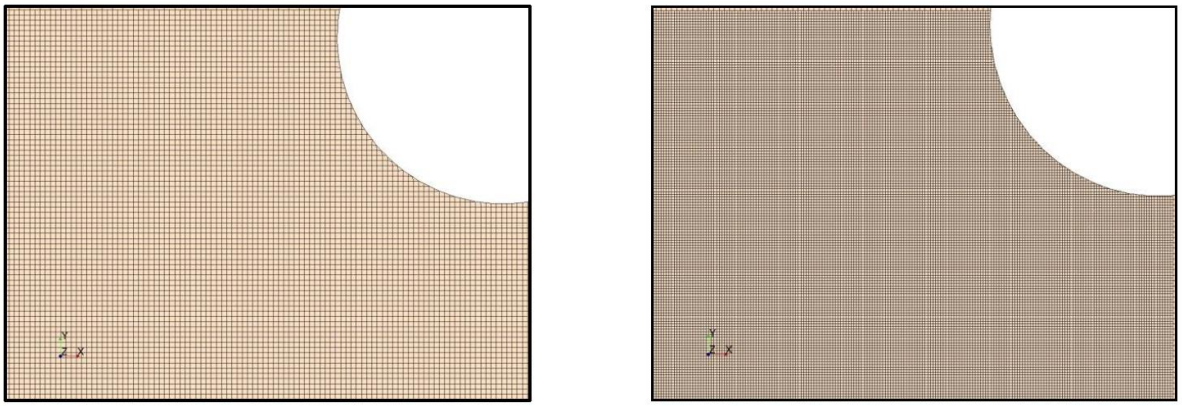

Figure 5-15: Snapshots showing the local refinement of surface mesh at the deck underside near the aft column: reference mesh, level 1 (left); fine mesh, level 2 (right).

5.3.5. Solution settings

Time step of 0.001 s and 5 iterations per time step were adequate to maintain optimal HRIC solution [39]. The second order discretisation of unsteady terms in momentum equations and HRIC scheme for the solution of the volume fraction equations was adopted. The pressure-velocity coupling was performed by the SIMPLE (Semi-Implicit Method for Pressure-Linked Equations) algorithm.

5.3.6. Assessment of CFD results

Wave quality

The accuracy of CFD wave elevations was assessed on the basis of the input wave height. Figure 5-16 presents the computed wave height averaged over several wave cycles for a simulation time of 20.0 s. The computed wave heights, at the CFD area of interest, x = 9.8 m (WP3) and x = 10.8 m (WP5), were found to be within 93% – 97% of the input wave height (H_{input}) indicating good accuracy and deemed to be acceptable.

The efficiency of the damping zone was assessed by monitoring the wave elevation along the domain, at a volume fraction of water = 0.5, obtained at different instances of time (Figure 5-17). It is difficult to simulate waves with zero transport losses numerically due to relaxed spatial and temporal discretisation [23]. Also, there is a tendency of NWT to build a

phase difference of numerical wave with the theoretical wave which is generally noticed far away from the inlet boundary condition (Figure 5-17).

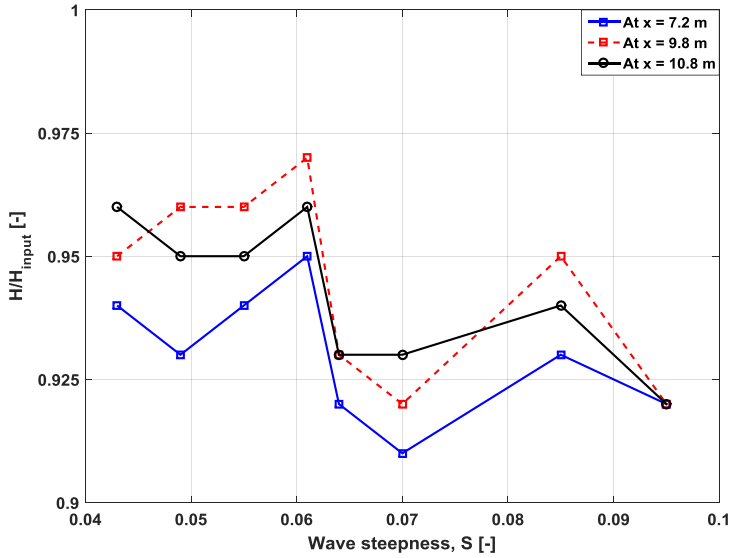

Figure 5-16: Results of wave height (H) predicted by CFD to H_{input} versus wave steepness at different locations along the computational domain. Mesh size: $\lambda/dx > 20$ and $H_{input}/dz > 80$.

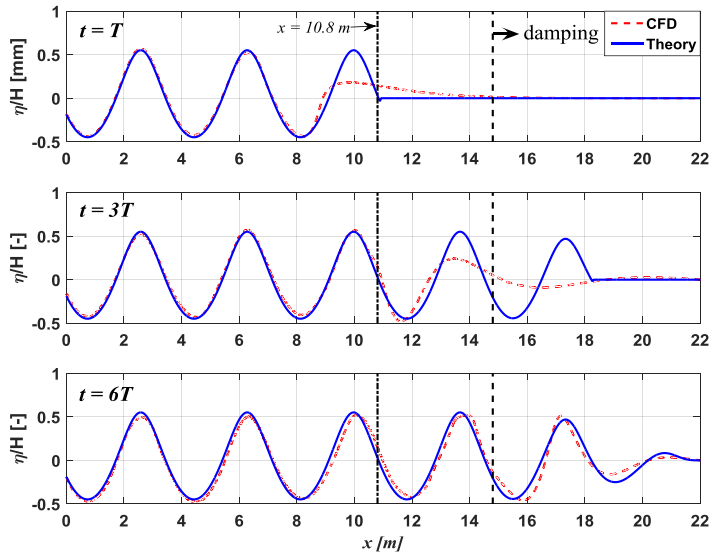

Figure 5-17: Comparisons between CFD and theoretical solutions of wave elevation along the computational domain for condition 3 (H = 220 mm, T = 1.52 s, S = 0.061): at time = one wave period (top); at time = three wave periods (middle); at time = six wave periods (bottom).

Mesh density

The maximum wave-in-deck pressure caused by the steepest wave condition (condition 5: H = 201.6 mm, T = 1.163 s) was utilised for sensitivity analyses due to local mesh density on the deck underside (Table 5-11). By referring to Figure 5-18 the effect of mesh density was noticeable when results of level 2 (fine mesh) and level 3 (finer mesh) were compared with

those of level 1 (reference mesh), refer to Table 5-12 for quantitative comparisons. For wave impacts 3 – 5, the use of level 3 indicated the effect of mesh local refinement on the magnitude of maximum impact pressure; much larger pressure values were computed using the finest mesh level examined in this study. Additional results of CFD mesh studies can be found in Appendix D for the same TLP model configuration, except the model was fixed in place.

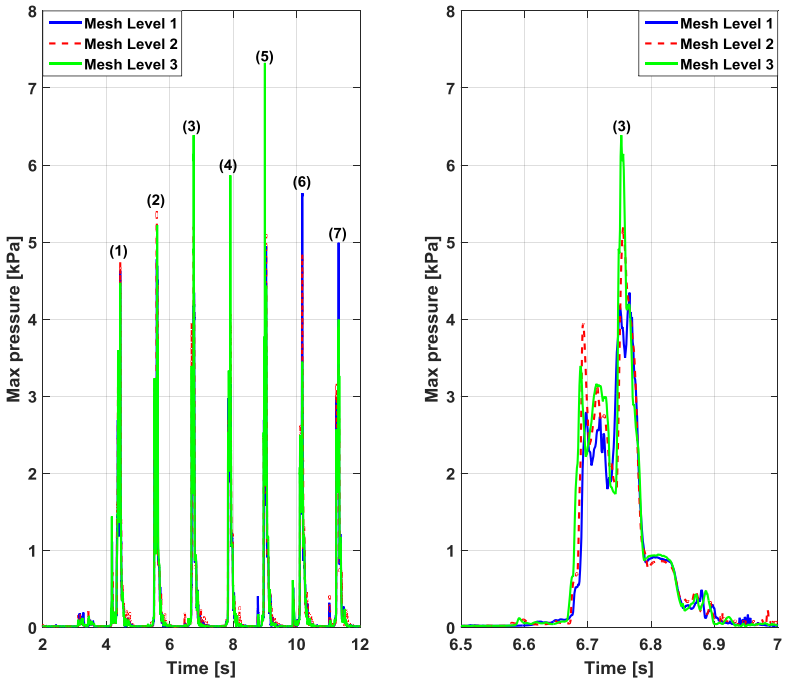

Figure 5-18: Results of sensitivity analysis of maximum pressure at the deck underside due to mesh density for condition 5 (H = 201.6 mm, T = 1.163 s, S = 0.095): time history of multiple wave-in-deck impact events (left); time history of a single wave-in-deck impact event (right).

Table 5-12: The effect of mesh density at the deck underside on the maximum slam pressure for condition 5 (H = 201.6 mm, T = 1.163 s, S = 0.095). Impact numbers are shown in Figure 5-18.

Wave impact	Peak pressure (kPa)			Peak pressure ratio	
	Level 1	Level 2	Level 3	Level 2/Level 1	Level 3/Level 1
1	4.63	4.73	4.47	102%	97%
2	4.78	5.44	5.22	114%	109%
3	4.34	5.20	6.39	120%	147%
4	3.16	4.06	5.87	129%	186%
5	4.93	5.05	7.33	102%	149%
6	5.64	4.85	3.45	86%	61%
7	4.99	3.83	4.00	77%	80%

Air compressibility

The effect of air compressibility was tested by comparing results of the maximum wave-in-deck pressure obtained using compressible air phase with those predicted using incompressible air. Both numerical tests were conducted using mesh level 3 for condition 5 (Figure 5-19). Air density and its pressure derivative were defined by means of user-defined field functions derived from the following equations [37]:

$$\rho_{air} = \rho'_{air} + \frac{p}{C_{air}^2} \tag{5-1}$$

$$\frac{d\rho_{air}}{dp} = \frac{1}{C_{air}^2} \tag{5-2}$$

where ρ'_{air} = 1.18415 kg/m^3 is the reference air density (incompressible air), C = 331 m/s is the sound speed in air, and p is pressure. At every time step, p value is obtained for each node throughout the numerical domain by solving the Poisson equation.

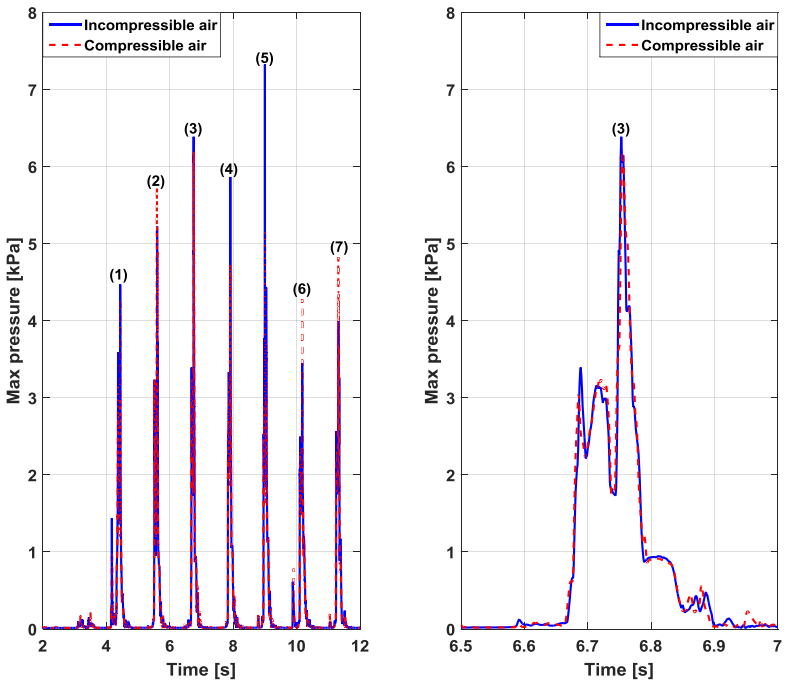

Figure 5-19: Results of sensitivity analysis of maximum pressure at the deck underside due to air compressibility using mesh level 3 for condition 5 (*H* = 201.6 mm, *T* = 1.163 s, *S* = 0.095): time history of multiple wave-in-deck impact events (left); time history of a single wave-in-deck impact event (right).

The air compressibility had also an inconsistent effect on the slam pressure (the magnitude of maximum impact pressure may not necessarily increase for all consecutive deck impacts); refer to Table 5-13 for quantitative comparisons. Additional CFD results detailing the effect of air compressibility can be found in Appendix D.

Table 5-13: The effect of air compressibility on the magnitude of maximum slam pressure acting on the deck underside using mesh level 3 for condition 5 (H = 201.6 mm, T = 1.163 s, S = 0.095). Impact numbers are shown in Figure 5-19.

Wave impact	Peak pressure (kPa)		Peak pressure ratio
	Incompressible air	Compressible air	Comp./Incomp.
1	4.47	4.28	96%
2	5.22	5.69	109%
3	6.39	6.17	97%
4	5.87	4.72	80%
5	7.33	5.18	71%
6	3.45	4.28	124%
7	4.00	4.79	120%

5.4. Comparison of experimental and CFD results

Using still-water simulations, the model was initialised by prescribed translational or angular velocity along the DOF of interest. An arbitrary selection of 0.3 m/s and 0.3 rad/s, was performed for modelling the surge/heave and pitch CFD free decay tests, respectively.
Table 5-14 summarises the results of these decay tests in the surge, heave and pitch DOF. Figure 5-20 shows the time traces of surge decay test and the corresponding FFT results.

Good agreement was achieved between the CFD and model tests, although damping ratios differed which can be attributed to the far-field boundary effects as the domain length was shorter than the physical tank. In other words, the effect of waves generated by radiation in the NWT was different from those generated in the towing tank.

Table 5-14: Damped natural periods.

Motion	Experiment (s)	CFD (s)	CFD/Experiment (-)
Surge	5.660	5.61	0.99
Heave	0.225	0.21	0.93
Pitch	0.222	0.21	0.95

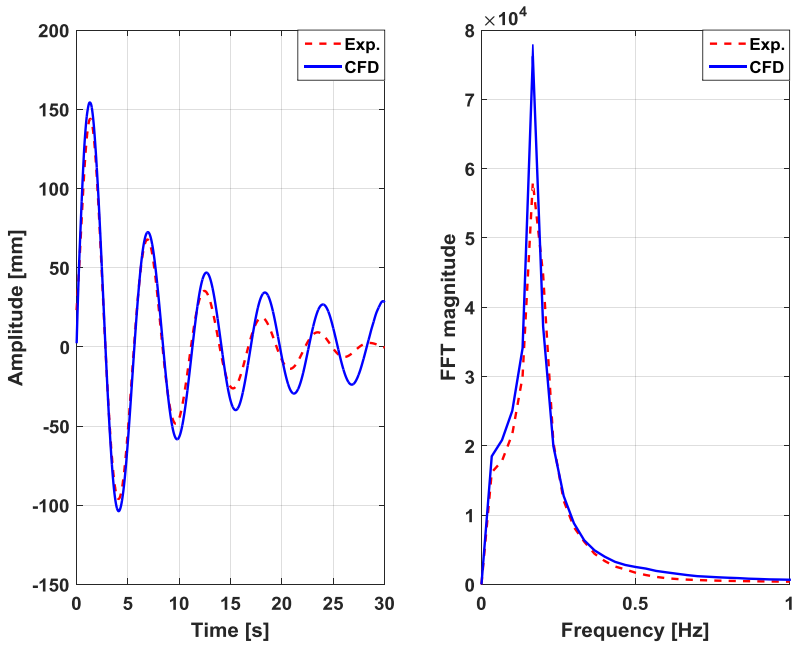

Figure 5-20: Free decay test results of CFD and experiments for surge motion: time history (left); FFT results (right).

5.4.1. Results of global response

Time histories of surge motions and tendon tensions for test conditions 2 and 3 are shown in Figure 5-21 and Figure 5-22, respectively. Apart from the first impact, which caused by the transient start-up condition of wavemaker in model tests, the magnitude of surge motion and tension in both legs were well predicted by CFD simulations.

With the assumption of zero pitch rotational motion, the platform set-down (Z) was estimated from the time history of the measured surge motion, $X(t)$, as $Z(t) = \mathrm{L_o} - \sqrt{(\mathrm{L_o^2} - X^2)}$ [66], L_o = 1195 mm (the change in the tendon length due to its elastic stretch was neglected). The estimated set-down was then compared with the heave motion predicted by CFD (Figure 5-23). Good agreement was achieved between the estimated and computed platform set-down for both conditions 2 and 3 indicating that the contribution of pitch motion in the magnitude of set-down was minimal.

T_{max} and T_{min} in the up-wave and down-wave tendons are summarised in Table 5-15 for all conditions. Figure 5-24 shows the maximum surge amplitude (in positive x-direction) and the maximum and minimum tensions as a function of wave steepness (S).

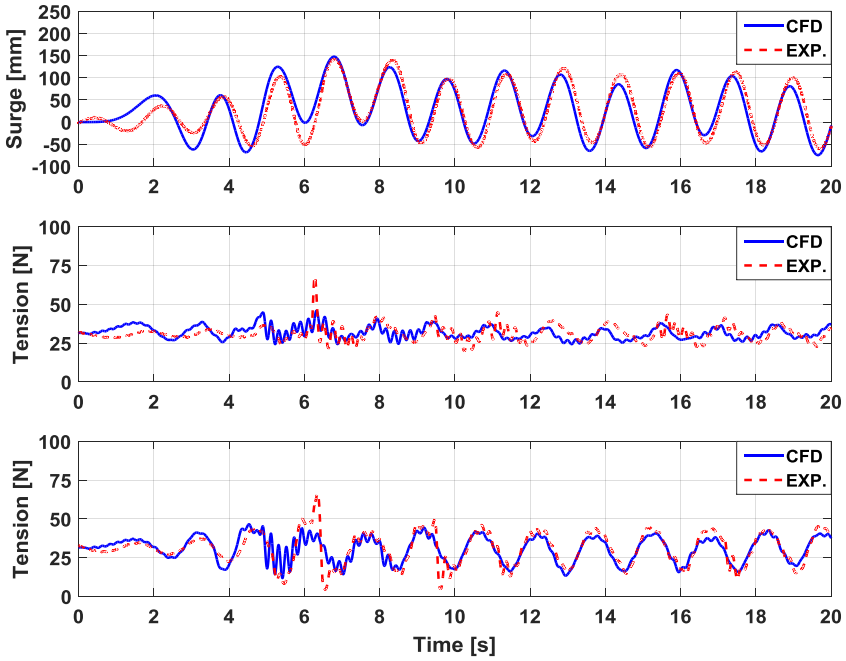

Figure 5-21: Comparison of CFD and experimental results for condition 2 (H = 200 mm, T = 1.52 s): surge motion (top); tension in the up-wave tendon (middle); tension in the down-wave tendon (bottom).

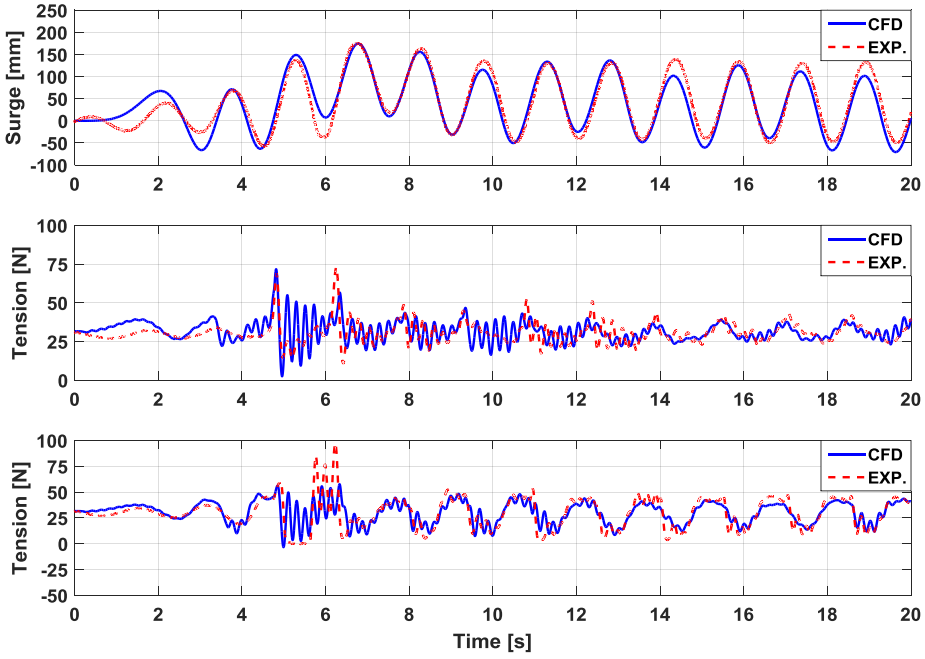

Figure 5-22: Comparison of CFD and experimental results for condition 3 (H = 220 mm, T = 1.52 s): surge motion (top); tension in the up-wave tendon (middle); tension in the down-wave tendon (bottom).

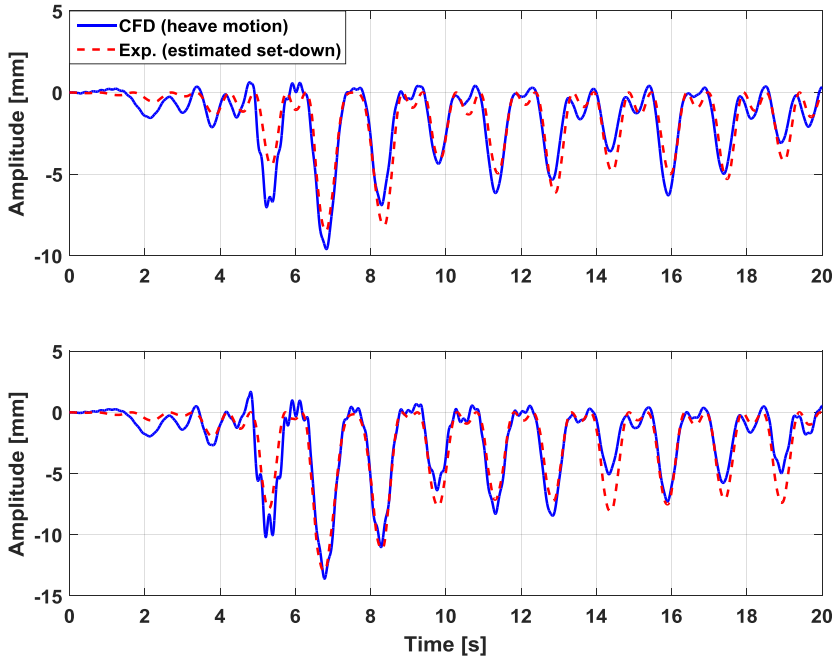

Figure 5-23: Time history of heave motion predicted by CFD and the estimated set-down by measurements: for condition 2 (top); for condition 3 (bottom).

For condition 5 (S = 0.095) and condition 8 (S = 0.085) CFD solutions were found to over-predict the minimum tension in the up-wave tendon. Such a discrepancy can be attributed to the sensitivity of load cells to zero/negative force as well as to the nonlinear response of spring line being different in CFD compared to the model tests. Furthermore, the initial pretension used in CFD models was set as constant (T_o = 31.6 N). This was not the case in model tests, where the measured initial pretension was found to vary and be sensitive to the initial condition for each individual test run. The measured leg pretension was obtained to be within 91% – 115% of the computed tendon pretension, see Table 5-6.

Table 5-15: T_{max} and T_{min} in the tendons (average measured values).

Condition	S (-)	up-wave tendon (N)				down-wave tendon (N)			
		T_{max}		T_{min}		T_{max}		T_{min}	
		CFD	Exp.	CFD	Exp.	CFD	Exp.	CFD	Exp.
1	0.049	36.39	37.97	27.19	25.72	39.13	42.40	19.48	19.00
2	0.055	38.05	40.44	26.09	23.24	41.19	44.04	16.35	11.65
3	0.061	42.33	42.80	22.40	22.85	44.77	45.89	10.44	9.60
4	0.07	37.06	41.30	26.73	31.04	71.61	79.20	39.13	47.85
5	0.095	57.90	63.23	1.27	9.54	61.50	67.16	0.00	0.00
6	0.043	32.88	36.57	28.80	30.76	37.01	48.39	35.50	41.85
7	0.064	36.20	41.33	27.27	28.35	39.91	49.71	18.03	13.08
8	0.085	67.07	73.17	1.89	9.78	70.07	83.54	0.00	0.00

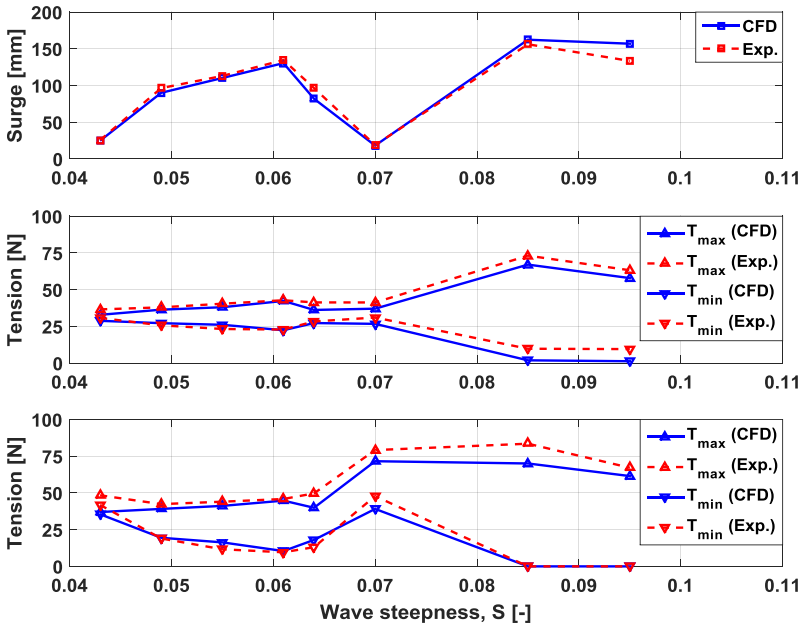

Figure 5-24: Comparison of CFD and experimental results: maximum amplitude of surge motion (top); maximum and minimum tension (T_{max} and T_{min}) in the up-wave tendon, Leg#1 (middle); maximum and minimum tension (T_{max} and T_{min}) in the down-wave tendon, Leg#4 (bottom).

5.4.2. Wave-in-deck impact events

During model experiments, the wave-in-deck impact events were identified through pressure measurements and using high-speed cameras. It was observed that trapped waves between the forward and aft columns seem to be heightened due to wave upwelling and diffraction and hence caused local impacts at the deck underside. The minimum dynamic air gap due to the estimated platform set-down (Z) was given as $a_n = a_0 - (\eta_{meas.} - Z)$, $\eta_{meas.}$ is the crest height at WP3. Table 5-16 summarises the estimated values of a_n compared with those obtained at zero offset/set-down using input wave parameters ($a = a_0 - \eta_c$). The platform surge motion and set-down resulted in additional wave-in-deck impact events including conditions 1, 2 and 5.

Table 5-16: Effect of platform set-down on the dynamic air gap.

Condition	Input parameters			Measurements (averaged)			
	S (-)	η_c (mm)	a (mm)	X (mm)	$\eta_{meas.}$ (mm)	Z (mm)	a_n (mm)
1	0.049	95.60	24.40	47.97	117.72	-0.96	1.32
2	0.055	109.10	10.90	98.94	122.18	-4.10	-6.28
3	0.061	121.00	-1.00	115.20	143.42	-5.57	-28.99
4	0.070	82.20	37.80	140.47	96.25	-8.28	15.47
5	0.095	115.90	4.10	100.05	115.01	-4.20	0.79
6	0.043	59.80	60.20	80.05	81.26	-2.68	36.06
7	0.064	92.50	27.50	154.37	106.13	-10.01	3.86
8	0.085	127.10	-7.10	134.27	116.58	-7.57	-4.15

CFD models enabled the wave impact force component acting on the topside deck (wave-in-deck force) to be isolated from the total hydrodynamic wave force acting on the TLP model.

In most cases, the magnitude of the horizontal wave-in-deck forces (F_x) was found to be insignificant, whereas the vertical wave-in-deck forces (F_z) were found to largely affect the global response of the TLP model.

The dynamic tensions (T_o was subtracted from the time histories) in the up-wave and down-wave tendons were analysed along with F_z time history. Figure 5-25 shows CFD results of F_z time history for conditions 3, 5 and 8.

Tendon slack situations were denoted by a dashed line (force = -31.60 N). The aft tendons were found to experience slackness following the deck impact in many wave cycles. The downward component of F_z which was found to be approximately synchronised with the minimum tendon tensions caused such slack situations.

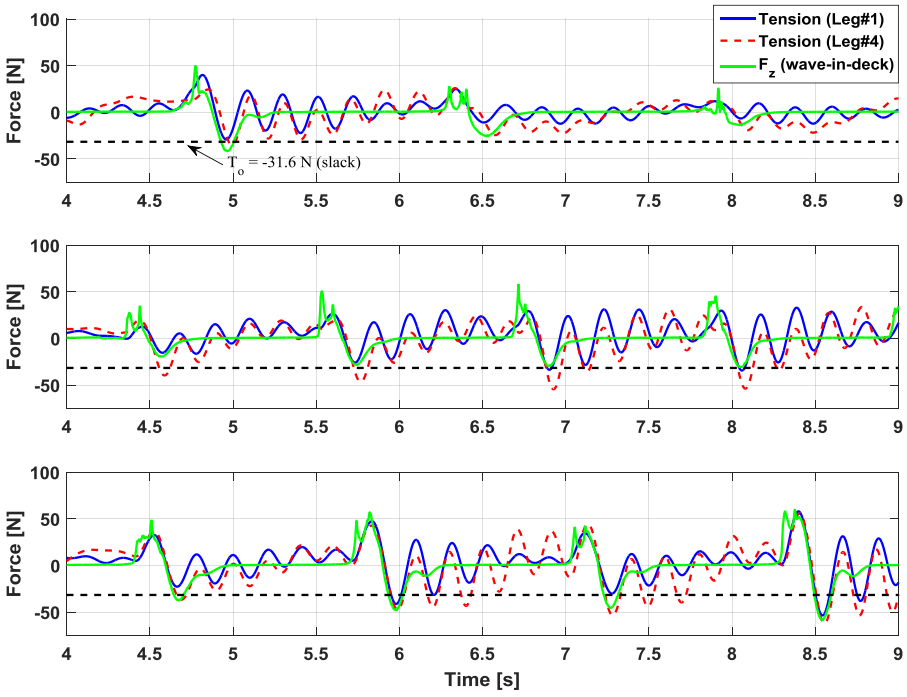

Figure 5-25: Time history of CFD results for tendon tensions in the up-wave and down-wave tendons and the simultaneous vertical wave-in-deck force, F_z: for condition 3 (top); for condition 5 (middle); for condition 8 (bottom).

Time history of a single wave-in-deck impact event for condition 5 is presented in Figure 5-26 with four phases defined as follows:

- Phase I (platform response: time = 5.0 s – 5.5 s) – it preceded the wave impact on the deck underside, the variation in tension could be caused by wave impact on the forward columns (including overtopping) and/or the ringing response caused by the previous deck impact, F_z = 0.0.
- Phase II (water entry: time = 5.5 s – 5.655 s) – two deck slams were identified: the first was at time = 5.534 s (F_z = 50.77 N) and the second occurred at time = 5.60 s (F_z = 35.89 N), the second slam was shorter than the first one.
- Phase III (water exit: time = 5.655 s – 6.0 s) – water detached from the deck underside started at time = 5.655 s, F_z was minimum (F_z = -28.37 N) and slackness occurred in the down-wave tendon, the phase completed at time = 6.0 s.
- Phase IV (platform response: time = 6.0 s – 6.5 s) – ringing response were pronounced in both tendons, F_z = 0.0.

Figure 5-27 shows the interaction between a large wave and the TLP model using snapshots at different time frames for condition 5.

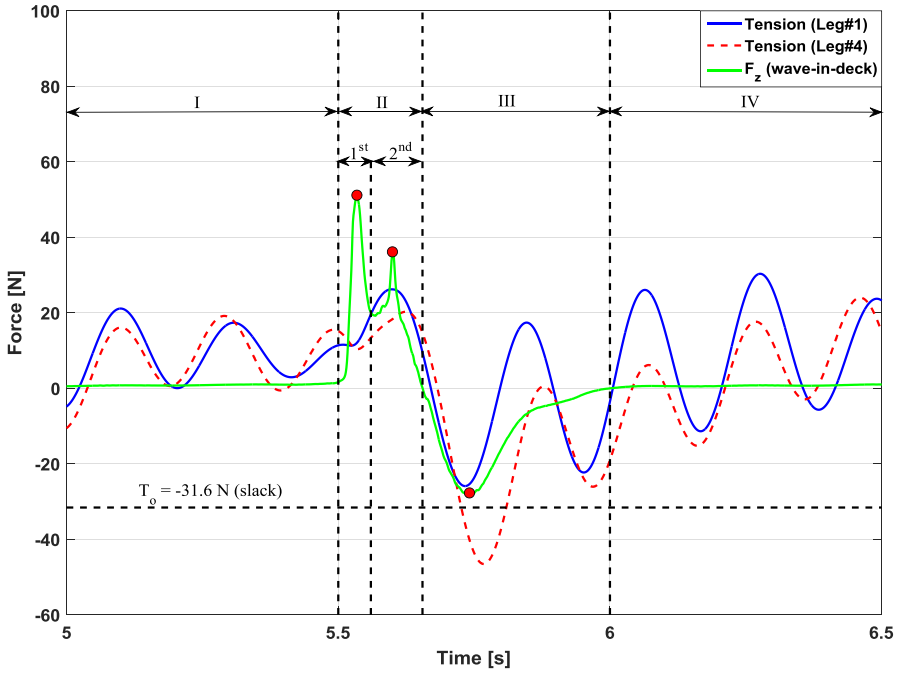

Figure 5-26: Time history of CFD results for a single wave-in-deck event and the associated tendon tensions in the up-wave and down-wave tendons for condition 5: H = 201.6 mm, T = 1. 163 s.

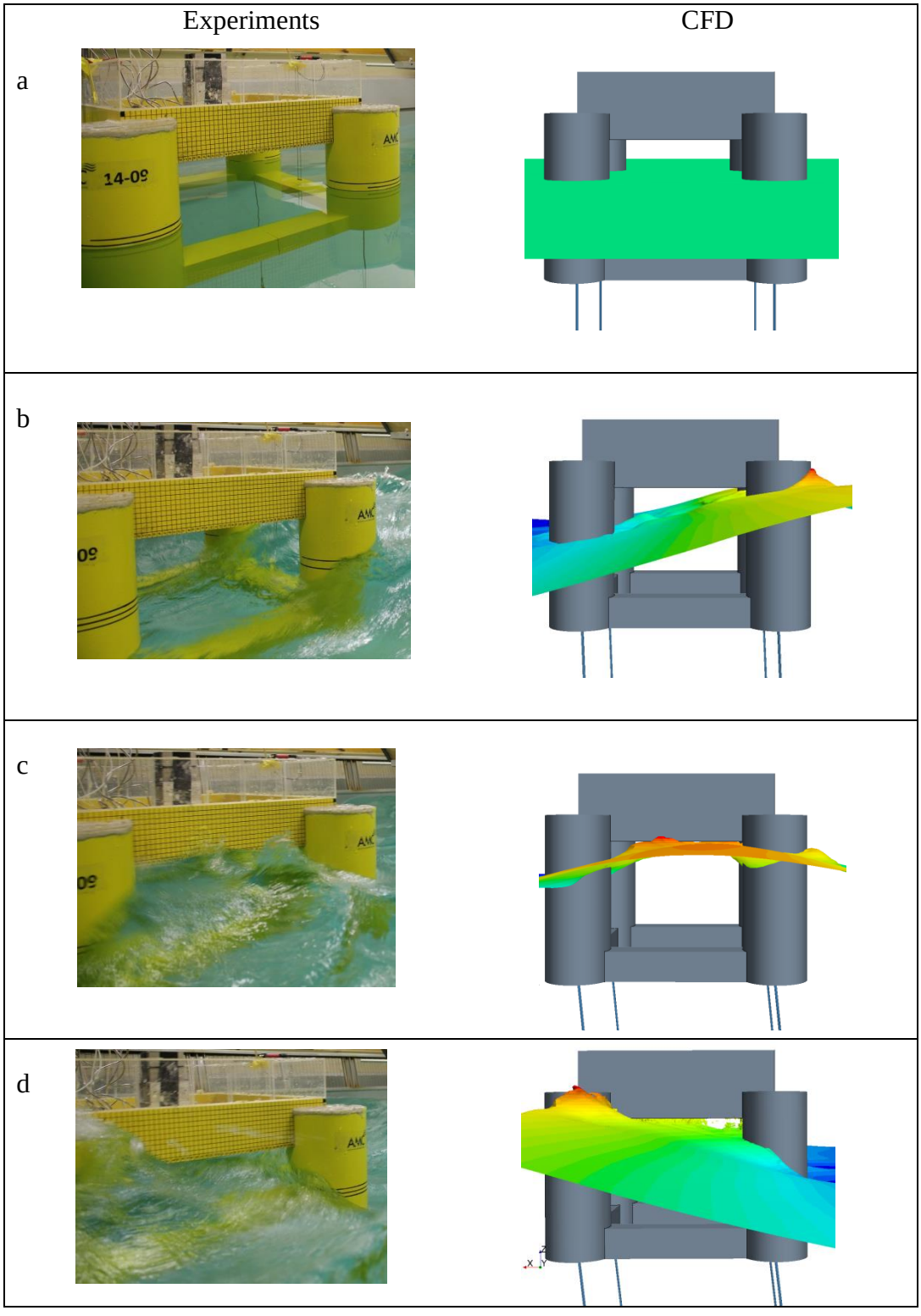

Figure 5-27: Snapshots at different time instances showing an extreme wave impact on the TLP model at the towing tank (left) and using CFD simulations (right): (a) no wave (still-water) condition; (b) wave run-up on the forward columns; (c) wave impact on the deck underside; (d) wave impact on the aft section of deck underside and water overtopping on the aft columns. Condition 5 (H = 201.6 mm, T = 1.163 s).

The CFD simulations of wave-in-deck pressures were conducted using mesh level 3 and the compressible air model. The single wave-in-deck impact event discussed above for condition 5 was selected for further analysis. The maximum pressure caused by the wave impact throughout the deck underside was captured at each time step (Figure 5-28). The pressure signal is denoted by four peaks (a) – (d). The first slam obtained in F_z (Figure 5-26) was found to coincide in the time interval (a) – (b), whereas the second slam occurred in the time interval (c) – (d). Figure 5-29 shows snapshots of pressure contours at the deck underside corresponding to the different time instances (a) – (d) where half of the deck underside and columns# 1 and 3 are only shown. The magnitude of the impact pressure caused by the first slam (a – b) was smaller but acting on a larger area than that caused by the second slam (c – d). By analysing the volume fraction of water during these time instances, the deck surface area subjected to wave slams was found to contain a mixture of air and water (the water content was not 100%, i.e., water volume fraction ≠ 1.0). At the instant (d), for example, the area around the aft column experienced a maximum pressure of approximately 4885 Pa with a volume fraction of water almost 65% (35% air).

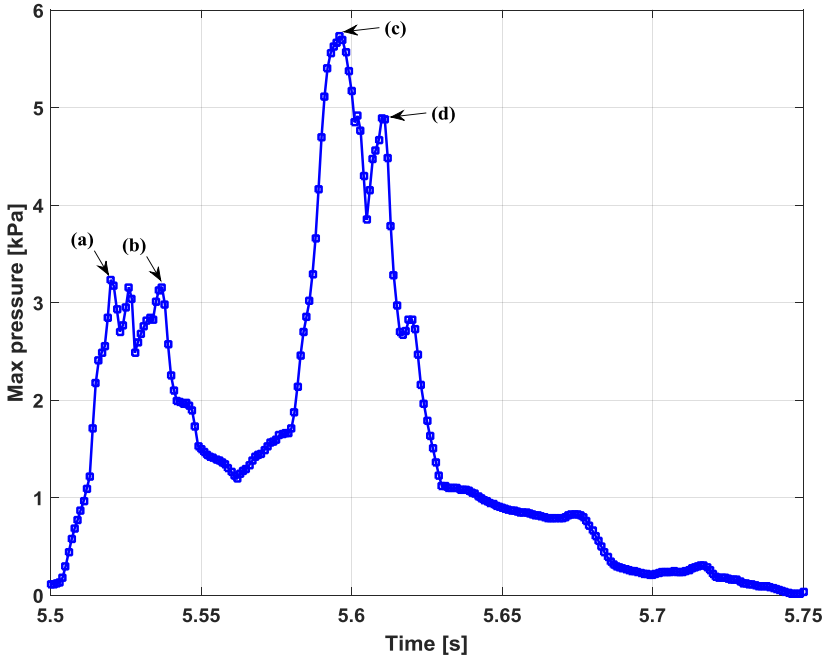

Figure 5-28: Time history of maximum pressure at the deck underside computed using mesh level 3 with compressible air for condition 5 (H = 201.6 mm, T = 1.163 s).

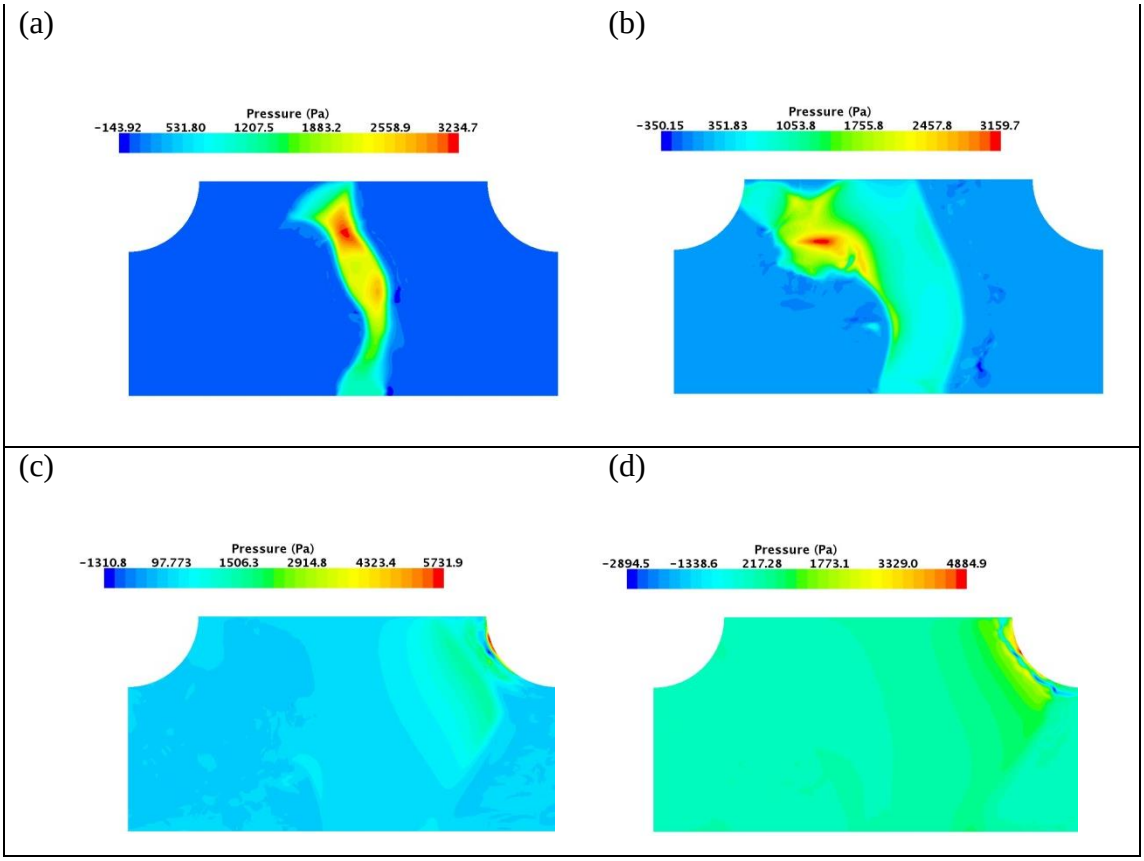

Figure 5-29: Pressure contours at the deck underside for condition 5 (*H* = 201.6 mm, *T* = 1.163 s) using mesh level 3 and compressible air. Time instances (a) – (d) are shown in Figure 5-28.

As the area around the aft column was found to experience large slam pressures, a comparison of measured and computed impact pressure at a discrete point representing the central location of pressure transducer PT#16 was made (Figure 5-30). CFD predictions of maximum pressure were found to favourably agree to the maximum pressure measured over repeated runs. As previously discussed, pressure measurements due to wave impact at discrete points were found to be extremely variable. Another complexity of model tests lies in the effect that regular waves often fail to reach the steady state and hence the wave-in-deck slam pressures vary in time and space. On the other hand, regular waves generated by CFD models demonstrated improved stability.

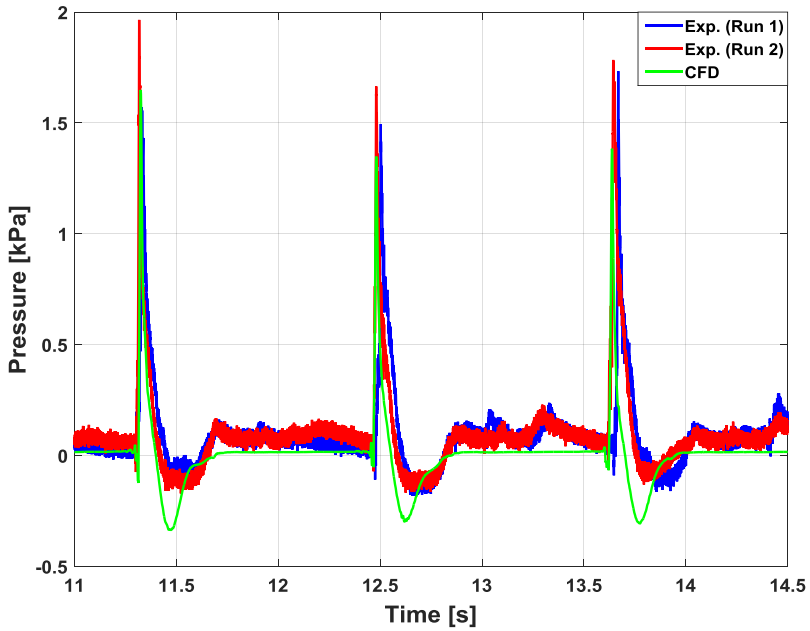

Figure 5-30: Time history of wave-in-deck pressure at PT#16 obtained by experiments and CFD for Condition 5 (H = 201.6 mm, T = 1.163 s).

5.5. Summary

Based on the findings reported in this chapter, the following conclusions could be drawn:

- Uncertainty analyses of data collected over 4 – 5 repeated runs demonstrated that the global loads and motions associated with extreme wave events affecting a TLP can be measured experimentally with low variability.
- The overset grid technique implemented in STAR-CCM+ was found to be capable of modelling large amplitude surge motions with adequate numerical stability within the tested time frame for all simulated cases.
- The model's motions and tendon tensions predicted by CFD were found to be in good agreement with the experimental measurements except for the initial transient periods caused by the start-up condition of the wavemaker.
- The aft tendons were found to experience slackness following the deck impact in many wave cycles. CFD results showed that the downward component of the vertical wave-in-deck force was approximately synchronised with the minimum tendon tensions and caused such slack situations.
- The leg pretension measured in model tests were found to be too sensitive to the initial conditions and varied amongst test runs. Another complexity of the model tests lies in the effect that regular waves often fail to reach the steady

state and hence the wave-in-deck slam pressures vary in time and space. On the other hand, regular waves generated by CFD models demonstrated improved stability. Using the exactly measured wave height and the tendon pretension would improve CFD results.

- Although CFD simulations showed that there was a strong water-air interaction at the moment of impact, the variation of air compressibility values did not generate a significant difference in the magnitude of the computed impact pressures. CFD predictions of maximum pressure were found to favourably agree to the measured one provided that the pressure measurement is obtained over repeated runs.
- Challenges remain in the measurement and computation of wave slamming pressures. Variability of the pressure measurements was found to be high; it is recommended to run at least five runs per each test to obtain a reliable pressure value.

Chapter 6: Conclusions and Further Work

This chapter presents the main conclusions of this research and a number of recommendations for further work.

6.1. Conclusions

On the basis of the reported findings in this thesis, the following main conclusions can be drawn:

1. The data analyses of experimental measurements reported in Chapters 2 – 5 showed that extreme wave events and associated global wave impact loads and response could be generated with good repeatability (low variability) within a coefficient of variation of 5%. However, the impact pressure was found to be extremely variable in magnitude and duration of up to 70% coefficient of variation.

Fixed Deck

2. A reduction of deck clearance (up to 2.5 m in full scale, ≈17% of the original deck clearance) of the fixed platform deck structure subjected to long-crested irregular waves significantly increased global wave-in-deck loads (approximately by a factor of 2.0). However, reducing deck clearance did not increase slam pressure for all locations.
3. The front half of the deck underside experienced larger impact pressures than the rear section in most test conditions, yet, at lower deck clearances the rear section experienced larger slam pressures.

Fixed Multicolumn Platform

4. The horizontal force acting on the fixed multicolumn platform subjected to irregular wave impact was found to be clearly affected by a small reduction in the deck clearance of 10 mm and 20 mm (1.25 m and 2.5 m full scale, ≈ 8 %–17% of the original deck clearance) such that the force magnitudes were amplified by 7% to 22%. However, the reduction of deck clearance had no a clear effect on either global or local vertical wave-in-deck loads.

5. The experimental results showed that the deck-column intersection areas experienced large wave-in-deck slamming pressures, in particular around the aft columns.

Compliant TLP

6. The experimental results of the compliant TLP subjected to long-crested irregular waves demonstrated a positive effect of compliance of a floating structure; in all wave-in-deck events, the wave came in contact with the deck when the platform was moving in the direction of the wave.
7. The wave-in-deck impact events had a significant effect on the tendons such that slack in the down-wave tendons and ringing responses were observed. Overall, the maximum impact pressures around the forward and aft columns correlated qualitatively with the maximum tension in the up-wave and down-wave tendons. The slam pressure was also found to correlate with wave steepness; steeper waves tended to cause higher slam pressure.
8. Out of all wave events tests, the events that produced the maximum and minimum tendon tension generally did not correspond to the largest wave crest or the largest wave steepness. This indicated that selection of the design waves, which cause extreme tendon tensions, in the same sea state, may require special investigation.

Numerical Prediction of the Wave-in-Deck Events for the compliant TLP

9. Based on the experimental results and the CFD simulations for regular wave tests on the compliant TLP, the model's motions and tendon tensions predicted by CFD were found to be in good agreement with the measurements except for the initial transient periods caused by the start-up condition of the wavemaker.
10. CFD results showed the overset grid technique implemented in STAR-CCM+ was capable of modelling large amplitude surge motions with an adequate numerical stability within the tested time frame for all simulated cases.
11. The maximum downward force acting on the deck during the wave-in-deck event was approximately synchronised with the minimum tendon tensions.

This confirmed that slack situations in the down-wave tendons were caused by the hydrodynamic "suction" force below the deck.

12. Although CFD simulations at model scale showed that there was a strong water-air interaction at the moment of wave impact, the variation of air compressibility values through modelling the air density as a function of pressure did not generate a significant difference in the magnitude of most computed impact pressures. In some cases, however, the magnitude of impact pressure increased by 10% – 24% by modelling compressible air.
13. CFD predictions of maximum pressure were found to favourably agree with the measurements provided that the measured pressure is obtained by averaging results over repeated test runs.
14. When compared with CFD simulations, the tendon pretension measured in model tests were rather sensitive to the initial conditions and varied amongst test runs. The tendon pretensions in the CFD simulations, on the other hand, were always the same.
15. An important complexity of the CFD and the model tests comparisons lies in the fact that regular waves often failed to reach the perfect steady state in the model tests and hence, the wave-in-deck slam pressures varied in time and space. On the other hand, regular waves generated in CFD simulations demonstrated higher stability. Using the exactly measured wave elevations and the tendon pretensions would provide a better basis for the comparison with the CFD results.

6.2. Further Work

The following areas are recommended for further research:

1. It is recommended to investigate the large variability of the impact pressure measurements, which may involve interaction between water and the entrapped air. Measuring the pressure as a force over a certain area rather than a pressure at a discrete point will be more useful in assessing the effect of the deck clearance reduction on the local wave-in-deck loading. Using more sophisticated instruments such as pressure mapping systems for pressure measurements may provide more detailed information about pressure distribution over a deck area.

2. It is recommended to conduct model tests for other extreme wave events, which may occur in the same sea state as tested, and with other platform deck clearances. This would contribute to better understanding of the uncertainties and the hydrodynamic mechanism governing the interaction of abnormal waves with floating structures.
3. Additional work is required to develop the characterisation of the wave impact pressure on the deck of a moving floating structure, in order to better understand its dependency on the main parameters of the structure, its dynamic response and kinematics of the wave.
4. The experimental results of the wave-in-deck events associated with long-crested irregular waves presented in Chapters 2 – 4 can be used to validate CFD simulations using focused wave techniques. In order to conduct CFD modelling, the time series of the different wave elevations measured can be provided on request.
5. The present numerical study using regular wave conditions validated against model tests may serve as a benchmark validation case for further numerical studies and be extended to predict wave-in-deck impact loading due to more complex metocean conditions such as combined waves with current and wind.

References

[1] Kaiser MJ, Yu Y, Jablonowski CJ. Modeling lost production from destroyed platforms in the 2004–2005 Gulf of Mexico hurricane seasons. Energy. 2009;34:1156-71.

[2] Buchan S, Black P, Cohen R. The Impact of Tropical Cyclone Olivia on Australia's Northwest Shelf. Offshore Technology Conference. Houston, USA: Offshore Technology Conference; 1999.

[3] BOM. Report on Cyclone Orson - April 1989, Bureau of Meteorology. Australia1992.

[4] McBride JL. The Estimated Cost of Tropical Cyclone Impacts in Western Australia: A Technical Report for The Indian Ocean Climate Initiative (IOCI) Stage 3. Project 22: Tropical Cyclones in the North West. Australia2012.

[5] Reuters. North Sea storm forces oil platform evacuations, output shutdown [online: http://www.reuters.com/article/us-weather-northsea-idUSKBN0UE0OR20151231] (last accessed 19/June/16). 2016.

[6] Naess A, Gaidai O. Extreme value statistics of non-Gaussian random wave fields and the airgap problem for offshore platforms. The 8th International Conference on Structural Dynamics, EURODYN 2011. Leuven, Belgium2011.

[7] DNV. Recommended practice DNV-RP-C205: environmental conditions and environmental loads. Høvik, Norway: Det Norske Veritas, DNV; 2010.

[8] API. Recommended Practice for Planning, Designing and Constructing Fixed Offshore Platforms–Working Stress Design, 2A-WSD, 2007. American Petroleum Institute; 2007.

[9] Raaij Kv. Dynamic behaviour of jackets exposed to wave-in-deck forces, PhD Thesis in Mech. and Struct. Eng. and Material Scien. . Stavanger, Norway: University of Stavanger; 2005.

[10] Raaij Kv, Gudmestad OT. Wave-in-deck loading on fixed steel jacket decks. Marine Structures. 2007;20:164-84.

[11] ABS. Rules for Building and Classing: Floating Production Installation. Houston, USA: American Bureau of Shipping, ABS; 2014.

[12] API. Planning, Designing, and Constructing Tension Leg Platforms: API recommended practice 2T third edition. USA: American Petroleum Institute, API; 2010.

[13] Scharnke J, Hennig J. Vertical wave impact loading on a fixed platform deck. Proceedings of the ASME 34th International Conference on Ocean, Offshore and Arctic

Engineering, OMAE. St. John's, Newfoundland, Canada: American Society of Mechanical Engineers; 2015.
[14] Bitner-Gregersen EM, Gramstad O. Rogue Waves - Impact on ships and offshore structures. DNV-GL; 2015.
[15] Mansour A, Gordon BJ, Ling Q, Shen Q. TLP Survivability against Progressive Failure of Tendon and Foundation Systems in Offshore Western Australian Harsh Environment. Proceedings of the ASME 32nd International Conference on Ocean, Offshore and Arctic Engineering, OMAE. Nantes, France: ASME; 2013.
[16] BV. Rules for the Classification of Tension Leg Platforms (TLP): Rule Note NR 578 DT R00 E. France: Bureau Veritas, BV; 2012.
[17] Bachynski EE, Moan T. Design considerations for tension leg platform wind turbines. Marine Structures. 2012;29:89-114.
[18] Thiagarajan KP, Repalle N. Wave run-up on columns of deepwater platforms. Proceedings of the Institution of Mechanical Engineers, Part M: Journal of Engineering for the Maritime Environment. 2013;227:256-65.
[19] Hennig J, Scharnke J, Buchner B, van den Berg J. Extreme Load-Response Mechanisms of a Tension Leg Platform due to Larger Wave Crests: Some Results of the 'CresT'JIP. Proceedings of the ASME 30th International Conference on Ocean, Offshore and Arctic Engineering, OMAE: American Society of Mechanical Engineers; 2011. p. 855-64.
[20] Johannessen T, Haver S, Bunnik T, Buchner B. Extreme Wave Effects on Deep Water TLPs Lessons Learned from the Snorre A Model Tests. Proc Deep Offshore Technology 2006. 2006:28-30.
[21] Hirdaris SE, Bai W, Dessi D, Ergin A, Gu X, Hermundstad OA, et al. Loads for use in the design of ships and offshore structures. Ocean engineering. 2014;78:131-74.
[22] Abdussamie N, Amin W, Ojeda R, Thomas G, Drobyshevski Y. Vertical Wave-in-Deck Loading and Pressure Distribution on Fixed Horizontal Decks of Offshore Platforms. Proceedings of the 24th International Offshore and Polar Engineering. Busan, South Korea: International Society of Offshore and Polar Engineers; 2014.
[23] Abdussamie N, Thomas G, Amin W, Ojeda R. Wave-in-Deck Forces on Fixed Horizontal Decks of Offshore Platforms. Proceedings of the ASME 33rd International Conference on Ocean, Offshore and Arctic Engineering, OMAE. San Francisco, CA, USA: American Society of Mechanical Engineers; 2014.

[24] Baarholm R. A simple numerical method for evaluation of water impact loads on decks of large-volume offshore platforms. Proceedings of the ASME 24th International Conference on Ocean, Offshore and Arctic Engineering, OMAE. Halkidiki, Greece: ASME; 2005.
[25] Baarholm R. Experimental and Theoretical Study of Three-Dimensional Effects on Vertical Wave-in-Deck Forces. Proceedings of the ASME 28th International Conference on Ocean, Offshore and Arctic Engineering, OMAE. Honolulu, Hawaii, USA: American Society of Mechanical Engineers; 2009.
[26] Baarholm R, Faltinsen OM. Wave impact underneath horizontal decks. Journal of Marine Science and Technology. 2004;9:1-13.
[27] Bhat SS. Wave slamming on a horizontal plate, MSc Thesis in Civil Engineering: University of British Columbia; 1994.
[28] Birknes-Berg J, Johannessen T. Methods for establishing governing deck impact loads in irregular waves. The ASME 2015 34th International Conference on Ocean, Offshore and Arctic Engineering, OMAE. St. John's, Newfoundland, Canada: ASME; 2015.
[29] Ding Z, Ren B, Wang Y, Ren X. Experimental study of unidirectional irregular wave slamming on the three-dimensional structure in the splash zone. Ocean Engineering. 2008;35:1637-46.
[30] El Ghamry O. Wave forces on platform decks. Proceedings of Offshore Technology Conference. Dallas, USA: Offshore Technology Conference; 1971. p. 537-48.
[31] Kendon TE, Pakozdi C, Baarholm RJ, Berthelsen PA, Stansberg CT, Enger S. Wave-in-deck impact: Comparing cfd, simple methods, and model tests. Proceedings of the ASME 29th International Conference on Ocean, Offshore and Arctic Engineering, OMAE: American Society of Mechanical Engineers; 2010. p. 495-509.
[32] Vestbøstad TM. A Numerical Study of Wave-in-Deck Impact using a Two-dimensional Constrained Interpolation Profile Method, PhD Thesis in Marine Technology. Norway: Norwegian University of Science and Technology; 2009.
[33] ISO. Petroleum and natural gas industries-fixed steel offshore structures, International Organization for Standardization. . In: Organization IS, editor. ISO 199022007.
[34] Kaplan P. Wave impact forces on offshore structures: re-examination and new interpretations. *Offshore Technology Conference, OTC 6814*. Houston, TX1992.
[35] Kaplan P, Murray J, Yu W. Theoretical analysis of wave impact forces on platform deck structures. Offshore Technology Conference Houston, USA1995.
[36] Scharnke J, Vestbostad T, Wilde Jd, Haver SK. Wave-In-Deck Impact Load Measurements on a Fixed Platform Deck. Proceedings of the ASME 33rd International

Conference on Ocean, Offshore and Arctic Engineering, OMAE. San Francisco, CA, USA: American Society of Mechanical Engineers; 2014.
[37] CD-Adapco. User guide - Star-CCM+ Version 7.04. CD-Adapco; 2012.
[38] Fluent A. Ansys Fluent 12.0 user guide. ANSYS Inc. 2009.
[39] Abdussamie N, Ojeda R, Amin W, Thomas G, Drobyshevski Y. Prediction of Wave-in-Deck Loads on Offshore Structures Using CFD. the 19th Australasian Fluid Mechanics Conference. Melbourne, Australia: AFMS; 2014.
[40] Iwanowski B, Vestbostad T, Lefranc M. Wave-In-Deck Load on a Jacket Platform, CFD Calculations Compared with Experiments. Proceedings of the ASME 33rd International Conference on Ocean, Offshore and Arctic Engineering, OMAE. San Francisco, CA, USA: ASME; 2014.
[41] Pákozdi C, Östeman A, Stansberg CT, Peric M, Lu H, Baarholm R. Estimation of Wave in Deck Load Using CFD Validated Against Model Test Data. Proceedings of the 25th International Offshore and Polar Engineering Conference: International Society of Offshore and Polar Engineers; 2015.
[42] Schellin TE, Perić M, el Moctar O. Wave-in-Deck Load Analysis for a Jack-Up Platform. Journal of Offshore Mechanics and Arctic Engineering. 2011;133:021303.
[43] Iwanowski B, Lefranc M, Wemmenhove R. CFD simulation of wave run-up on a semi-submersible and comparison with experiment. Proceedings of the ASME 28th International Conference on Ocean, Offshore and Arctic Engineering, OMAE: ASME; 2009.
[44] Lee S-K, Yu K, Huang SC. CFD Study of Air-Gap and Wave Impact Load On Semisubmersible Under Hurricane Conditions. Proceedings of the ASME 33th International Conference on Ocean, Offshore and Arctic Engineering, OMAE. San Francisco, CA, USA: ASME; 2014.
[45] Buchner B, Bunnik T. Extreme wave effects on deepwater floating structures. Offshore Technology Conference. Houston, Texas2007.
[46] Rudman M, Cleary PW. Rogue wave impact on a tension leg platform: The effect of wave incidence angle and mooring line tension. Ocean Engineering. 2013;61:123-38.
[47] Rudman M, Cleary PW. The influence of mooring system in rogue wave impact on an offshore platform. Ocean engineering. 2016;115:168-81.
[48] Wu G, Jang H, Kim JW, Ma W, Wu M-C, O'Sullivan J. Benchmark of CFD Modeling of TLP Free Motion in Extreme Wave Event. ASME 2014 33rd International Conference on Ocean, Offshore and Arctic Engineering: American Society of Mechanical Engineers; 2014. p. V002T08A86-VT08A86.

[49] Chen H-C, Lee S-K, Seah AK. Overset grid CFD applications for challenging offshore hydrodynamic problems. ABS Technical Paper. 2008.
[50] Almeland I, Gaul T, Pettersen D, Vogel H. Snorre TLP configuration and analysis technology. Proceedings of Offshore Technology Conference. Houston, USA: Offshore Technology Conference; 1991.
[51] Abdussamie N, Amin W, Ojeda R, Thomas G, Drobyshevski Y. Irregular Wave Generation and Assessment of Static Air Gap of Offshore Structures. Proceedings of the 19th Australasian Fluid Mechanics Conference. Melbourne, Australia: AFMS; 2014.
[52] Broughton P, Horn E. Ekofisk platform 2/4C: re-analysis due to subsidence. Institution of Civil Engineers Proceedings pt1. 1987;82:949-79.
[53] Olagnon M, Nerzic R, Prevosto M. Extreme water level from joint distributions of tide, surge and crests: a case study. Proceedings of the International Offshore and Polar Engineering1999. p. 95-100.
[54] Sekhar GR, Nallayarasu S. Experimental investigation of the wave slam and slap coefficients for array of non-circular section of offshore platforms. Ships and Offshore Structures. 2013;8:15-28.
[55] Chakrabarti S. Handbook of Offshore Engineering. Elsevier Publications, Oxford, UK; 2005.
[56] van Dijk R, van den Boom H. Full scale monitoring marco polo tension leg platform. Proceedings of the ASME 26th International Conference on Ocean, Offshore and Arctic Engineering, OMAE: American Society of Mechanical Engineers; 2007. p. 915-21.
[57] Oberlies R, Khalifa J, Huang J, Hetland S, Younan A, Overstake M, et al. Determination of Wave Impact Loads for the Hebron Gravity Based Structure (GBS). Proceedings of the ASME 33rd International Conference on Ocean, Offshore and Arctic Engineering, OMAE: American Society of Mechanical Engineers; 2014.
[58] Winsor F. Evaluation of methods to remove inertial force from measured model wave impact force signals. Ocean engineering. 2002;30:47-84.
[59] Murray J, Winso F, Kaplan P. Impact forces on a jacket deck in regular waves and irregular wave groups. Offshore Technology Conference: Offshore Technology Conference; 1997.
[60] Cooker M. The interaction between steep water waves and coastal structures, PhD Thesis in Mathematics: University of Bristol; 1990.

[61] Abdussamie N, Ojeda R, Drobyshevski Y, Thomas G, Amin W. Experimental investigation of extreme wave impacts on a rigid TLP model in cyclonic conditions. Ships and Offshore Structures. 2016:1-18.
[62] Abdussamie N, Ojeda R, Thomas G, Amin W. Measurements of global and local effects of wave impact on a fixed platform deck - "accepted in press". the Proceedings of the Institution of Mechanical Engineers, Part M: Journal of Engineers for the Maritime Environment. 2016.
[63] Wang H. Water wave pressure on horizontal plate. Journal of the Hydraulics Division. 1970;96:1997-2017.
[64] Souterm K, Krachman HE. Measurement of local pressures resulting form hydrodynamic impact ENDEVCO.Technical Paper TP 269.
[65] Choi J, Yoon SB. Numerical simulations using momentum source wave-maker applied to RANS equation model. Coastal Engineering. 2009;56:1043-60.
[66] Demirbilek Z. Design formulae for offset, set down and tether loads of a tension leg platform (TLP). Ocean engineering. 1990;17:517-23.

Appendix A

Additional Results of Chapter 4

Wave event WE#1

Model scale (1:125): H = 231 mm, η_c = 145 mm, T_z = 1.48 s, λ = 3.39 m, S = 0.068

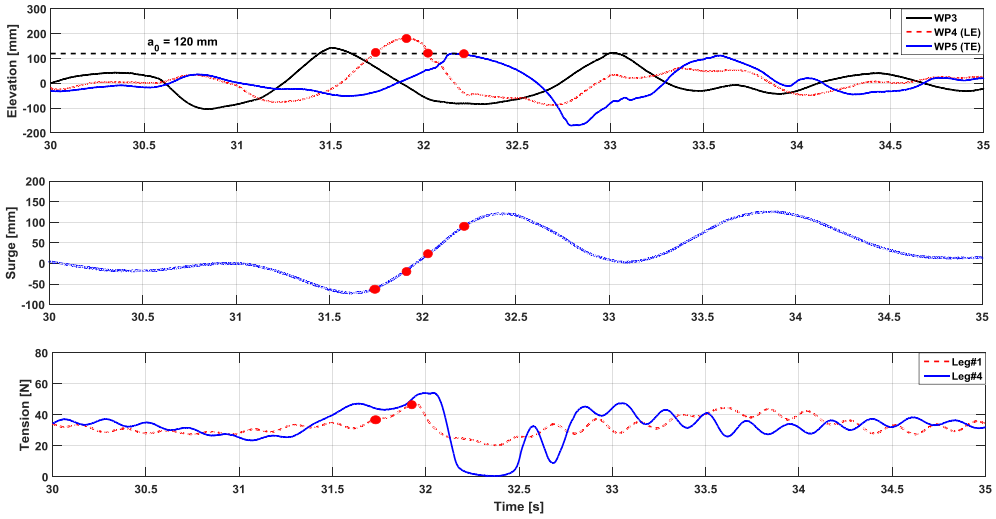

Fig.A 1: Simultaneous measurements: wave elevations (top); surge motion (middle); tendon tension (bottom).

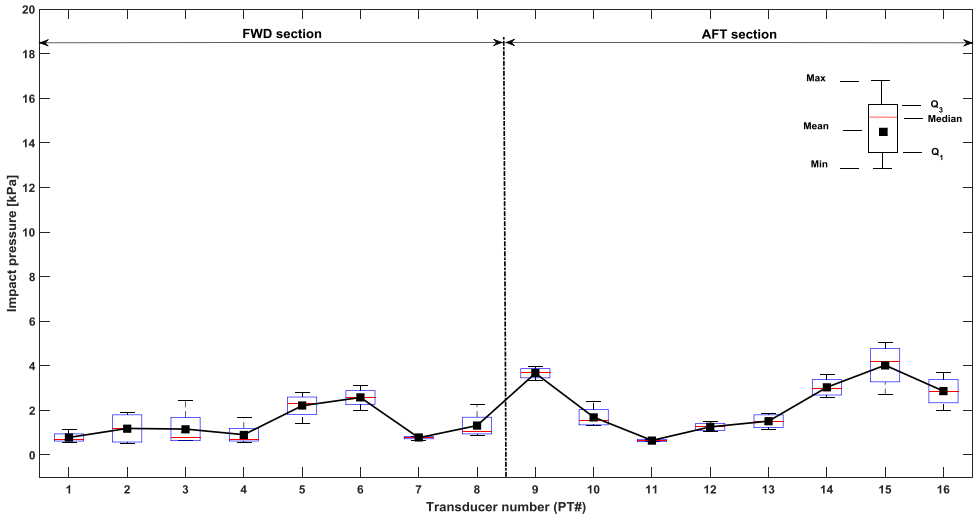

Fig.A 2: Boxplots showing variation in impact pressure at different pressure transducers.

Wave event WE#2

Model scale (1:125): H = 260 mm, η_c = 163 mm, T_z = 1.37 s, λ = 2.92 m, *S* = 0.089

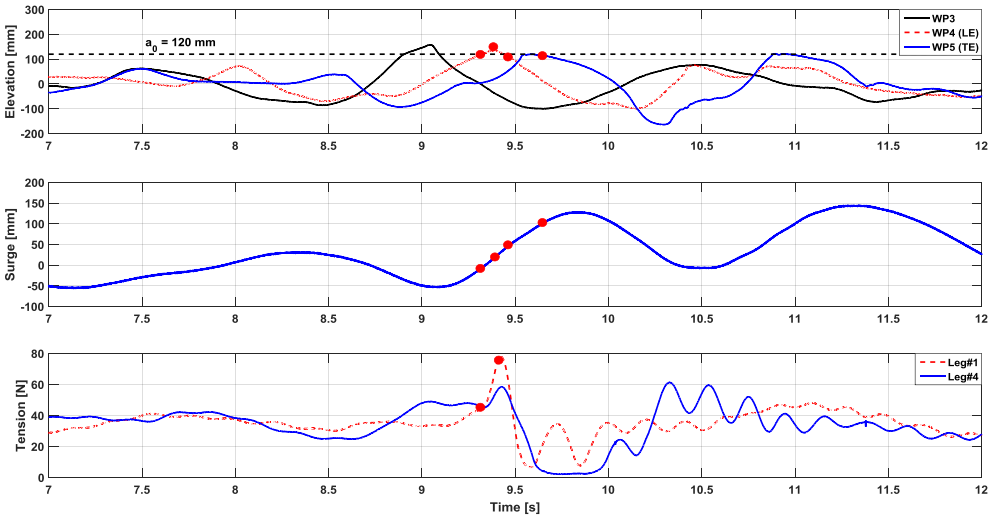

Fig.A 3: Simultaneous measurements: wave elevations (top); surge motion (middle); tendon tension (bottom).

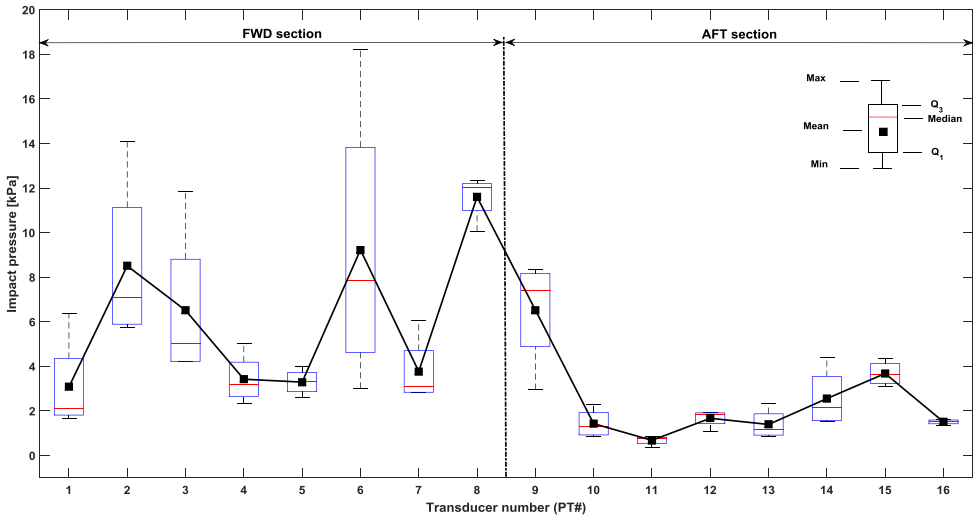

Fig.A 4: Boxplots showing variation in impact pressure at different pressure transducers.

Wave event WE#3

Model scale (1:125): H = 238 mm, η_c = 171 mm, T_z = 1.65 s, λ = 4.16 m, *S* = 0.057

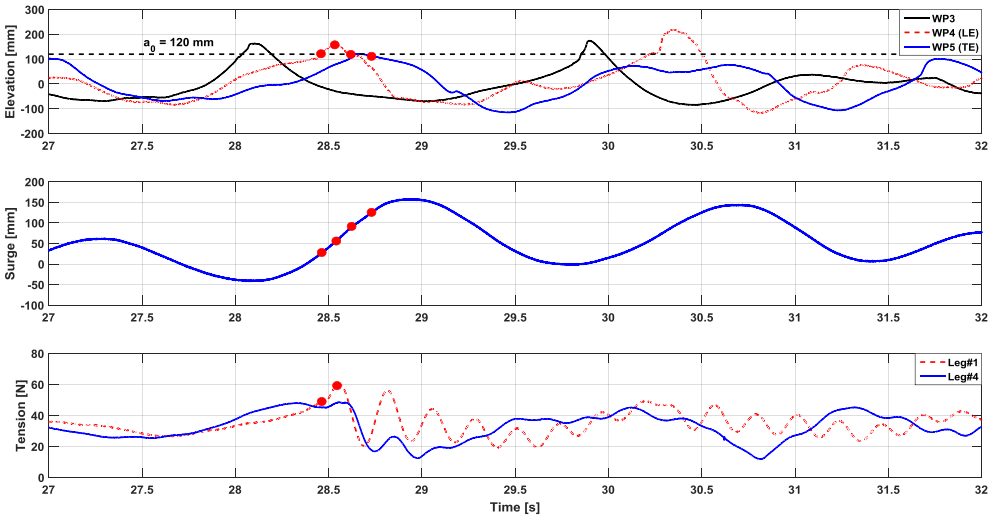

Fig.A 5: Simultaneous measurements: wave elevations (top); surge motion (middle); tendon tension (bottom).

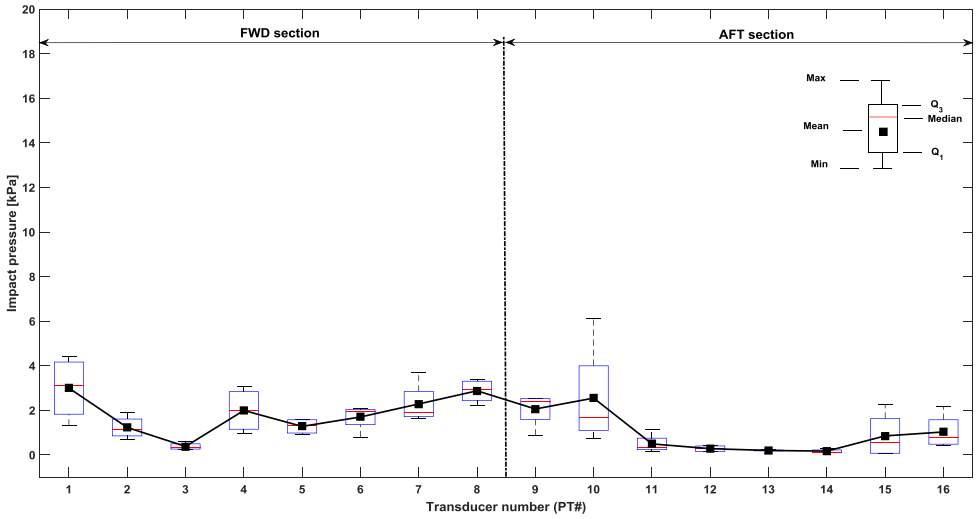

Fig.A 6: Boxplots showing variation in impact pressure at different pressure transducers.

Wave event WE#4

Model scale (1:125): H = 227 mm, η_c = 137 mm, T_z = 1.35 s, λ = 2.84 m, *S* = 0.08

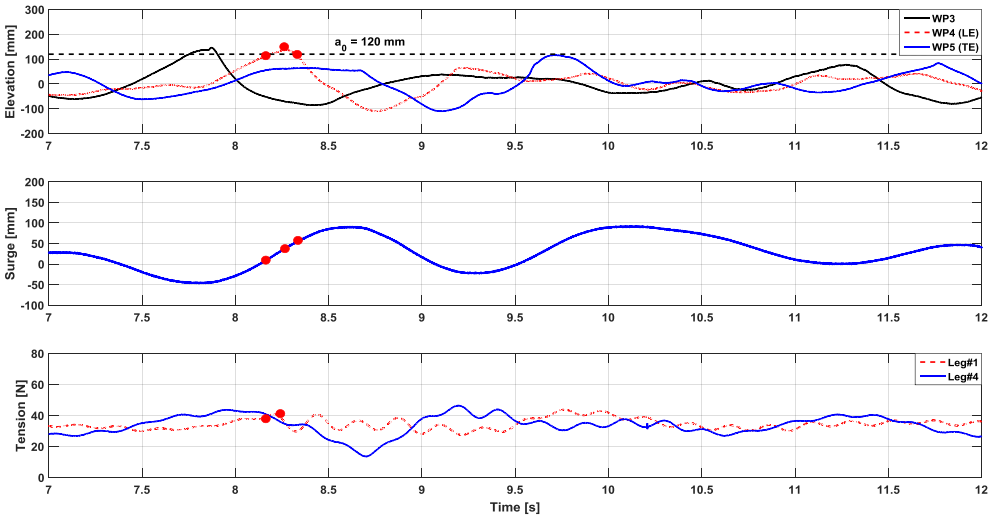

Fig.A 7: Simultaneous measurements: wave elevations (top); surge motion (middle); tendon tension (bottom).

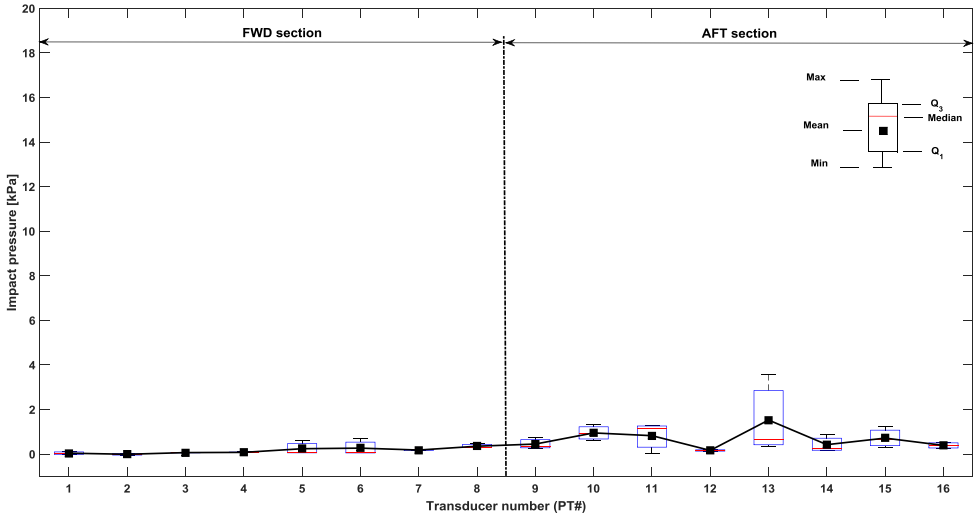

Fig.A 8: Boxplots showing variation in impact pressure at different pressure transducers.

Wave event WE#5

Model scale (1:125): H = 186 mm, η_c = 156 mm, T_z = 1.76 s, λ = 4.67 m, *S* = 0.04

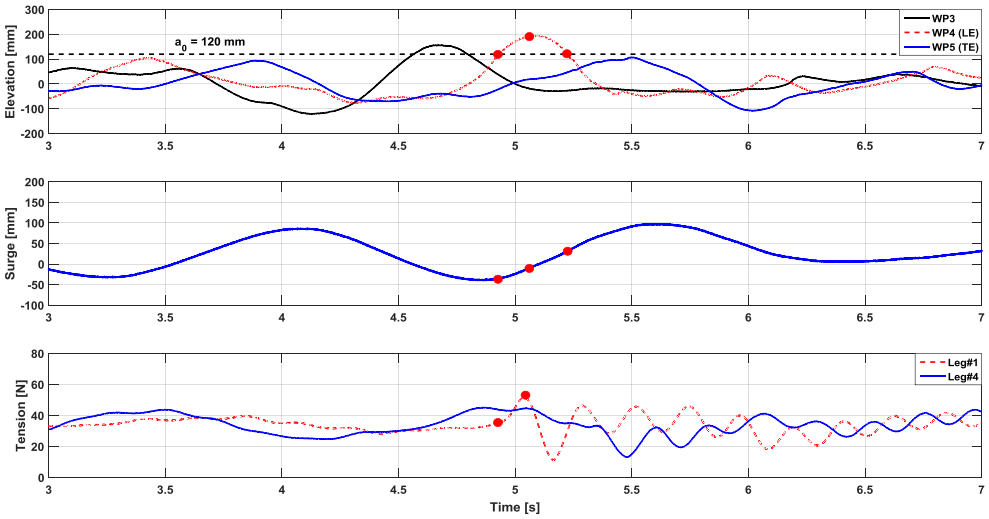

Fig.A 9: Simultaneous measurements: wave elevations (top); surge motion (middle); tendon tension (bottom).

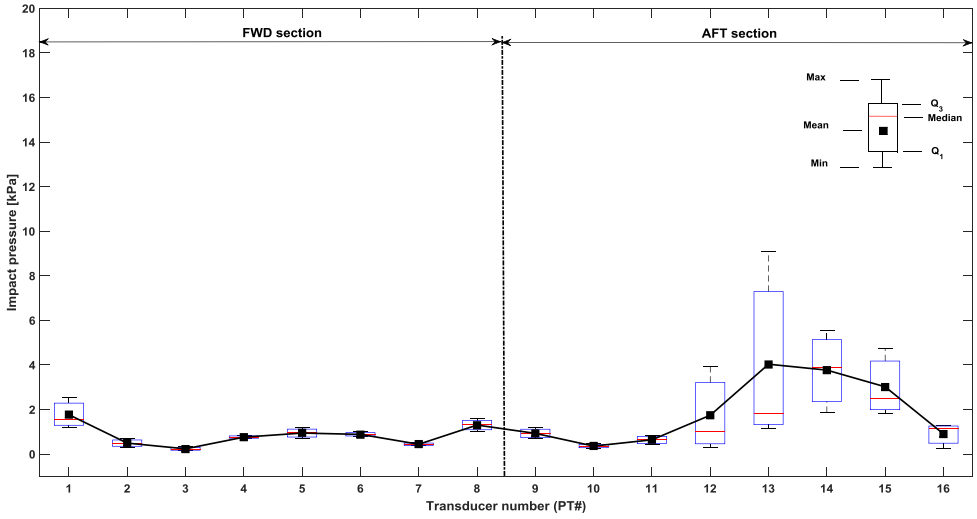

Fig.A 10: Boxplots showing variation in impact pressure at different pressure transducers.

Wave event WE#6

Model scale (1:125): H = 168 mm, η_c = 126 mm, T_z = 1.73 s, λ = 4.53 m, *S* = 0.037

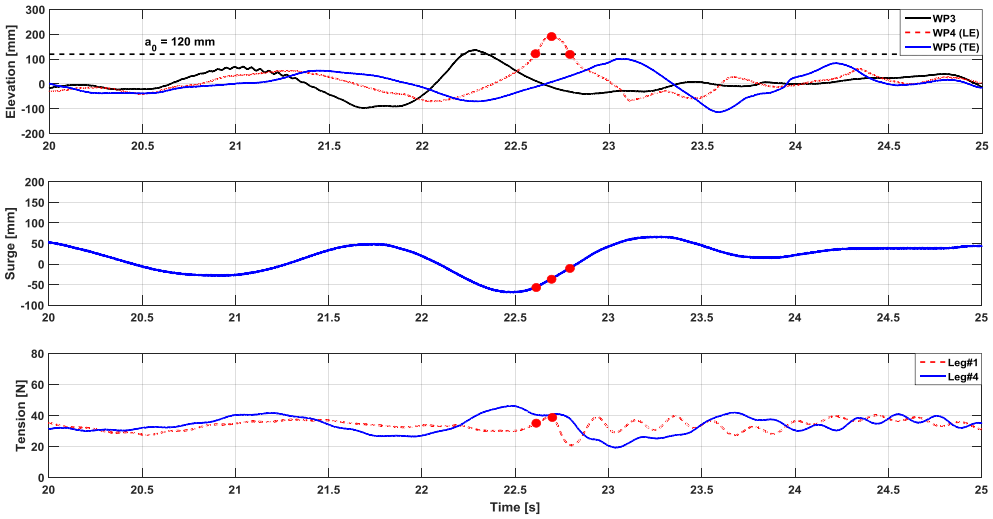

Fig.A 11: Simultaneous measurements: wave elevations (top); surge motion (middle); tendon tension (bottom).

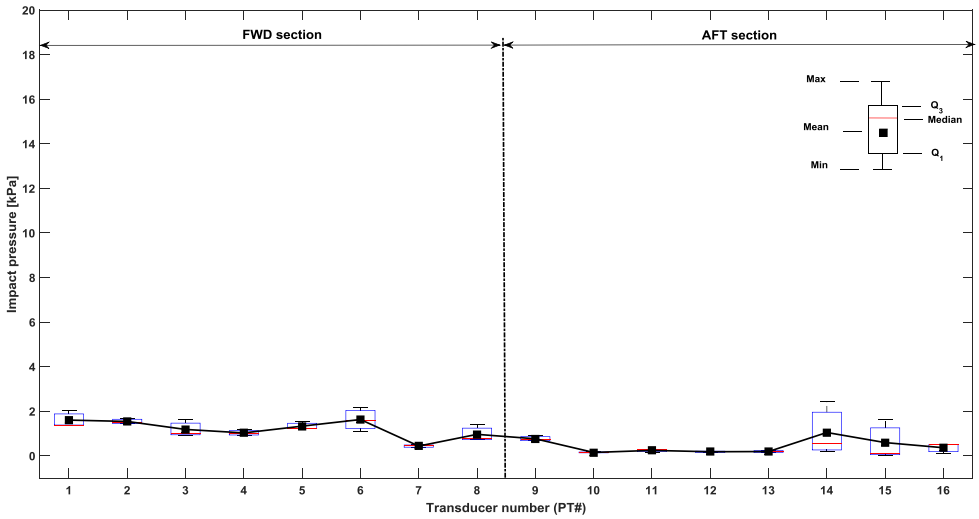

Fig.A 12: Boxplots showing variation in impact pressure at different pressure transducers.

Wave event WE#7

Model scale (1:125): H = 191 mm, η_c = 144 mm, T_z = 1.44 s, λ = 3.22 m, *S* = 0.059

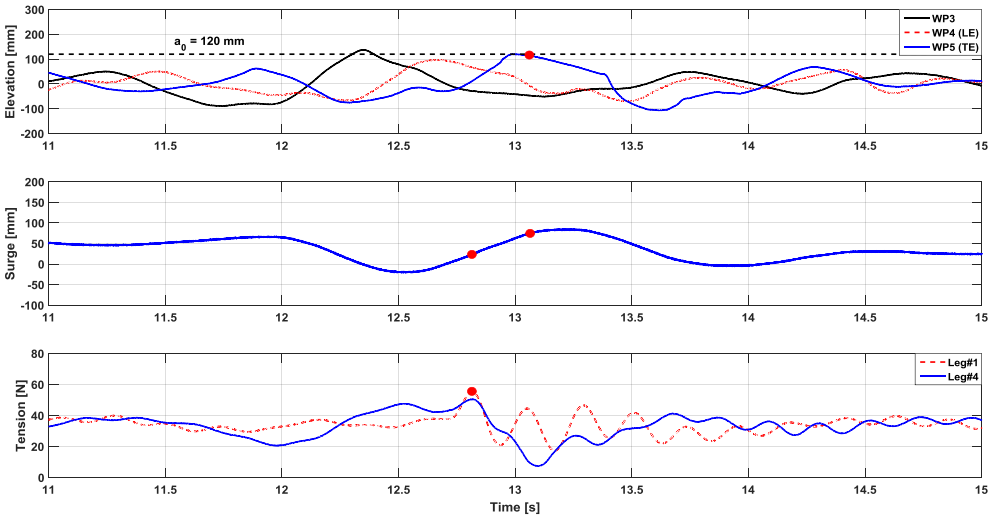

Fig.A 13: Simultaneous measurements: wave elevations (top); surge motion (middle); tendon tension (bottom).

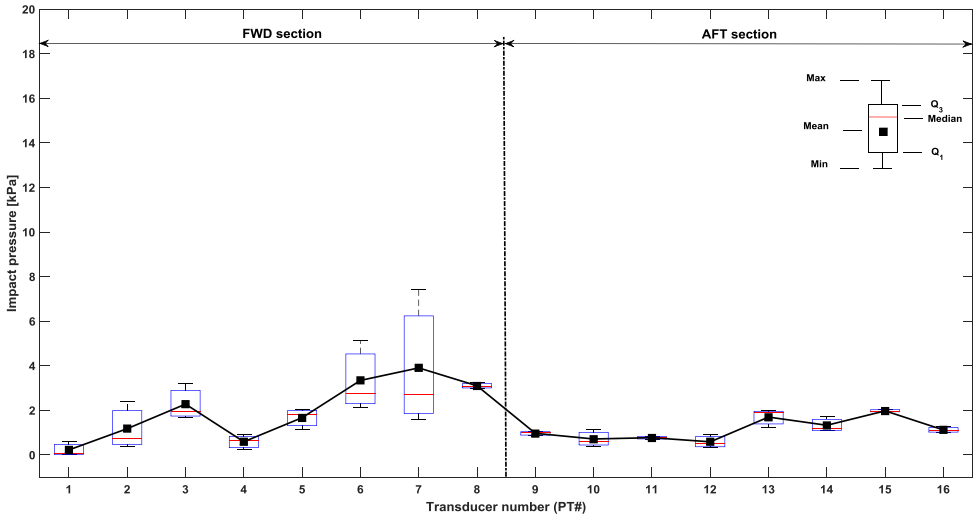

Fig.A 14: Boxplots showing variation in impact pressure at different pressure transducers.

Wave event WE#8

Model scale (1:125): H = 261 mm, η_c = 160 mm, T_z = 1.46 s, λ = 3.31 m, *S* = 0.079

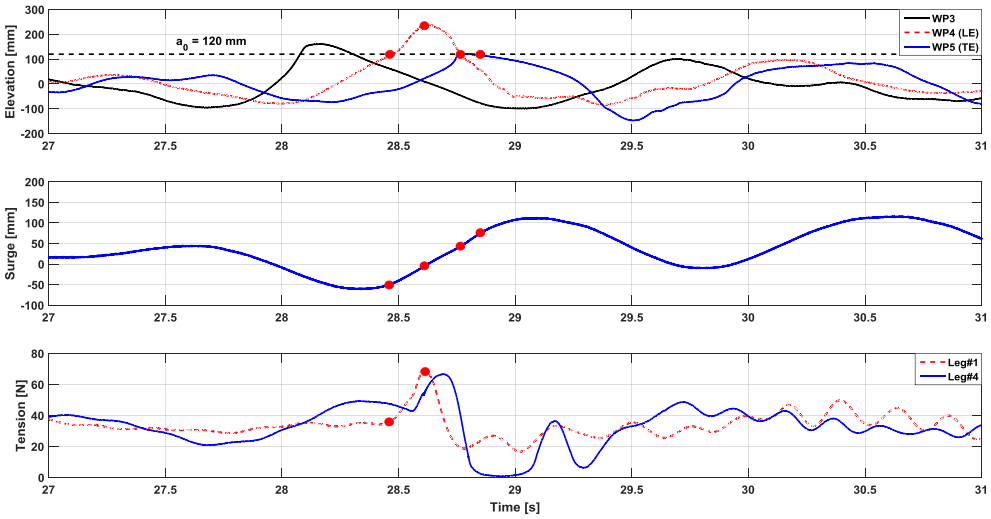

Fig.A 15: Simultaneous measurements: wave elevations (top); surge motion (middle); tendon tension (bottom).

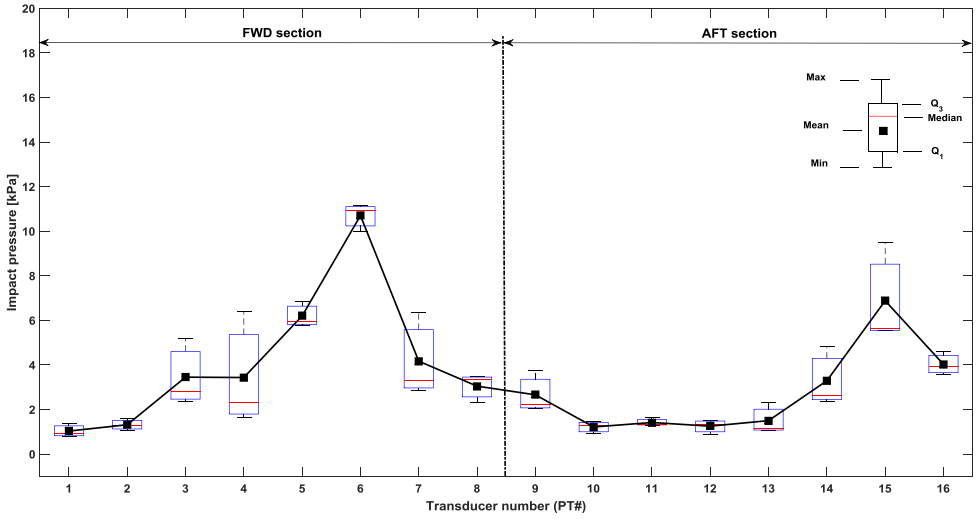

Fig.A 16: Boxplots showing variation in impact pressure at different pressure transducers.

Appendix B

Vertical Wave-in-Deck Loading and Pressure Distribution on Fixed Horizontal Decks of Offshore Platforms

This conference paper was presented at the 24th International Offshore and Polar Engineering (ISOPE) Conference in Busan, South Korea. The citation for this paper is:

Abdussamie N, Amin W, Ojeda R, Thomas G, Drobyshevski Y. 2014. Vertical Wave-in-Deck Loading and Pressure Distribution on Fixed Horizontal Decks of Offshore Platforms. Proceedings of the 24th International Offshore and Polar Engineering (ISOPE-I-14-058); 2014 Jun 15-20; Busan, South Korea: ISOPE.

Appendix C

Prediction of Wave-in-Deck Loads on Offshore Structures Using CFD

This conference paper was presented at the 19th Australasian Fluid Mechanics Conference (AFMC) in Melbourne, Australia. The citation for this paper is:

Abdussamie N, Ojeda R, Amin W, Thomas G, Drobyshevski Y. 2014. Prediction of Wave-in-Deck Loads on Offshore Structures. Proceedings of the 19th Australasian Fluid Mechanics Conference (AFMC) in Melbourne, Australia: AFMS.

Appendix D

Offshore Platforms in Waves – CFD Simulations for Devastating Conditions

This conference paper is to be presented at the 12th International Offshore and Polar Engineering (ISOPE) Pacific/Asia Offshore Mechanics Symposium (PACOMS-2016) in Gold Coast, Brisbane, Australia.